Modulating Neuroinflammation with Porous Templated Scaffolds

Ian D. Dryg

A dissertation

Submitted in partial fulfillment of the

Requirements for the degree of

Doctor of Philosophy

University of Washington

2019

Supervisory Committee:

Buddy Ratner, Chair

James Bryers

Steve Perlmutter

Eric Chudler

University of Washington

Abstract

Modulating Neuroinflammation with Porous Templated Scaffolds

Ian D. Dryg

Chair of the Supervisory Committee:

Buddy Ratner

Department of Bioengineering

Neuroelectronic interfaces can restore mobility and independence for patients with neurological conditions such as spinal cord injury, stroke, or limb loss. However, unstable neural recording performance remains unresolved. Via the foreign body reaction, macrophages and glial cells develop a “glial scar” around implants, increasing electrode impedance and leading to time-dependent declines in electrode performance. During the first two years of my PhD, I worked with Dr. Bill Shain to study the brain’s foreign body reaction to a variety of cortical implants, using Electrochemical Impedance Spectroscopy, Optical Coherence Tomography, and post-hoc Immunohistochemistry. After Dr. Shain retired, I joined the labs of Dr. Buddy Ratner and Dr. James Bryers to study the effects of porous hydrogels on the foreign body reaction in the central nervous system, and how they might improve regeneration after spinal cord injury and glial scarring around implanted cortical recording devices. We observed reduced astrocyte encapsulation and increased neuron density around softer, porous hydrogels compared to stiffer, nonporous hydrogels.

Contents

List of Figures 4

List of Tables 7

Chapter 1: Introduction 11

1.1 Motivation 11

1.2 Background 11

Chapter 2: CNS Tissue Response to Implanted Neural Recording Devices 13

2.1 Introduction 13

2.2 – Project 1 – poly(trivinyltrimethylcyclotrisiloxane): GVD's Exilis™ Coating to Reduce Brain Tissue Responses and Improve Utah Array Functionality in rat cortex 13

2.2 – Project 2 – Glassy Carbon Micro-ECoG Arrays 17

2.3 – Project 3 – Actively controlled release of Dexamethasone from neural microelectrodes in a chronic in vivo study 21

Chapter 3: Optical Coherence Tomography for In-Vivo Monitoring of Neural Implants 24

3.1 Introduction 24

3.2 Materials and Methods 24

3.3 Results and Conclusions 26

Chapter 4: Background on The Foreign Body Reaction & Porous Biomaterials 30

4.1 Change of labs: 30

4.2 Background on The Foreign Body Response & Biomaterials 30

4.3 Background on Porous Biomaterials in the Ratner & Bryers Labs 31

Chapter 5: Development of Porous Neural Implants 37

5.1 Methods of creating Porous Templated Scaffolds for Neural Interface Experiments 37

5.2 Initial Attempts at Incorporating Microwires for Neural Recordings 40

Chapter 6: Characterization of Inflammation after Spinal Cord Injury 43

6.1 Introduction 43

6.2 Materials and Methods 44

6.1.1 – Porous Templated Scaffolds for Spinal Cord Regeneration 44

6.1.2 – Using Flow Cytometry to Assess Effects of Duratomy on Neuroinflammation After SCI 47

Chapter 7: CNS Tissue Response to Porous Materials 53

7.1 Introduction 53

7.2 Materials and Methods 53

Chapter 8: Effect of Implant Stiffness on CNS Tissue Response to Porous Materials 64

8.1 Introduction 64

8.2 Methods 66

8.2.1 Polymer Fabrication Methods 66

8.2.2 Tissue Histology Analysis 72

8.3 Results 75

8.4 Discussion and Conclusions 85

Chapter 9: Conclusions and Future Directions 88

9.1 Conclusions and Future Directions 88

Bibliography 89

Appendix 94

Tissue Histology Protocol 94

Shain Lab Immunohistochemistry Protocol for Floating Sections 95

Shain Lab 4% Paraformaldehyde Recipe 96

Shain Lab HBHS (HEPES Buffered Hanks Saline) Recipe 97

List of publications: 98

List of Figures

Figure 1 *– Schematic representation of the matrix structure of the Exilis™ polymer film.* 14

Figure 2 *- Histology of rat brains after implantation with Utah Arrays.* 15

Figure 3 *- Stained cells on explanted Utah Arrays.* 15

Figure 4 *– Nyquist plots summarizing complex impedance spectroscopy (CIS) results* 16

Figure 5 *– Device schematic (left) and image of surgical implantation of the glassy carbon array* 18

Figure 6 *- Tissue growth through array's breathing holes can be used to verify electrode locations.* 19

Figure 7 *- Increased GFAP signal beneath the array, but tissue responses appear minimal.* 19

Figure 8 *- FARSIGHT analysis of microglial morphology underneath implanted µECoG array* 20

Figure 9 *- Quantified histology of Dex-release implants.* 22

Figure 10 *- Quantified histology for Neurons, based on NeuN fluorescent staining.* 23

Figure 11 *– OCT Project surgical setup.* 26

Figure 12 *- Changes in electrode position can be monitored using the OCT signal profile. Here, the distance between the OCT probe (x-axis = 0) and the Silicon Probe (peak on right of each profile) decreases over time (y-axis). If electrode position changes, neural recording quality may be affected.* 26

Figure 13 *- Comparisons between IHC (Sagittal sections in (a,b)) and OCT signal (c).* 28

Figure 14 *- Effect of CH4 plasma coating on glial encapsulation of the OCT probes.* 29

Figure 15 *- Schematic of the different phases of the FBR over time (Grainger, 2013).* 31

Figure 16 *- Fabrication process for PTS, otherwise known as the "6-S Process".* 34

Figure 17 *- Oblique view of 35-µm pore pHEMA PTS* 34

Figure 18 *- Intra-pore vascular density after 4 weeks of subcutaneous implantation varies with pore size.* 35

Figure 19 *- Foreign body reaction is reduced with porous implants* 35

Figure 20 *- Representative samples of glass + PMMA tube molded (left), needle-punched (center), and glass + PMMA coating molded (right) porous rods.* 39

Figure 21 *- Scanning electron micrograph of an unscraped rod using the PMMA coating method (bottom) and a scraped rod (top). The scraping method yields more consistent results.* 40

Figure 22 *- Defects in the microwire's Teflon insulation after undergoing the PTS fabrication procedure. Left scale bar is 30 µm s, right scale bar is 100 µm.* 41

Figure 23 *- Impedance measurement of microwires before (left, blue) and after (right, green) undergoing the PTS fabrication process.* 42

Figure 24 *- Demonstration of polymer swelling and microwire tip location change depending on processing steps. Wires cut after polymer lyophilization result in the least amount of wire extending from the polymer rod at the end of fabrication. (DCM is dichloromethane).* 42

Figure 26 *- Inflammation gives way to pro-healing processes in normal wound healing, whereas inflammation does not resolve after SCI.* 44

Figure 27 *- Porous SCI Implant Histology.* 46

Figure 28 *- Functional recovery of rats with SCI* 47

Figure 29 *- Intraspinal pressure increases at the injury site and rostral to the injury site after spinal cord injury.* 49

Figure 30 *- Example of gatings used for flow analysis.* 51

Figure 31 *- Flow cytometry results.* 52

Figure 32 *- Experimental design for initial cortical implant experiment* 54

Figure 33 *- Representative 20X confocal images from each group.* 55

Figure 34 *- Normalized GFAP (astrocytes) fluorescence vs. distance from the center of the implant, 7 days post implant.* 57

Figure 35 *- Normalized iba1 (microglia) fluorescence vs. distance from the center of the implant, 7 days post implant.* 58

Figure 36 *- Normalized GFAP (astrocytes) fluorescence vs. distance from the center of the implant, 21 days post implant.* 58

Figure 37 *- Normalized iba1 (microglia) fluorescence vs. distance from the center of the implant, 21 days post implant.* 59

Figure 38 *- Molded 40 µm porous rod within brain tissue, labeled with MAP2 (Neurons, green), RECA1 (vascular endothelium, red), and Hoechst (nuclei, blue).* 60

Figure 39 *- Nonporous pHEMA rod within brain tissue, labeled with MAP2 (Neurons, green), RECA1 (vascular endothelium, red), and Hoechst (nuclei, blue).* 60

Figure 40 *- Punched 40 µm porous rod within brain tissue, labeled with MAP2 (Neurons, green), RECA1 (vascular endothelium, red), and Hoechst (nuclei, blue).* 61

Figure 41 *- Punched 100 µm porous rod within brain tissue, labeled with MAP2 (Neurons, green), RECA1 (vascular endothelium, red), and Hoechst (nuclei, blue).* 62

Figure 42 *- Slices labeled with CD68 (macrophages, activated microglia, red) and Hoechst (cell nuclei, blue).* 62

Figure 43 *- The wide spectrum of stiffnesses in available neural interface materials compared to biological tissue.* 64

Figure 44 *- HEMA and GMA monomers.* 65

Figure 45 *- Stiffness tunability of pHEMA/GMA* 65

Figure 46 *- Scanning electron micrographs of pHEMA/GMA scaffolds* 67

Figure 47 *– Hydrated pHEMA/GMA bulk mechanical properties* 67

Figure 48 *– Lyophilized pHEMA/GMA bulk mechanical properties* 68

Figure 49 *- Scanning Electron Micrographs showing gelatin reinforced porous rods from each implant group.* 70

Figure 50 *- Surgical schematic for the polymer stiffness study.* 71

Figure 51 *- Demonstration of the area under the curve measurements for glial encapsulation.* 73

Figure 52 *- Demonstration of neuronal counting within 50 µm bands.* 74

Figure 53 *- Confocal microscopy images of glial encapsulation for each group.* 75

Figure 54 *- Astrocyte encapsulation 0-25 µm outside implants.* 76

Figure 55 *- Microglia encapsulation 0-25 µm outside implants.* 76

Figure 56 *- Normalized Neuron Density plotted as % of control tissue.* 77

Figure 57 *- Average Integrated Density of NeuroFilament images.* 78

Figure 58 *- Average Integrated Density for MAP2 images.* 78

Figure 59 *- Examples of positive NeuN expression within 40 µm pores. Green is NeuN (neurons), red is GFAP (astrocytes), and blue is Hoechst (cell nuclei). Scale bars are 100 µm.* 79

Figure 60 *- Examples of positive NeuroFilament expression within pores. Green is NeuroFilament (axons), red is GFAP (astrocytes), and blue is Hoechst (cell nuclei). Scale bars are 100 µm.* 80

Figure 61 *- Examples of MAP2 expression within pores. Green is MAP2 (dendrites), red is RECA1 (endothelium), and blue is Hoechst (cell nuclei). Scale bars are 100 µm.* 81

Figure 62 *- Average Integrated Density for iNOS images.* 82

Figure 63 *- Average Integrated Density for Arg1 images.* 82

Figure 64 *- Examples of iNOS expression around 50% Water, gel-reinforced implants.* 83

Figure 65 *– Examples of Arg1 expression around 75% Water, gel-reinforced implants.* 84

Figure 66 *- Scanning Electron Micrographs of PTS with recording devices incorporated* 88

List of Tables

Table 1 *- Summary of the iterations of PTS Fabrication.* 38

Table 2 *- Antibodies used for flow cytometry* 50

Table 3 *- Antibodies and immunohistochemistry information used in pHEMA implant experiments.* 56

Table 4 *- Recipe of pHEMA/GMMA hydrogels with varied pre-polymerization water content. 82.5% water group is shown but was not used in the implant study.* 66

Table 5 *- Average stiffness values (kPa) for materials used in this study. Showing hydrated (left) and lyophilized (right) stiffness values. 82.5% water group is shown but was not included in the implant study.* 68

Table 6 *- Implant groups used.* 69

Table 7 *- Antibodies and immunohistochemistry information used in pHEMA/GMA implant experiments.* 71

Table 8 *- Imaging settings for each marker.* 72

Acknowledgements

The work in this dissertation would not be possible without the guidance, mentorship, support, and companionship of many friends, coworkers, and collaborators. First, I'm thankful to Bill Shain, Seattle Children's Research Institute, and the Center for Sensorimotor Neural Engineering (now the Center for Neurotechnology) for supporting me for the first two years of my PhD and fostering a solid foundation studying CNS tissue histology around implanted devices. Second, I'm grateful to have had the opportunity to participate in an international collaboration with Ulrich Hofmann's lab at the University of Freiburg in Freiburg, Germany. Special thanks to Yijing Xie for being an amazing mentor during my time there, and to all of the great friends I met at the Greencity Boardinghouse and the Boulderkitchen climbing gym in Sankt Georgen. Third, I'm thankful for my collaborators at San Diego State University: Dr. Sam Kassegne and Maria Vomero.

After Bill retired in 2015, I wasn't sure where to go. I'm eternally grateful to my advisors Buddy Ratner and James Bryers for welcoming me into their labs with such short notice, without any of my own funding, and for mentoring me for the remainder of my PhD. They allowed me to explore my own research project, merging my old research interests with theirs. There's no way I could have made it without their support. Thanks to Eric Chudler for pointing me in their direction in my time of need.

I'm thankful to Neal Beeman, Alex Chen, Marvin Mecwan, Le Zhen, Lars Crawford, Zak Wescoe, Savannah Lawton, Becky Darrow, Billana Hwang, Aya Pusic, Alissa Bleem, Ruying Chen, and all of the other Ratner and Bryers lab members who provided feedback, guidance, mentorship, and support in my research.

I'm thankful to my collaborators – especially Rob Robinson, Tyler Maxfield, and the rest of Steve Perlmutter's lab, who were always open to new research questions both during my time with Bill and with Buddy and James. Thanks to Zin Khaing, Jeffrey Hyde, Lindsay Cates, Dane DeWees, and the rest of Christoph Hofstetter's lab for their collaboration. I would like to acknowledge Daniel Passos and the Parsek lab for assistance and allowance to use their confocal microscope, which I used to obtain many of these images.

Lastly, I'm forever indebted to my family and friends for support and companionship. I couldn't have done it without them.

Dedicated to Lisa Willman

Chapter 1: Introduction

1.1 Motivation

Neural interfaces have made possible important observations on neuron activity, disclosing fundamental knowledge of the brain and nervous system and offering great potential to reduce the burden of many neurological conditions. In the United States, nearly 2 million people are living with limb loss (Ziegler-Graham, MacKenzie, Ephraim, Travison, & Brookmeyer, 2008), an estimated 282,000 people are living with spinal cord injury (National Spinal Cord Injury Statistical Center, 2013), and approximately 6 million people have had a stroke, with ~795,000 people having a new or recurrent stroke each year (Mozaffarian et al., 2015). Many of these people rely on the assistance of loved ones or personal aides. Using neuronal control signals for assistive devices, neural interfaces could restore their mobility and independence. Neural control of a robotic arm for reach and grasp tasks has already been demonstrated in humans with tetraplegia (Collinger et al., 2013; Hochberg et al., 2012). Also, many studies have shown evidence that neural interfaces can assist in stroke rehabilitation, reviewed by (Soekadar, Birbaumer, Slutzky, & Cohen, 2014).

1.2 Background

Unfortunately, inflammatory central nervous system (CNS) responses limit a number of potential therapeutic interventions including long-term neural recording devices and may worsen outcomes following ischemic and traumatic damage to the CNS. Reactive tissue responses that develop around neural implants are often responsible for time-dependent declines in electrode performance (Barrese et al., 2013; Freire et al., 2011; Prasad et al., 2012; Ward, Rajdev, Ellison, & Irazoqui, 2009). These tissue responses are largely attributed to activated microglia and astrocytes. Initial tissue damage from implant insertion recruits circulating macrophages, and activates nearby microglia, which have been described as the tissue-resident macrophages of the brain (Aguzzi, Barres, & Bennett, 2013). Activated microglia and macrophages migrate quickly towards the implant where they release cytokines and other signals that activate and

recruit astrocytes to the area of the implant. Over the course of a few weeks in rats, the acute stage of the tissue response subsides and gives way to a chronic reactive tissue response around the implant. This tissue response can be compared to foreign body responses seen in other tissues. The mass of glial cells and deposited extracellular matrix around the neural recording device (Biran, Martin, & Tresco, 2005; Turner, 1999) results in an increased impedance seen by the electrodes (Ward et al., 2009; Williams, Hippensteel, Dilgen, Shain, & Kipke, 2007), and a decrease in recording signal quality over time (Freire et al., 2011). Most electrodes are rendered useless over the course of months to a few years in primates (Barrese et al., 2013). Controlling this neuroinflammatory response around implanted devices could reduce glial encapsulation, allowing for longer functional lifetimes for recording devices.

The first two years of my PhD were spent advised by Dr. Bill Shain, studying tissue responses to various implanted neural recording devices **(Chapter 2)**. During my 2nd year, I participated in a research collaboration at the University of Freiburg, Germany **(Chapter 3)**. After Bill Shain retired in the Spring of 2015, I joined the labs of Dr. Buddy Ratner and Dr. James Bryers. They had been studying inflammation and the foreign body reaction to implanted biomaterials, specifically precision-engineered porous templated polymer scaffolds. These had never been tested in the central nervous system, so I applied their biomaterials to my research goal: improving tissue responses around neural implants **(Chapters 5-8)**. While working in the Ratner & Bryers labs, I participated in a brief collaboration with Dr. Christoph Hofstetter's lab, characterizing inflammation after spinal cord injury **(Chapter 4)**.

Chapter 2: CNS Tissue Response to Implanted Neural Recording Devices

2.1 Introduction

For the first two years of my PhD, I worked in the lab of Dr. Bill Shain, where I studied tissue responses to various neural implants, using Electrical Impedance Spectroscopy (EIS), Optical Coherence Tomography (OCT), and post-hoc immunohistochemistry (IHC). We participated in multiple collaborative research projects, described below.

2.2 – Project 1 – poly(trivinyltrimethylcyclotrisiloxane): GVD's Exilis™ Coating to Reduce Brain Tissue Responses and Improve Utah Array Functionality in rat cortex

This project is the result of a collaboration between UW (Ian Dryg & Bill Shain), University of Utah (Loren Reith), and GVD Corporation (Shannan O'Shaughnessy).

Background

Devices for neural recording and stimulation are typically made of a conductive material (e.g. tungsten, platinum-iridium), and coated with an electrical insulator (e.g. teflon, polyimide, parylene). Electrode sites are left exposed to allow current to pass for recording or stimulation. GVD Corporation develops Chemical Vapor Deposition (CVD) coatings with non-stick properties for various applications. The overall goal of this project was to examine the impact of GVD's Exilis™ coating compared to traditional parylene coated arrays on performance of microfabricated neural prosthetic devices.

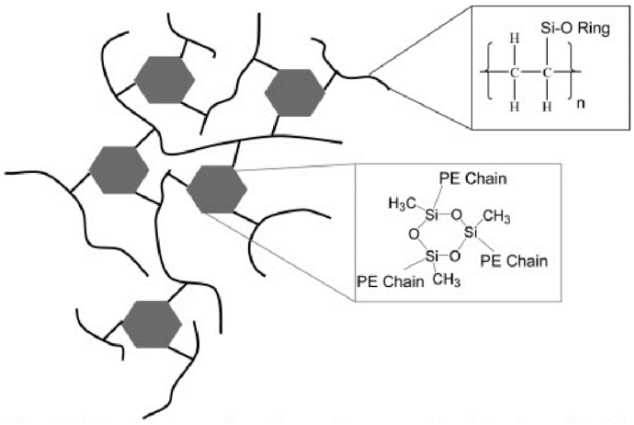

Figure 1 *– Schematic representation of the matrix structure of the Exilis™ polymer film. Hexagonal units represent the intact siloxane rings, which act as cross-linking moieties for multiple carbon backbone chains. From (W. Shannan O'Shaughnessy, Gao, & Gleason, 2006).*

The Exilis™ material is inspired by the success of organosilicon polymers such as the widely used poly(dimethylsiloxane). Exilis™ is created by initiated Chemical Vapor Deposition (iCVD) using trivinyltrimethylcyclotrisiloxane as a monomer and *tert*-butyl peroxide as a free-radical-generating initiator, generating a highly cross-linked matrix material **(Figure 1)** (W. Shannan O'Shaughnessy et al., 2006). It's been demonstrated as a stable, electrically insulating, flexible, neural cell-compatible material suitable for implanted device coatings (W S O'Shaughnessy, Murthy, Edell, & Gleason, 2007). In this study, we tested its performance *in-vivo*. **Hypothesis: Devices coated with Exilis™ result in decreased tissue responses and better device performance than Parylene-coated devices.**

Methods

Six Utah Arrays (3 Exilis™ coated, 3 Parylene coated) were implanted into motor cortex of 6 rats (one implant per animal). Impedance measurements and neural recordings were taken ~twice per week. After ~6 weeks, animals were euthanized and tissue histology was performed to analyze tissue responses as described in the appendix. Neural recordings were sampled at 25 kHz and raw signals saved. In MATLAB, raw signals were filtered from 300 Hz to 3 kHz and processed through a custom-made spike sorting algorithm (FMM Sorter) developed by Dr. Larry

Carin's group (Carlson et al., 2014). Verification of spike sorting was performed using windowed discrimination (Tucker-Davis Technologies).

Results

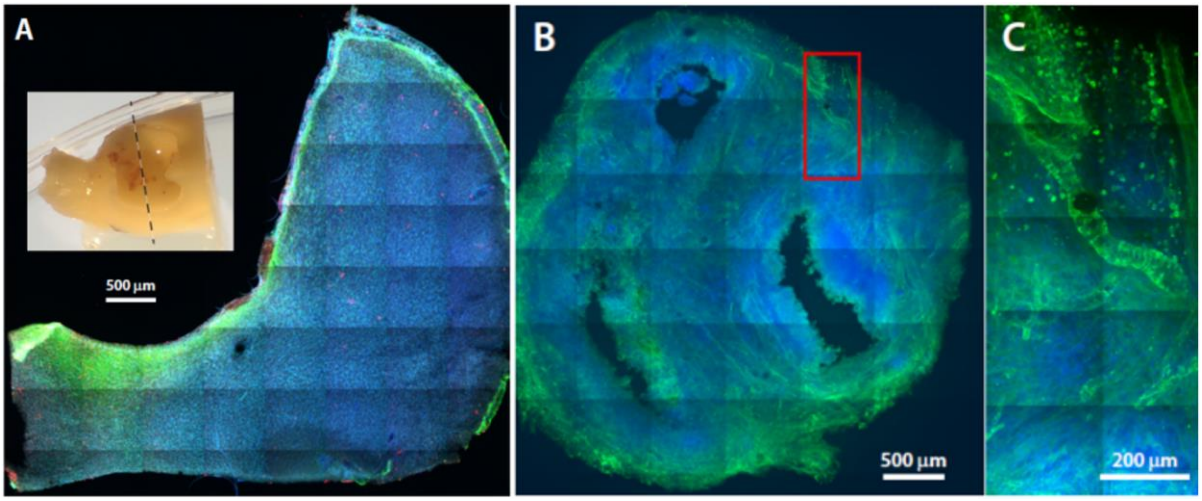

Figure 2 *- Histology of rat brains after implantation with Utah Arrays.Implanted devices in rat U07 (shown) and 3 other rats were encapsulated in tissue mass.* ***(A)*** *Astrocyte-rich cellular wall that separated the brain from the encapsulating mass. Inset is a photo of the brain illustrating the large space created by the encapsulating mass. Dashed line indicates the approximate position of the tissue slice that was processed and imaged to make the montage.* ***(B)*** *A montage of the encapsulating mass.* ***(C)*** *Region indicated by the red box in* ***B*** *illustrating both the high vascular nature and nuclear/cell density of the mass. Astrocytes (GFAP,green), Microglia (Iba1,red), Cell Nuclei (Hoechst,blue).*

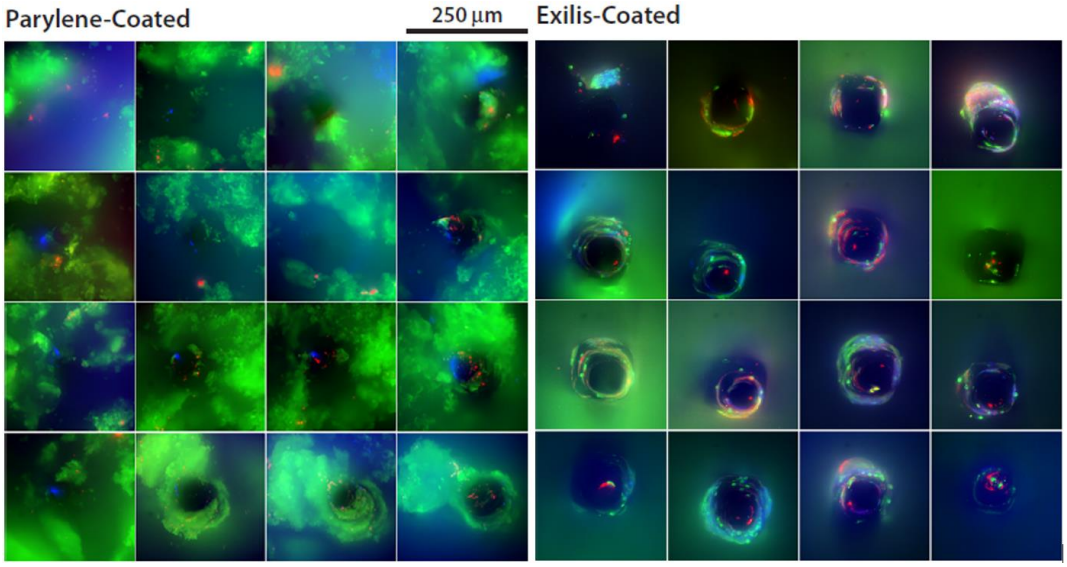

Figure 3 *- Stained cells on explanted Utah Arrays. Two-dimensional projections of shank images from representative parylene- and Exilis™-coated devices demonstrating that Exilis™ coatings reduced reactive cell response and attachment. Processing used same methods as for brain tissue. Astrocytes (GFAP; green), Microglia (Iba-1; red), Cell Nuclei (Hoechst; blue).*

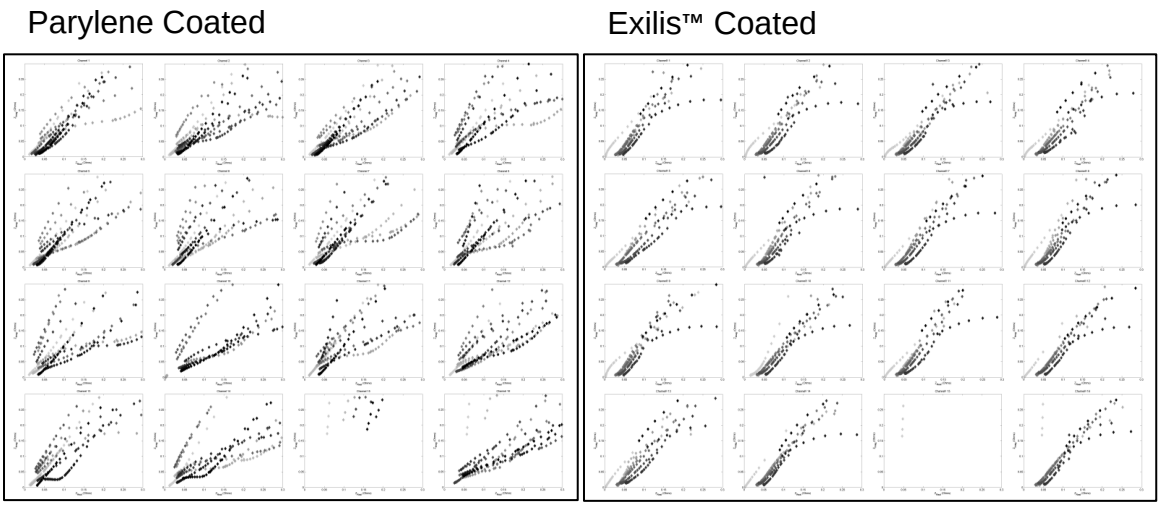

Figure 4 *– Nyquist plots summarizing complex impedance spectroscopy (CIS) results from two representative animals (16 electrodes per device). Exilis™-coated devices (right) showed more stable spectral impedance over time than Parylene-coated devices (left). Each set of symbols represents data collected on a single day, with shades of grey indicating time after device insertion. Darker shades indicate longer times since implant date. Axes are same for all plots.*

Neural Recordings: Output of the FMM Sorter showed no signals that appeared to be single units. These findings were verified using TDT's BoxSort function to perform windowed discrimination on the data. Because no single-unit activity was recorded on any devices, the effect of Exilis™ coatings on recording capabilities is unclear.

Tissue Histology: Four out of six devices were surrounded by encapsulation tissue and pushed out of the brain, which has previously been reported with Utah Arrays (Barrese et al., 2013). The most extreme case is shown in **Figure 2**. This encapsulation tissue was not normal brain tissue - there was no positive neuron labeling, it was highly vascularized, and contained very high cell density. Explanted devices were labeled for cellular debris **(Figure 3)**, which showed less cellular attachment to Exilis™ coated devices.

Impedance Measurements: Reactive tissue responses have been associated with increases in spectral impedance over time (Williams et al., 2007). Exilis™-coated devices showed more stable spectral impedance over time than Parylene-coated devices **(Figure 4)**, suggesting decreased reactive tissue responses to Exilis™-coated devices.

Discussion/Conclusions.

Exilis™-coated devices showed more stable impedance and less cellular attachment, suggesting the **Exilis™ coating likely improves reactive tissue responses.** However, due to the large amounts of tissue encapsulation, these findings should be verified. We interpret the lack of neural signals as being due to the large amounts of non-neural tissue encapsulation around the arrays.

2.2 – Project 2 – Glassy Carbon Micro-ECoG Arrays

This project is the result of a collaboration between CSNE members at UW and San Diego State University (SDSU). People involved: Ian Dryg, Bill Shain, Maria Vomero, Sam Kassegne, Tyler Maxfield, and Steve Perlmutter.

Background

A new material for neural electrodes, glassy carbon (GC) provides tunable impedance based on processing, intended to optimize charge injection capabilities (Kassegne et al., 2015). However, few studies had examined brain tissue's response to GC. Through a collaborative effort, members of the Kassegne, Shain, and Perlmutter labs designed a micro-encephalography (µECoG) array for recording local field potentials from the surface of a rat brain, featuring GC electrodes on a polyimide substrate with platinum traces. **Hypothesis: glassy carbon µECoG electrodes show favorable tissue responses.** These experiments validating the biocompatibility of glassy carbon will open the door for use of glassy carbon electrodes in future studies.

Methods

Polyimide-based µECoG arrays with either glassy carbon and platinum electrodes were fabricated by our collaborators at SDSU. In between electrodes and traces, "breathing holes" were engineered into the polyimide to allow tissue to grow through the implant. In Dr. Perlmutter's lab at UW, arrays were implanted subdurally over rat motor cortex **(Figure 5)**.

Spectral impedance was monitored over time. After 6 weeks, rats were euthanized for tissue histology as described in the appendix, taking coronal sections **(Figures 6 & 7)**. Microglial morphology was analyzed using the FARSIGHT Toolkit (Luisi, Narayanaswamy, Galbreath, & Roysam, 2011), a cell tracing software developed in collaboration between Bill Shain and Badri Roysam (University of Houston). Volumes of tissue at varying depths below the brain's surface (and thus the implant) were analyzed and populations of microglia were separated into four groups based on morphology. Groups ranged from microglia in their resting, normal state (Group 1: Ramified Microglia) to fully activated microglia (Group 4: Ameboid Microglia) **(Figure 8)**.

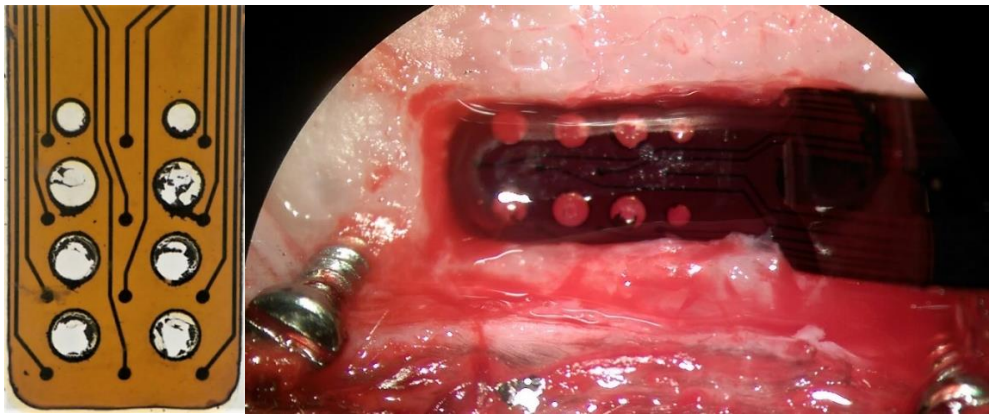

Figure 5 *– Device schematic (left) and image of surgical implantation of the glassy carbon array onto the surface of the brain (right).*

Results

Immunofluorescent staining of glial cells and neurons showed an increase in GFAP (Astrocyte) staining on the brain's surface directly underneath the polyimide array, but no extensive tissue damage was caused. **Figure 6 and Figure 7** show brain histology underneath "breathing holes" **(Figure 6)**, showing tissue growing through the holes; and underneath the GC electrodes **(Figure 7)**, showing no reaction to the GC electrodes compared to the polyimide.

To analyze the extent of microglial activation underneath a surface array, we used the FARSIGHT Toolkit to group microglia into groups based off morphological markers such as:

number of processes, length of processes, number of branches, length of branches, and cell body shape and volume **(Figure 8)**. Tissue underneath a surface array exhibited higher number of total microglia at most tissue depths up to 1.3mm, and microglia within 130µm of the surface array were skewed towards an activated/ameboid morphology, indicating higher levels of activation. These results suggest that the presence of a surface array is sensed even by cells over a millimeter deep into cortex, but only especially activates microglia within approximately 130µm of the implant. Unfortunately, this analysis was only performed extensively in one animal.

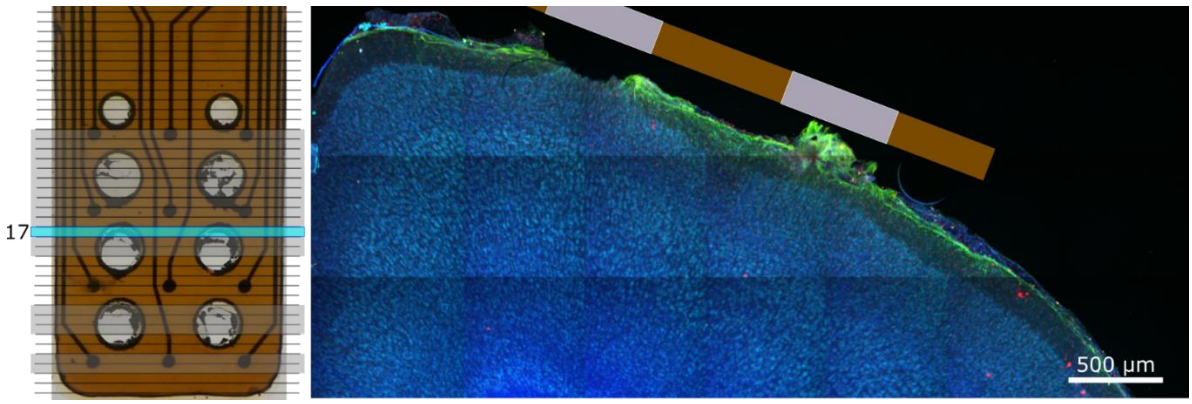

Figure 6 *- Tissue growth through array's breathing holes can be used to verify electrode locations. Coronal brain slice showing tissue growth through device's breathing holes (inset cartoon shows polyimide in brown and breathing holes in light grey). Left: Cartoon of device showing position of the current slice (cyan) and all processes slices (grey).*

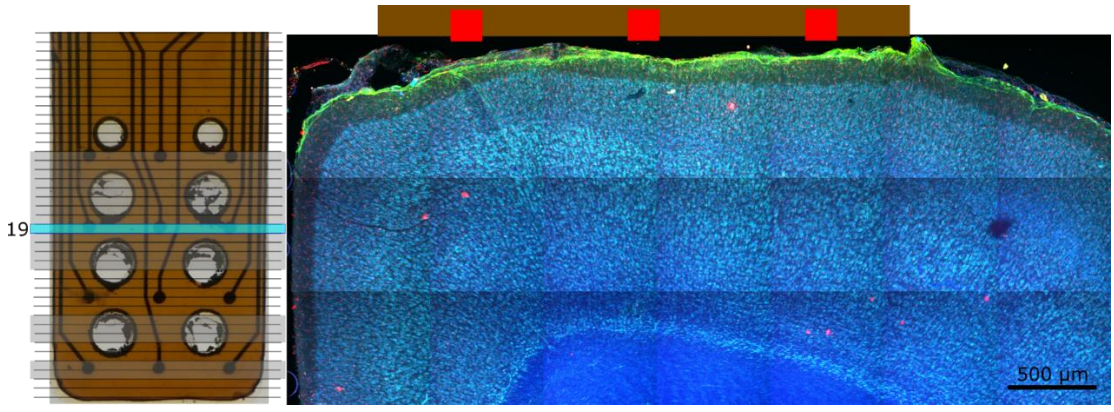

Figure 7 *- Increased GFAP signal beneath the array, but tissue responses appear minimal. Coronal brain slice showing tissue underneath glassy carbon electrodes (inset cartoon shows polyimide in brown and GC electrodes as red squares). Left: Cartoon of device showing position of the current slice (cyan) and all processed slices (grey).*

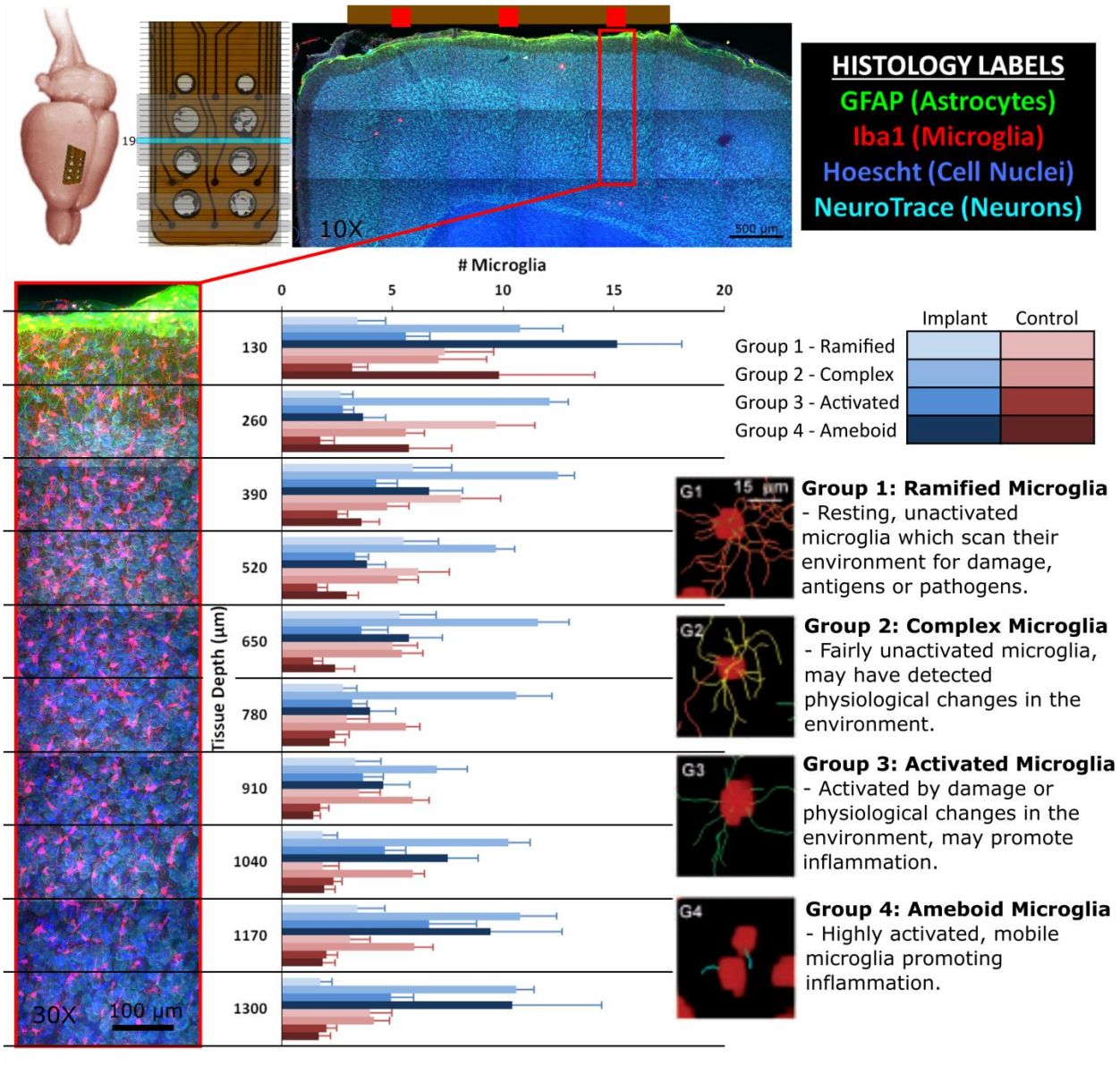

Figure 8 *- FARSIGHT analysis of microglial morphology underneath implanted µECoG array vs. control tissue (no implant). 130µm thick coronal slices were taken along the length of the array and immunolabeled for astrocytes (GFAP, green), microglia (Iba1, red), neurons (NeuroTrace, cyan), and cell nuclei (Hoechst, blue). Immunolabeled slices were imaged at 10X (top) and then at 30X (bottom-left) underneath electrodes by confocal microscopy. Microglial morphology was analyzed using the FARSIGHT toolbox, grouping microglia into 4 groups based on a multitude of morphological features related to their activation (bottom-right).*

This work resulted in the following publications (Goshi, Vomero, Dryg, Seidman, & Kassegne, 2016; Vomero et al., 2016):

Noah Goshi, M. Vomero, **Ian Dryg**, S. Seidman, Sam Kassegne. "Modeling and Characterizing of Tissue/Electrode Interface in Capacitive ECoG Glassy Carbon Electrodes." ECS Transactions. (2016)

Maria Vomero, **Ian Dryg**, Tyler Maxfield, William Shain, Steve Perlmutter, Sam Kassegne. "In-Vivo characterization of Glassy Carbon-Electrodes and Histological Analysis of Brain Tissue after Chronic Implants." ECT Transactions. (2016)

2.3 – Project 3 – Actively controlled release of Dexamethasone from neural microelectrodes in a chronic in vivo study

This project is the result of a collaboration between UW CSNE (Ian Dryg & Bill Shain), the Neuroelectronic Systems Lab at University of Freiburg, Germany (Yijing Xie & Ulrich Hofmann), and IMTEK in Freiburg, Germany (Christian Boehler, Thomas Stieglitz, & Maria Asplund) over Summer 2014.

Background:

One method for improving neural electrode performance is to electrochemically polymerize conducting polymer films onto the surface of the electrodes. This provides a softer barrier between the stiff electrode material and the soft brain tissue, and effectively increases the surface area of the electrode, lowering impedance and increasing charge storage capacity for stimulation. Another promising use of conducting polymers is for controlled delivery of an entrapped drug by electrical stimulation. Dexamethasone is a commonly used corticosteroid for controlling inflammation and is routinely delivered when electrodes are implanted in human patients, such as a deep brain stimulation electrode for Parkinson's Disease. In this study, we demonstrate the controlled release of Dexamethasone from a PEDOT-coated flexible probe and assess long-term recording capability and tissue responses.

Methods:

Twelve rats were implanted with flexible polyimide penetrating electrode arrays, using a stiff trocar to enable implantation into cortex. Implanted electrodes featured active (stimulated) PEDOT/Dexamethasone, passive (not stimulated) PEDOT/Dexamethasone, active PEDOT/PSS, passive PEDOT/Dexamethasone, or no polymer coating (Iridium-Oxide electrodes: IrOx). Drug was actively released using cyclic voltammetry once per week.

Impedance of the electrodes and neural recordings were monitored once per week throughout the study. After 12 weeks, animals were euthanized for histological evaluation.

Results:

All implants maintained stable impedance and Local Field Potentials (LFPs) over the course of the study. All groups showed similar GFAP fluorescence, except IrOx electrodes that showed lower GFAP intensity at the interface. For microglia, both PEDOT:Dexamethasone groups and IrOx groups showed lower ED1 than PEDOT:PSS groups. This suggests the controlled release of Dexamethasone was effective in reducing activation of microglia and macrophages **(Figure 9)**.

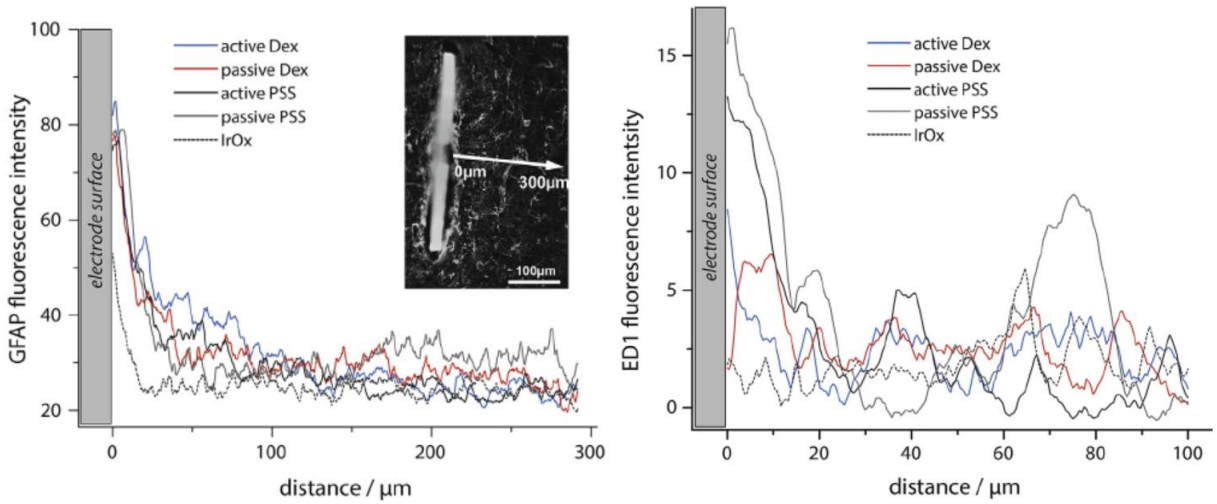

Figure 9 *- Quantified histology of Dex-release implants. Fluorescence of GFAP (astrocytes, left), and ED1 (activated microglia and macrophages, right) vs. distance from the electrode surface. From (Boehler et al., 2017).*

Implants that actively released Dexamethasone showed the least distance between the interface and labeled neurons, although there was no statistically significant difference among all groups **(Figure 10)**.

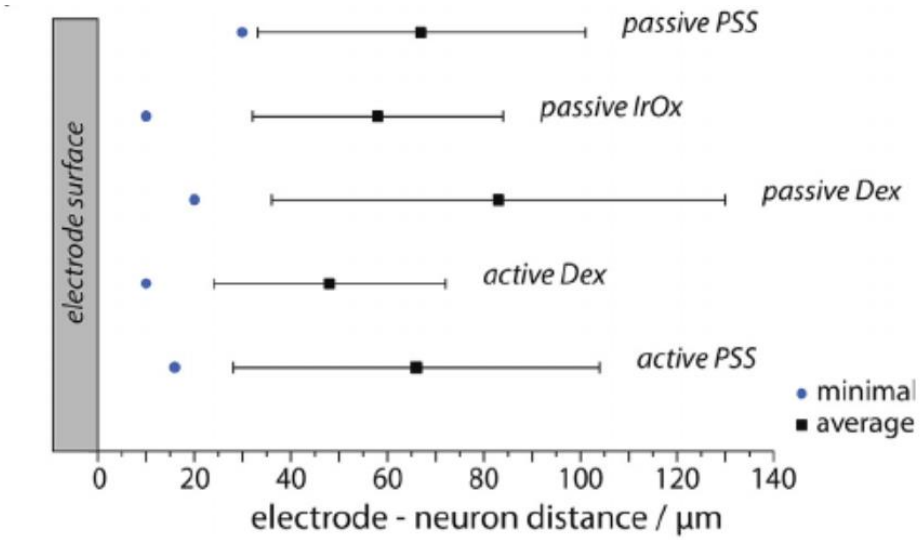

Figure 10 *- Quantified histology for Neurons, based on NeuN fluorescent staining. From (Boehler et al., 2017).*

My main roles in this project were animal care and handling and performing all the cardiac perfusions.

<u>This work resulted in the following publications (Boehler et al., 2017):</u>

C. Boehler, C. Kleber, N. Martini, Y. Xie, **I. Dryg**, T. Stieglitz, U. Hofmann, M. Asplund. "Actively controlled release of Dexamethasone from neural microelectrodes in a chronic in-vivo study." Biomaterials (2017). In print.

Chapter 3: Optical Coherence Tomography for In-Vivo Monitoring of Neural Implants

3.1 Introduction

This project is the result of a collaboration between UW CSNE (Ian Dryg & Bill Shain) and the Neuroelectronic Systems Lab at University of Freiburg, Germany (Yijing Xie & Ulrich Hofmann) over Summer 2014.

Background

The current state of the art for visualizing tissue responses surrounding brain implants in animals utilizes immunohistochemistry and confocal microscopy, which can only be performed after sacrificing the animal. Monitoring tissue responses in real-time could reveal important features of tissue responses, informing improvements in electrode design. Optical Coherence Tomography (OCT), an imaging technique commonly used in ophthalmology, has been adapted for imaging and mapping of brain tissue (Xie et al., 2013). Here, for the first time, we use an implantable, single A-scan OCT system to achieve real-time, *in vivo* monitoring of tissue responses surrounding chronically implanted neural devices and verify those responses using traditional tissue histology. **Hypothesis: Reactive tissue responses surrounding neuroprosthetic devices can be monitored in real-time by OCT imaging.** As an additional experiment, we evaluate the effectiveness of CH4 plasma deposition on the implants on the foreign body reaction in the brain.

3.2 Materials and Methods

12 rats were implanted for 8 weeks with both a glass OCT imaging probe (made in-house) and a Michigan-style silicon probe (non-functional), angled at ~90 degrees from one another **(Figure 11)**, using a two-arm stereotactic frame. Three bone screws were placed on the contralateral side of the skull to provide stability for the headcap, and a ~10 mm long burr hole line was drilled in the skull for entry points of the two probes. Both probes were aligned in air and reflectance of the OCT signal from the silicon probe was confirmed. The silicon probe was implanted at an angle of 45 degrees moving in the caudal direction, and the OCT probe was

implanted at an angle of 45 degrees moving in the rostral direction. The OCT probe was advanced until reflectance from the silicon probe could be seen in the OCT signal at a distance of less than 1 mm. If the silicon probe could not be found, the OCT probe was removed, re-positioned, and advanced again. In initial surgical attempts, aligning the probes within brain tissue proved rather difficult but improved with practice. We determined that the angle between probes must be near 90 degrees (80-100 degrees), otherwise the reflectance signal was too weak to detect. Once probes were aligned within brain tissue, dental acrylic was used to stabilize both probes, and a dental acrylic headcap was built. The silicon probe was non-functional, so no connector was needed. The OCT imaging probe served as a port that could be disconnected from the OCT imaging system, and re-connected during imaging sessions. Between imaging sessions, the OCT port was wrapped with parafilm to prevent debris from filling the port. Before each imaging session, the parafilm was removed, the OCT port was cleaned using lens-cleaning solution, and the fiber optic cable leading to the OCT imaging system was plugged into the OCT port on the rat's head. OCT imaging was performed once per week for 8 weeks. After the final imaging session, rats were euthanized for tissue histology as described in the appendix. For this histology, both the OCT and silicon probes were captured within the same Saggital brain slice. To test the effect of the CH4 plasma coating of the probes on the foreign body reaction, the OCT probes were coated in half (n=6) of the animals.

3.3 Results and Conclusions

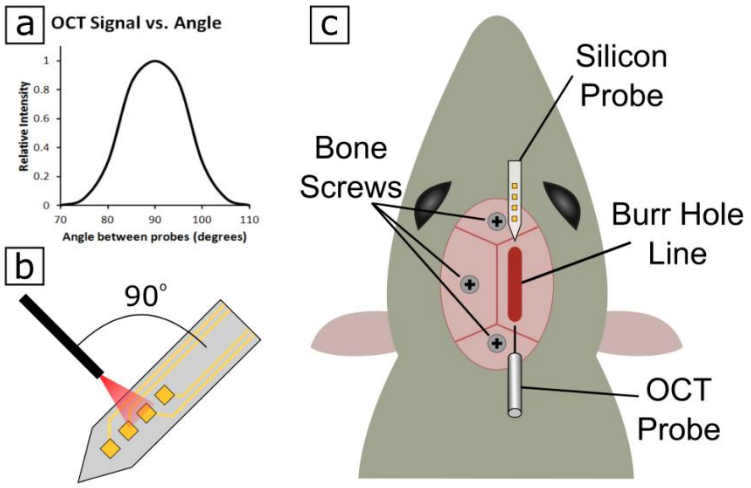

Figure 11 *– OCT Project surgical setup. (a,b) To detect the silicon probe with the OCT signal, probes had to be angled close to 90 degrees from one another, maximizing reflectance back into the OCT probe. (c) Top view of the surgical setup. A burr hole line was drilled to allow implantation of probes into brain tissue. The OCT probe and silicon probe were pre-aligned before advancing into brain tissue. The silicon probe was advanced first, then the OCT probe was advanced until the silicon probe could be detected in the OCT signal.*

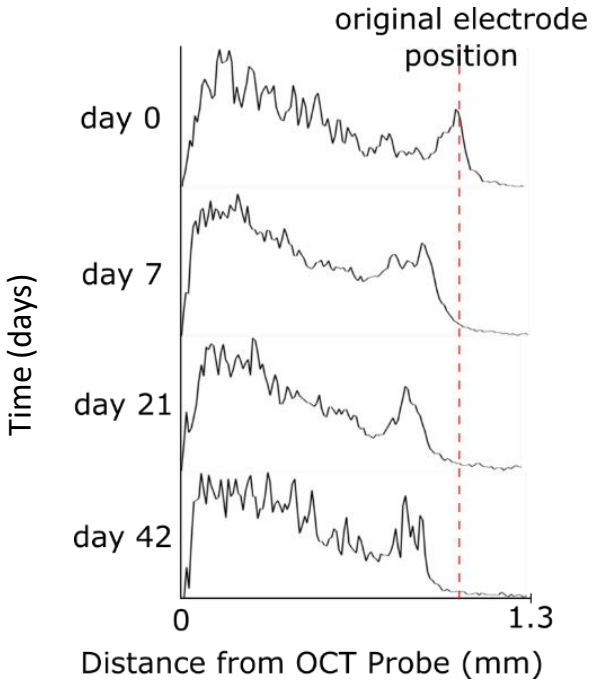

Figure 12 *- Changes in electrode position can be monitored using the OCT signal profile. Here, the distance between the OCT probe (x-axis = 0) and the Silicon Probe (peak on right of each profile) decreases over time (y-axis). If electrode position changes, neural recording quality may be affected.*

Our data suggests that OCT is capable of monitoring tissue *in vivo,* and some aspects of the OCT signal may correlate with imaging by traditional IHC. In **Figure 13** below, traditional IHC and the OCT signal are compared for two representative animals. In all IHC analyses, there exists a noted increase in GFAP and Iba1 signal at the location of the silicon probe (denoted by the solid red line). Surrounding the location of the silicon probe there exists a spike in OCT signal likely representing the scattering of light by the dense glial encapsulation. Although the overall glial scar can be seen in the OCT signal, individual glial cells could not be resolved. In addition to monitoring the development of the glial scar, OCT can also be used to track undesired movement of an implanted electrode, which may result in a loss of neural recordings due to lack of proximity to spiking neurons **(Figure 12)**.

Quantitative histological analysis of glial encapsulation around coated or uncoated OCT probed was somewhat inconclusive: coated OCT probes displayed a higher peak fluorescence indicating glial scarring. However, glial scarring seemed to extend less distance from coated probes (fluorescence stopped being significantly different at a closer distance to coated probes) **(Figure 14)**. This data is currently in preparation for publication.

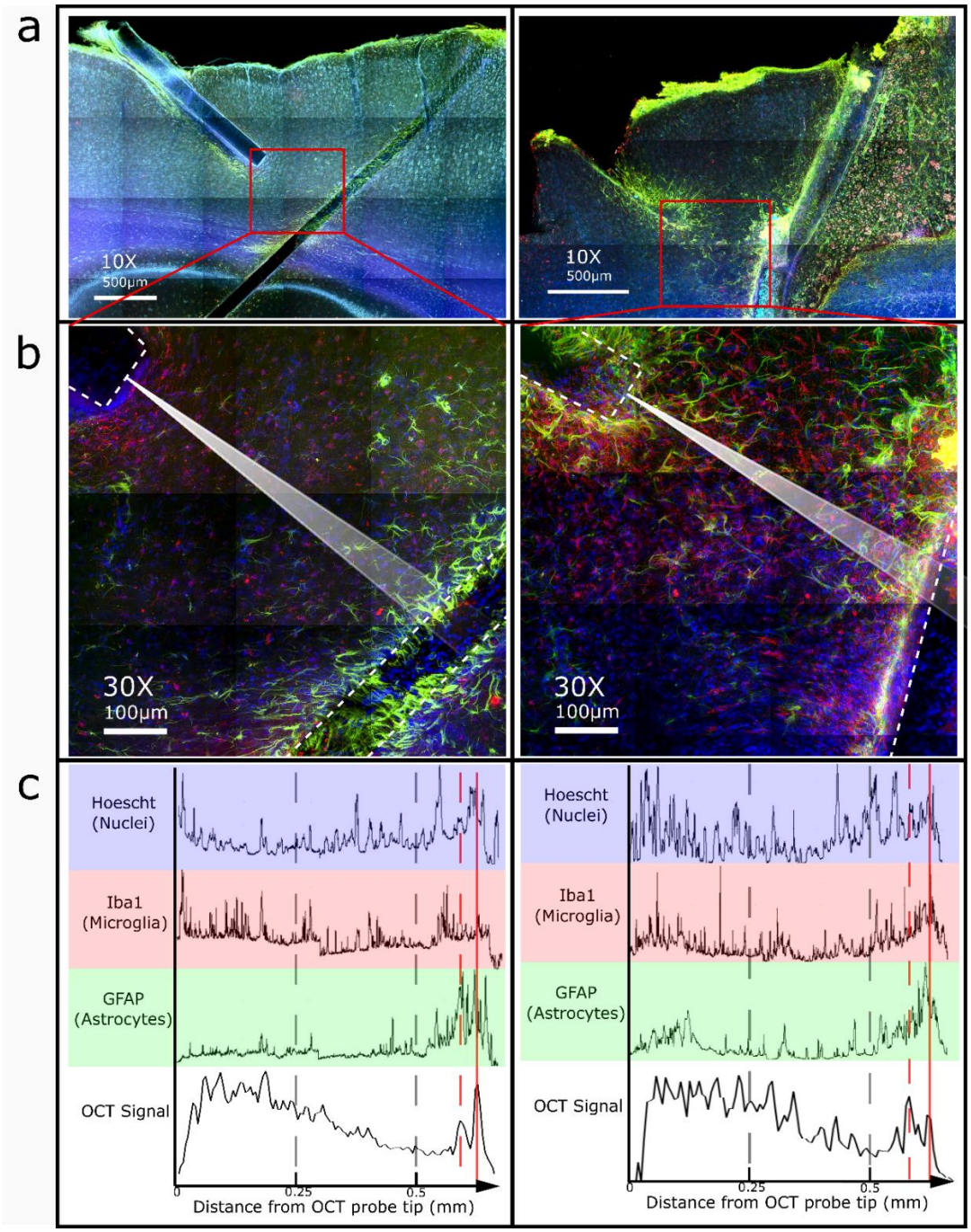

Figure 13 *- Comparisons between IHC (Sagittal sections in (a,b)) and OCT signal (c). (a) 10X scans show implant positions (scalebar: 500µm). (b) 30X scans of the tissue that had been imaged by OCT (illustrated by white beam) allows comparison between OCT signal and IHC profiles. Implants are outlined by dotted lines (scale bar 100µm). (c) OCT signal profile plotted below fluorescence profiles from the same tissue that had been imaged by OCT. The x-axis spans from the OCT imaging probe tip, through the tissue, and ends at the implanted silicon probe. Increases in fluorescence intensity profiles from labeled glial cells (dotted red line) match with the increase in OCT signal at the location of the silicon probe (solid red line).*

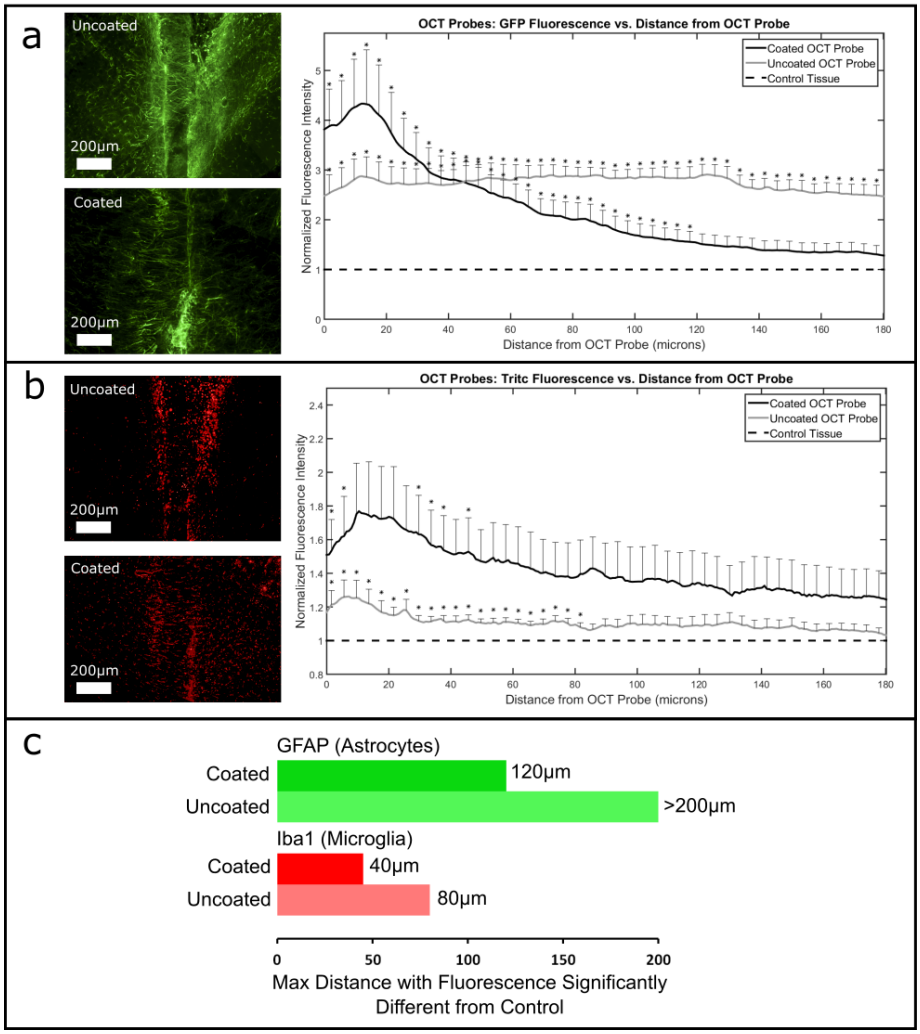

Figure 14 *- Effect of CH4 plasma coating on glial encapsulation of the OCT probes. Shown are quantified encapsulation by (a) astrocytes labeled by GFAP, and (b) microglia labeled by iba1, with representative uncoated and coated OCT probe images. The maximum distance with fluorescence intensity significantly different from control tissue is plotted in (c).*

This research resulted in the following conference presentations:

Ian Dryg, Yijing Xie, Michael Bergmann, Gerald Urban, William Shain, Ulrich Hofmann. (January 2017). Online Monitoring of Tissue Response to Plasma Coated Rigid Neural Implants using Fiber-based Optical Coherence Tomography. SPIE Photonics West, 2017, San Francisco, CA.

Chapter 4: Background on The Foreign Body Reaction & Porous Biomaterials

4.1 Change of labs:

In the Spring of 2015, my initial PI, Dr. Bill Shain retired. There had been conversations between Dr. Buddy Ratner and Dr. Shain about testing porous polymer scaffolds as coatings for brain implants. So, I joined the labs of Dr. Buddy Ratner and Dr. James Bryers to study this material and its potential for neural interfaces.

4.2 Background on The Foreign Body Response & Biomaterials

Whenever a medical implant or material is placed within the body, the biology will respond. This response is called the Foreign Body Response (FBR), which typically results in the implant becoming encapsulated in a dense, fibrous capsule. For some implants, this is not a major issue; but for implants that must interact with the biology, such as a chemical or electrical sensor, or a drug delivery device, this fibrous capsule can hinder the capabilities of the implant and ultimately lead to its failure.

As soon as the implant encounters biological fluids, host proteins adsorb to the surface of the implant, often resulting in abnormal conformations. When host cells interact with these abnormally conformed proteins, they are seeing an environment distinct from normal tissue. Within a few hours, neutrophils enter the implant site and produce cytokines, chemokines, and reactive oxygen species in reaction to the implant they consider to be foreign. Over the course of days, circulating monocytes and tissue resident macrophages are recruited to the implant site and release cellular signals promoting inflammation and recruiting fibroblasts to the area. Macrophages undergo frustrated phagocytosis as they are unable to engulf such a large body, and fuse together to form foreign body giant cells (FBGCs). Fibroblasts deposit collagen around the implant, and along with the cellular layer of FBGCs, form a dense capsule around the implant, walling it off from the rest of the tissue **(Figure 15)** (Grainger, 2013).

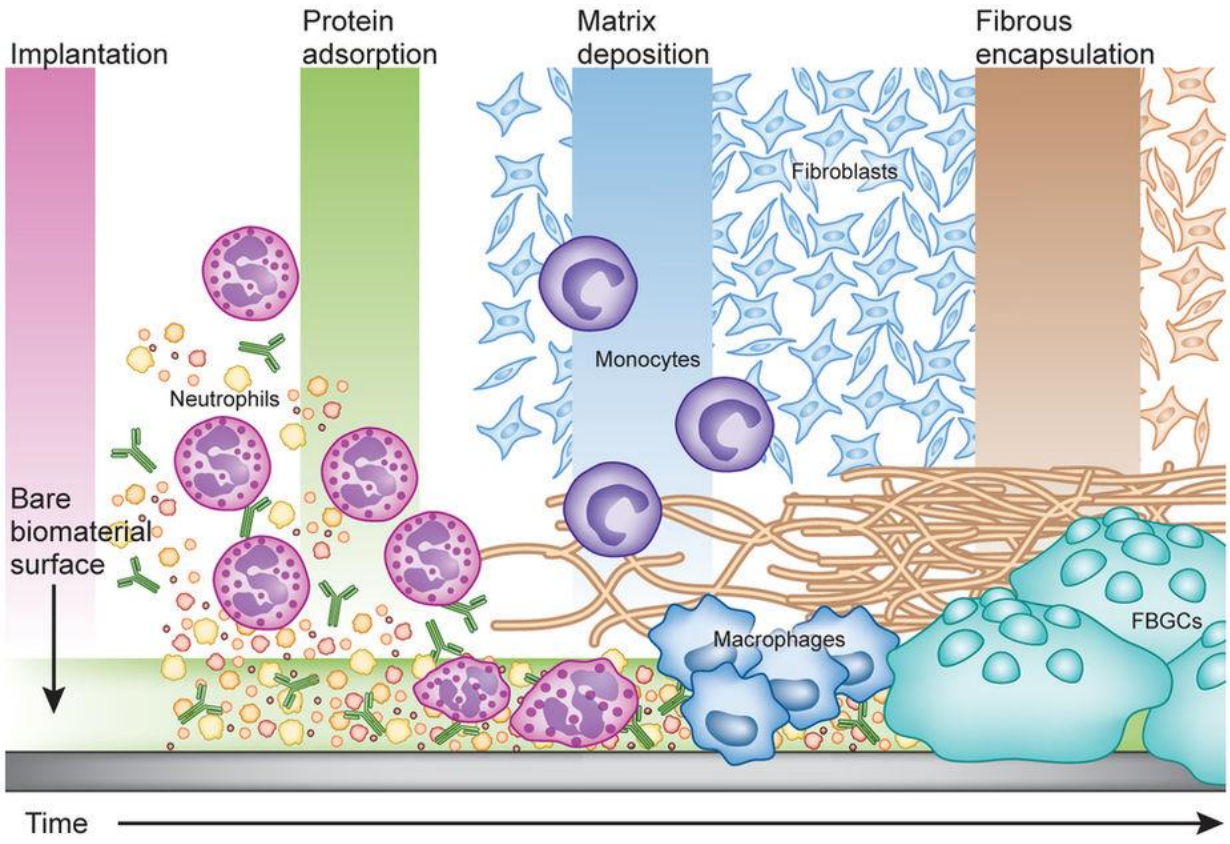

Figure 15 *- Schematic of the different phases of the FBR over time (Grainger, 2013).*

4.3 Background on Porous Biomaterials in the Ratner & Bryers Labs

The Ratner and Bryers labs are developing biomaterial platform technologies to control the phenotype of cells that orchestrate inflammation, *i.e.,* microglia, astrocytes, and inflitrating macrophages. Influenced by their microenvironment, macrophages may become classically activated into a pro-inflammatory phenotype (M1) (Gordon, 2003; Hume et al., 2002; Mosser, 2003; Mosser & Edwards, 2008; Mytar et al., 1999), or alternatively activated into one of three phenotypes - M2a, M2b, or M2c (Doherty, Kastelein, Menon, Andrade, & Coffman, 1993; Gratchev et al., 2006; Munder, Eichmann, & Modolell, 1998; Murray, 2006; Stein, Keshav, Harris, & Gordon, 1992; Verreck et al., 2004) that are associated with wound healing and regulation of immune responses. Characterization of macrophage activation has mainly been based on *in vitro* studies, while macrophage phenotype during various phases of the *in vivo* inflammatory response is only now being investigated. Many believe that chronic inflammation is

brought on by an imbalance in the M1:M2 macrophage populations. Recent work suggests that certain mechanical and physical properties of tissue engineering constructs can enhance tissue regeneration by influencing macrophage phenotype. For example, 3D electrospun PLGA nanofiber meshes with various mechanical properties and pore sizes yielded different macrophage phenotypes: small (~20 μm) pores skewed towards M1-macrophages and larger (100 μm) pores modulated macrophages towards a mix of M1 & M2 (Bartneck et al., 2012). Furthermore, materials that induce more M2-macrophage cells may increase the success of remodeling and healing (Badylak, Valentin, Ravindra, McCabe, & Stewart-Akers, 2008; Brown, Ratner, Goodman, Amar, & Badylak, 2012; Brown, Valentin, Stewart-Akers, McCabe, & Badylak, 2009).

Porous Templated Scaffolds (PTS) (Bryers, Giachelli, & Ratner, 2012) are porous polymers where every pore is the exact same size, and pore interconnects are also uniform in size, with both parameters being adjustable (**Figure 17**). Originally developed by the NSF-funded UWEB ERC (1996-2007), PTS have gone on to applications in humans. We have made PTS from poly(2-hydroxyethyl methacrylate) (pHEMA) hydrogel, a biodegradable pHEMA-co-caprolactone (PCL), silicone elastomer, fibrin, alginate, and polyurethane; all with pore sizes ranging from 10-160 μm. We have studied the healing of these materials in multiple *in vivo* environments, including adult rat myocardium (Thomson et al., 2013), mouse subcutaneous skin (**Figure 19**) (Sussman, Halpin, Muster, Moon, & Ratner, 2014), mouse transcutaneous skin (Bhrany, Irvin, Fujitani, Liu, & Ratner, 2013; Y. Fukano et al., 2010; Yuko Fukano et al., 2006; Isenhath et al., 2007; Knowles et al., 2005; Underwood et al., 2011), human vaginal wall (Bota et al., 2010), canine sclera (Galperin, Long, Garty, & Ratner, 2013),and rabbit drilled femur defect model. Maximum vascular density (**Figure 18**) and minimum fibrosis are always noted for 35-40 μm PTS. Consistently, only 35 μm PTS show excellent healing, regardless of the polymer used or the implant site.

The fabrication procedure for PTS **(Figure 16)** is described elsewhere (Sussman et al., 2014). Briefly, poly(methyl-methacrylate) (PMMA) microbeads are sifted to obtain a population of beads that are monodispersed in size. A monodispersed population of beads are filled within a mold, typically between two glass slides with a Teflon spacer, commonly called a “slide-sized mold” in our group. The beads within the mold are sonicated to ensure close packing of the beads, then heated to sinter the beads together at connection points. The heating time and temperature can be varied to precisely control the diameter of the bead connections, which will eventually become the interconnections between pores in the final scaffold. After sintering, the material is at a stage called the “bead cake”. The empty space between beads in the bead cake is now filled with a monomer solution. To make a pHEMA scaffold, ingredients are HEMA monomer, the cross-linking agent (TEGDMA), a UV initiator (Irgacure), and water. The solution is polymerized with UV light, and PMMA beads are dissolved out using an organic solvent such as dichloromethane (DCM). The result is a crosslinked hydrogel scaffold with interconnected spherical pores running throughout the material **(Figure 17)**. Typically, after UV-polymerization, a “skin” of polymer surrounds the entire material because monomer solution infiltrates the space between sintered PMMA beads and the glass slide mold. This is remedied by scraping the entire outer surface with a razor blade, clearing the skin away and exposing the porous network. However, this skin formation can also be prevented by coating the glass slides with a thin layer of PMMA before filling with PMMA beads and sintering.

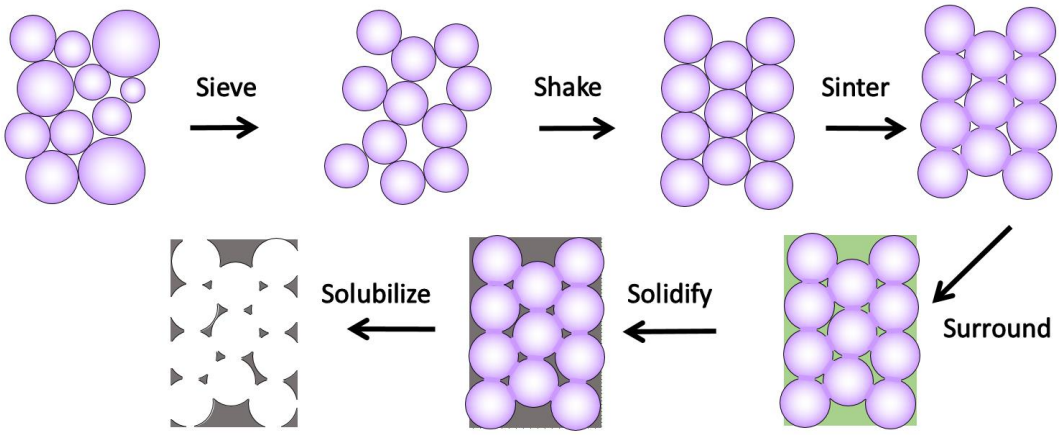

Figure 16 *- Fabrication process for PTS, otherwise known as the "6-S Process".*

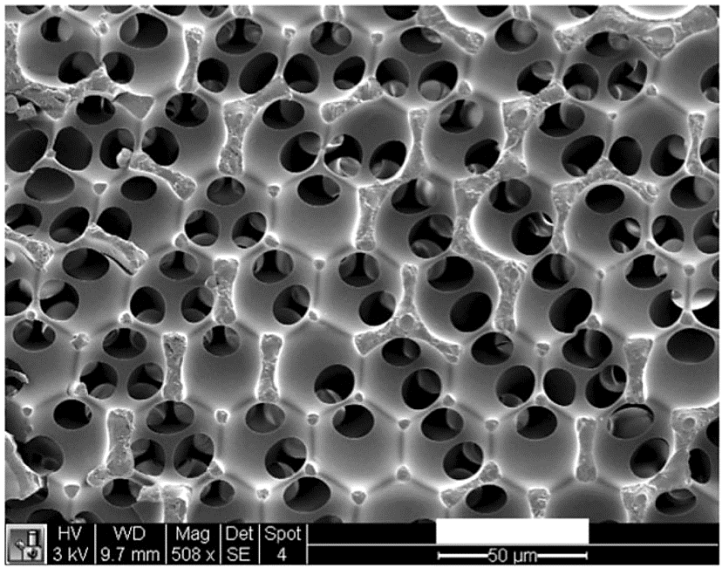

Figure 17 *- Oblique view of 35-µm pore pHEMA PTS ; Scale bar = 100 µm. (Bryers et al., 2012).*

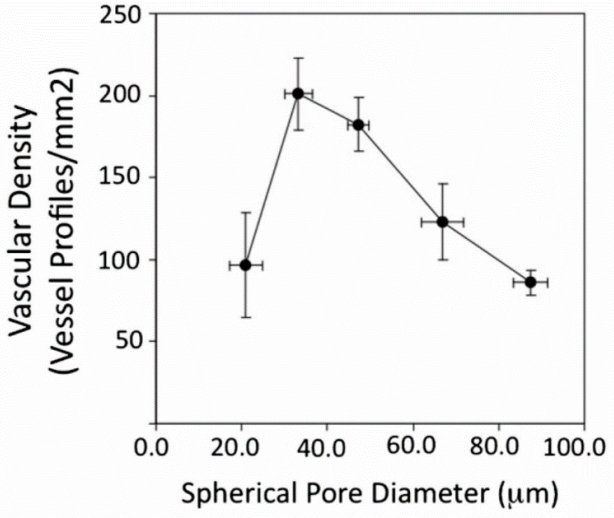

Figure 18 *- Intra-pore vascular density after 4 weeks of subcutaneous implantation varies with pore size. (A. Marshall et al., 2004).*

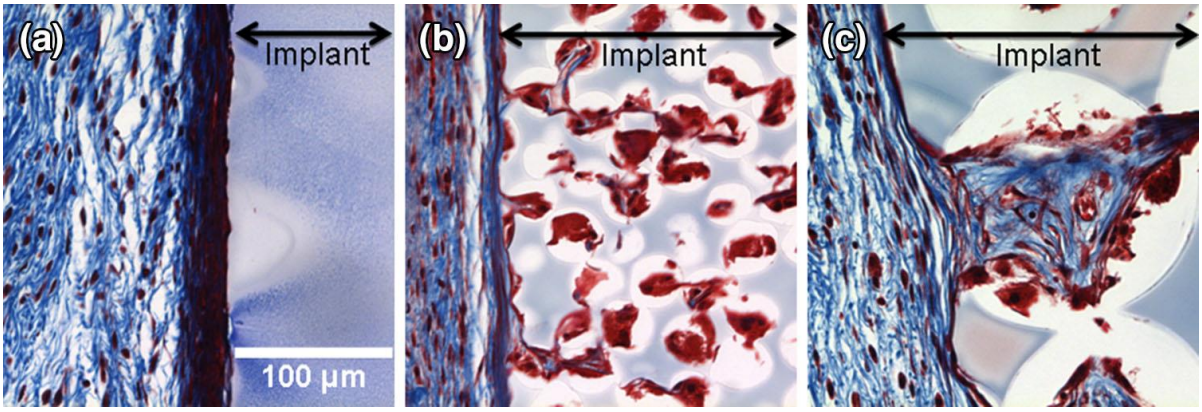

Figure 19 *- Foreign body reaction is reduced with porous implants (subcutaneous implants after 3 weeks in mice shown here). Representative Masson's trichrome photomicrographs show histological responses based on pore size. Collagen is shown in blue, cellular cytoplasm in red, and cell nuclei in black. (a) Non-porous implants have a dense FBC at the implant edge. (b) 34 µm porous scaffolds have a highly cellular infiltrate. (c) 160 µm porous scaffolds have a cellular infiltrate that is much richer in collagen than 34 µm scaffolds. (Sussman et al., 2014).*

PTS have shown great potential but have never been tested in the CNS. Because MØ can be influenced by PTS to promote healing in many tissues, and microglia are the brain's tissue-resident MØ, we hypothesize that PTS can influence CNS tissue responses towards healing as well. I briefly touch on the testing of PTS in the context of spinal cord injury

regeneration **(Chapter 6)**, and more extensively in the context of glial scarring around cortical implants **(Chapters 7 & 8)**.

Chapter 5: Development of Porous Neural Implants

For the remaining chapters, some version of PTS is used. Over time I have tried to improve and optimize the form of PTS. These iterations and optimizations are described here.

5.1 Methods of creating Porous Templated Scaffolds for Neural Interface Experiments

In this research, five different methods were used to fabricate porous templated scaffolds, summarized in **Table 1** and described below. The first method is the standard method used in the Ratner Lab to create porous scaffolds, described previously (Sussman et al., 2014). This was used to create scaffolds for the spinal cord injury project in Chapter 6. The other four methods were used to create rods of porous scaffolds, to be used in the neural implant studies in Chapters 7 and 8. These PTS rods are intended to eventually be used as a sheath around neural recording devices. Three of these methods used a tube-shaped mold and applied the normal fabrication method, or the “6-S Process”. The last method used a needle to punch rods out of a bulk porous scaffold.

Previous experiments have shown that just using glass as a mold results in the formation of a pHEMA surface skin around the scaffold, blocking the exterior from access to the internal porous structure. This skin formation can be circumvented by either scraping the skin off the PTS after fabrication, or by coating the glass with a thin layer of PMMA so the PMMA beads sinter to the PMMA layer, preventing pHEMA from getting between the two. Therefore, for method (2), a PMMA tube (300 µm ID, 600 µm OD) was inserted into the glass capillary tube mold to attempt to circumvent pHEMA surface skin formation. That mold was then filled with PMMA beads and rod-shaped scaffolds were created using the PTS fabrication procedure described in section 4.3 above. However, the PMMA tubing that was used as a secondary mold was too thick and resulted in poor porous structure: the surface showed lots of nonporous area, and pores within the implant were not well interconnected **(Figure 20, left)**. It is thought that this is because the PMMA tube had a lower melting temperature than the PMMA microbeads,

pulling some of the beads out of the main bead cake, and disconnecting the beads from sintering well to one another.

Table 1 *- Summary of the iterations of PTS Fabrication.*

Method	Description	Result	Used in:
(1) Bulk scaffold, punched or cut to size	Molded between 2 glass slides with a U-shaped Teflon spacer separating the slides a given distance.	This method is widely used in our lab to produce scaffolds. It results in a larger 3D porous templated scaffold. Polymer skin must be scraped off.	Chapter 6
(2) Molded within PMMA + glass tube	Molded within a PMMA tube, which is within a glass tube. Idea: prevent skin formation by sintering beads to the mold. Broke glass and washed in acetone to free the scaffold.	The mold (PMMA tube) melted too much, causing the porous structure to lose interconnectedness.	Chapter 7
(3) Punched with a needle	Used a 24-27 gauge needle (311-210µm inner diameter) to punch rods from a larger bulk porous scaffold.	Good porous structure, but rod shape was inconsistent. Incorporating a recording device would not be trivial but may be able to insert into the hydrated polymer rod after fabrication.	Chapters 7 and 8. May be used for future studies incorporating recording devices.
(4) Molded within a PMMA-coated glass tube	Filled glass tubes with PMMA dissolved in acetone, then sprayed the excess out with air. Used this as a mold, then broke glass and washed in acetone to free the scaffold.	PMMA coating is inconsistent in thickness due to the sintering step – it melts and accumulates in the bottom. Also, access to outer pores was inconsistent.	Not used.
(5) Molded within a glass tube + scraping	Used a glass tube as a mold. Broke glass mold to free the scaffold, then scraped the skin away.	Easy to break rods while scraping, but if done successfully, results in good porous rods with good access to pores. Can also incorporate a recording device during scaffold fabrication. However, some devices may not survive the fabrication process.	Not used. May be used for future studies incorporating recording devices.

For method (3), punching porous scaffold rods, a normal slide-sized scaffold was created, and a syringe-puller equipped with a liquid-filled syringe and needle of the desired inner diameter was used to slowly punch out a rod-shaped scaffold from the bulk material. Then, the

porous polymer rod was ejected from the syringe/needle, ready to be washed and lyophilized **(Figure 20, center)**. This method resulted in good porous structure, but sometimes the rod shape was imperfect or noncontinuous. Also, incorporating a microwire for electrophysiology within one of these punched rods has proven to be a big challenge. For this reason, the tube-molding method was re-explored.

For method (4), a smaller glass tube (300 µm ID) was used as a mold, and only a thin film of PMMA was used to coat the glass to prevent polymer skin formation **(Figure 20, right)**. To create the PMMA coating, PMMA was dissolved in acetone (10 g PMMA/50 mL Acetone), the glass capillary tube was filled with this solution, and sprayed out and dried using an air hose. This resulted in good porous structure internally, but the external surface still showed lots of nonporous area. In comparison with method (5), which involved no PMMA coating of the mold, there was not much improvement. Both methods (4) and (5) usually required scraping to reveal the porous structure, so method (5) is preferred at this time. A comparison of method (4) without scraping and (5) with scraping are shown in **Figure 21**.

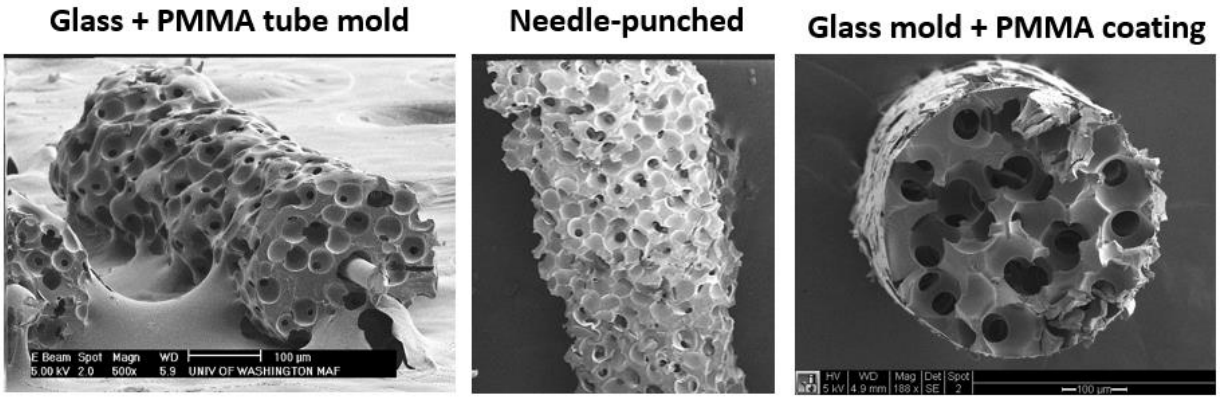

Figure 20 *- Representative samples of glass + PMMA tube molded (left), needle-punched (center), and glass + PMMA coating molded (right) porous rods. Molded porous rods showed better rod-shaped structure but often poorly interconnected porous structure, while punched porous rods showed better porous structure but sometimes had poor rod-shaped structure.*

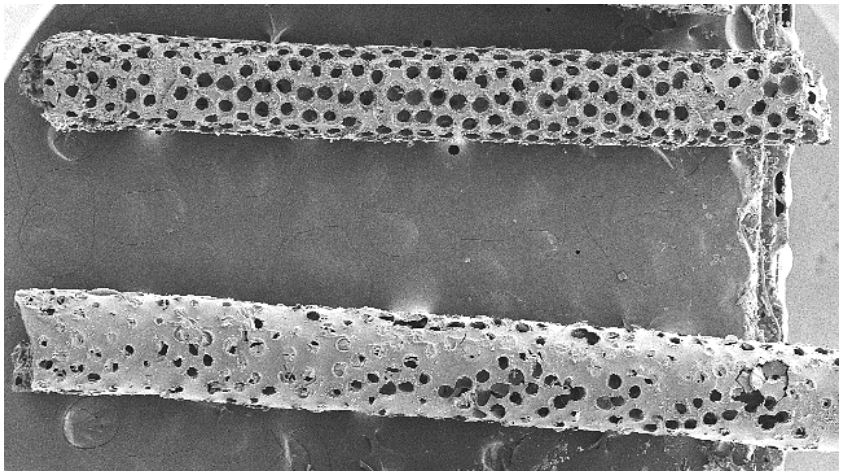

Figure 21 *- Scanning electron micrograph of an unscraped rod using the PMMA coating method (bottom) and a scraped rod (top). The scraping method yields more consistent results.*

5.2 Initial Attempts at Incorporating Microwires for Neural Recordings

Microwires have successfully been incorporated into PTS rods by placing them in the mold prior to beginning the PTS fabrication process. However, it was unknown how the microwires have been affected by the PTS fabrication process. We wanted to answer: (1) does the microwire and Teflon insulation survive the PTS fabrication process; (2) How much does the polymer rod swell and/or how much does the location of the microwire tip change throughout the PTS fabrication process? To test these questions, a 25µm platinum-iridium microwire coated in 4µm of Teflon was placed within the glass mold prior to the beginning of the PTS fabrication process. Afterwards, the samples were observed with scanning electron microscopy. For the most part, the microwires and insulation seemed to remain intact. However, in some places, the microwire insulation seemed crumpled or damaged (**Figure 22**). It is uncertain whether this is due to exposure to organic solvents, rough handling with forceps, or some other reason. We speculate that the organic solvents involved in the PTS fabrication procedure somewhat weaken

the Teflon coating.

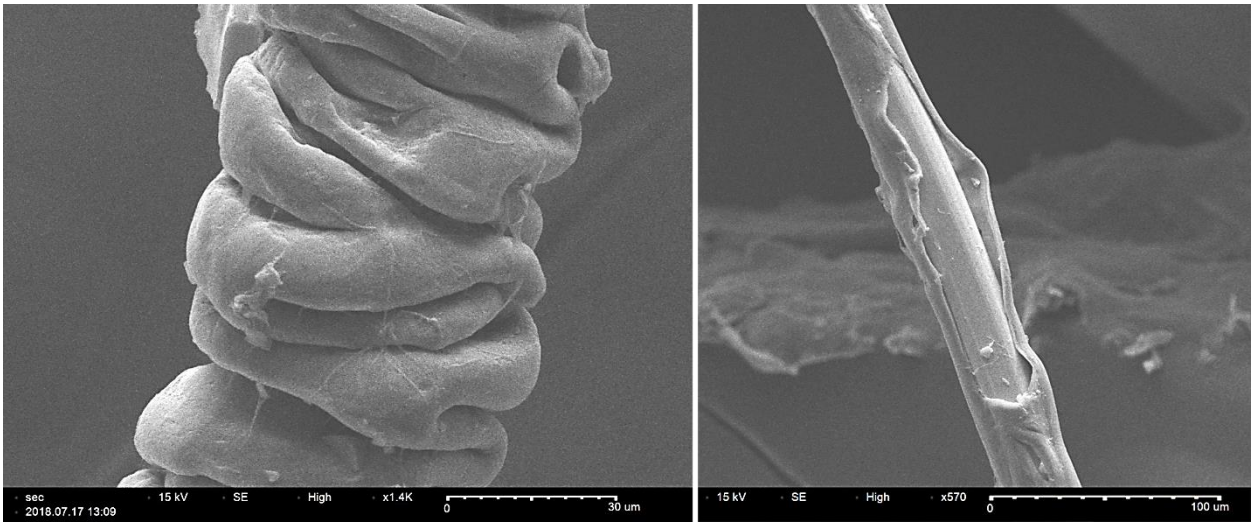

Figure 22 *- Defects in the microwire's Teflon insulation after undergoing the PTS fabrication procedure. Left scale bar is 30 µm s, right scale bar is 100 µm.*

To test if this influences the recording performance of the microwires, they underwent Electrical Impedance Spectroscopy with the help of labmate Lars Crawford. After undergoing the PTS fabrication process, impedance at 1kHz decreased to 20 kΩ or less **(Figure 23)**. This is still within an acceptable range to record neural signals, but if part of the microwire between the recording site and the amplifiers is damaged, then the signal will be compromised.

It is ideal to have the recording surface of the microwire as close as possible to the tip of the PTS rod to take advantage of the prohealing effects of the porous material. However, the polymer swells in different solvents. To test how the positioning of the microwire within the PTS changes, the microwire/PTS tip was cut at different steps in the fabrication process, and the length of wire remaining was measured using scanning electron microscopy. The later in the process the tip was cut, the less exposed microwire was present **(Figure 24)**. If fabricated in this way, it is recommended to cut the tip at the end of the process, after the material has been lyophilized. However, overall it is recommended to try to incorporate a recording device after

PTS fabrication since incorporating before the fabrication process induces so many other factors to optimize.

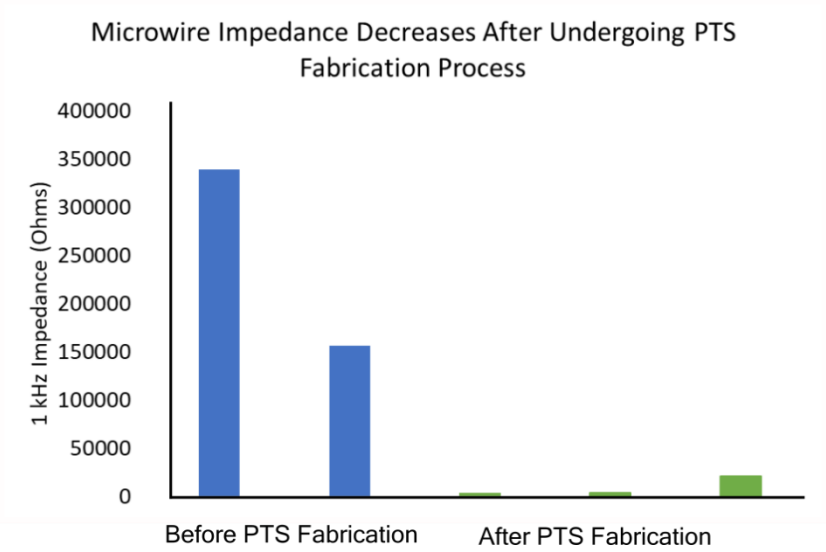

Figure 23 *- Impedance measurement of microwires before (left, blue) and after (right, green) undergoing the PTS fabrication process.*

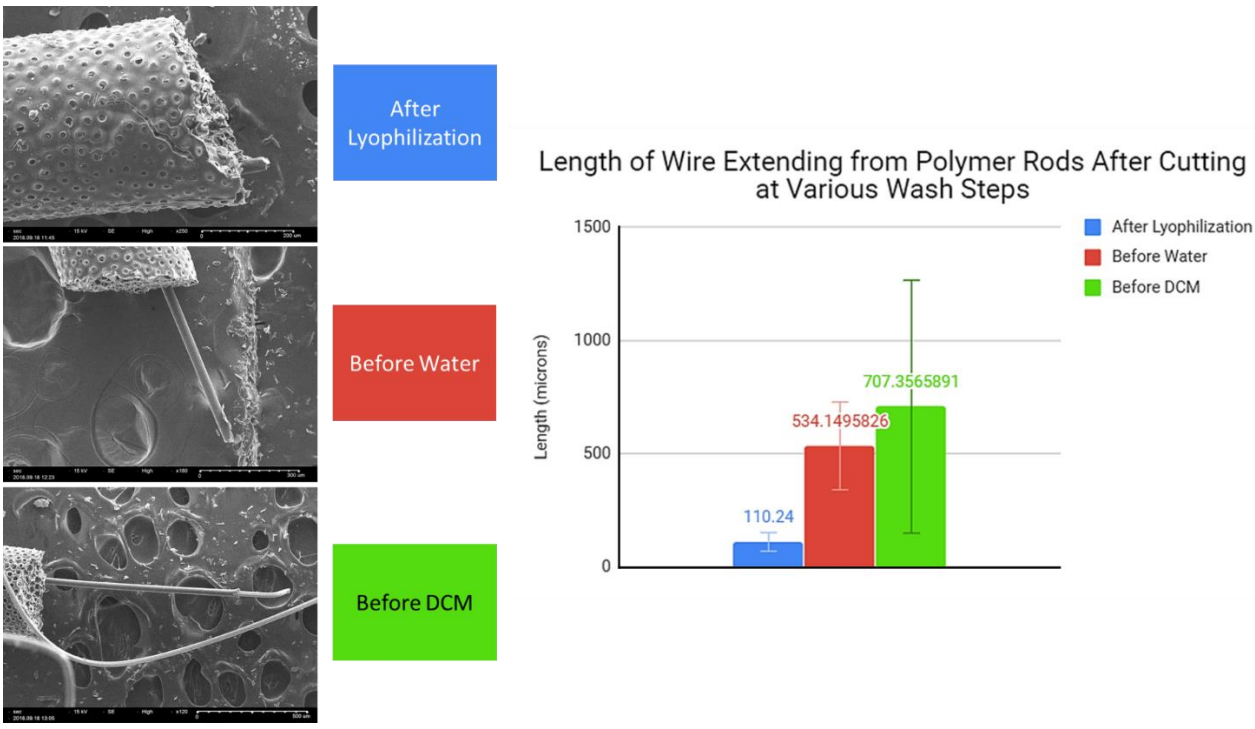

Figure 24 *- Demonstration of polymer swelling and microwire tip location change depending on processing steps. Wires cut after polymer lyophilization result in the least amount of wire extending from the polymer rod at the end of fabrication. (DCM is dichloromethane).*

Chapter 6: Characterization of Inflammation after Spinal Cord Injury

6.1 Introduction

This work has been a collaboration between UW Bioengineering (Ian Dryg, Buddy Ratner, & James Bryers) and the UW Neurological Surgery (Zin Khaing & Christoph Hofstetter) since Summer 2016.

Roughly 282,000 people are living with spinal cord injury, with approximately 17,000 new cases per year (National Spinal Cord Injury Statistical Center, 2013), resulting in $19 billion in direct medical care costs every year (Cao, Chen, & DeVivo, 2011). Although there are many on-going clinical trials for SCI therapies (Kim, Ha, & Kim, 2017), there are still no effective treatments. One strategy for improving SCI outcomes is shifting macrophage phenotypes at the injury from pro-inflammatory phenotypes towards pro-healing phenotypes. Compared to normal wound healing, inflammation does not resolve after spinal cord injury **(Figure 25)**, with levels of pro-inflammatory M1 macrophages remaining high for an extended time (Gensel, Kopper, Zhang, Orr, & Bailey, 2017). Currently attempts at this strategy include utilized pharmaceuticals (Gensel et al., 2017), hyperbaric oxygen (Geng, Cao, Ying, Zhang, & Yu, 2015), stem cell delivery (Nakajima et al., 2012), or other beneficial neuropeptides such as Substance P (Mei H. Jiang et al., 2012; Mei Hua Jiang et al., 2013). Two strategies we have used attempting to modulate immune cell phenotype towards pro-healing are described below.

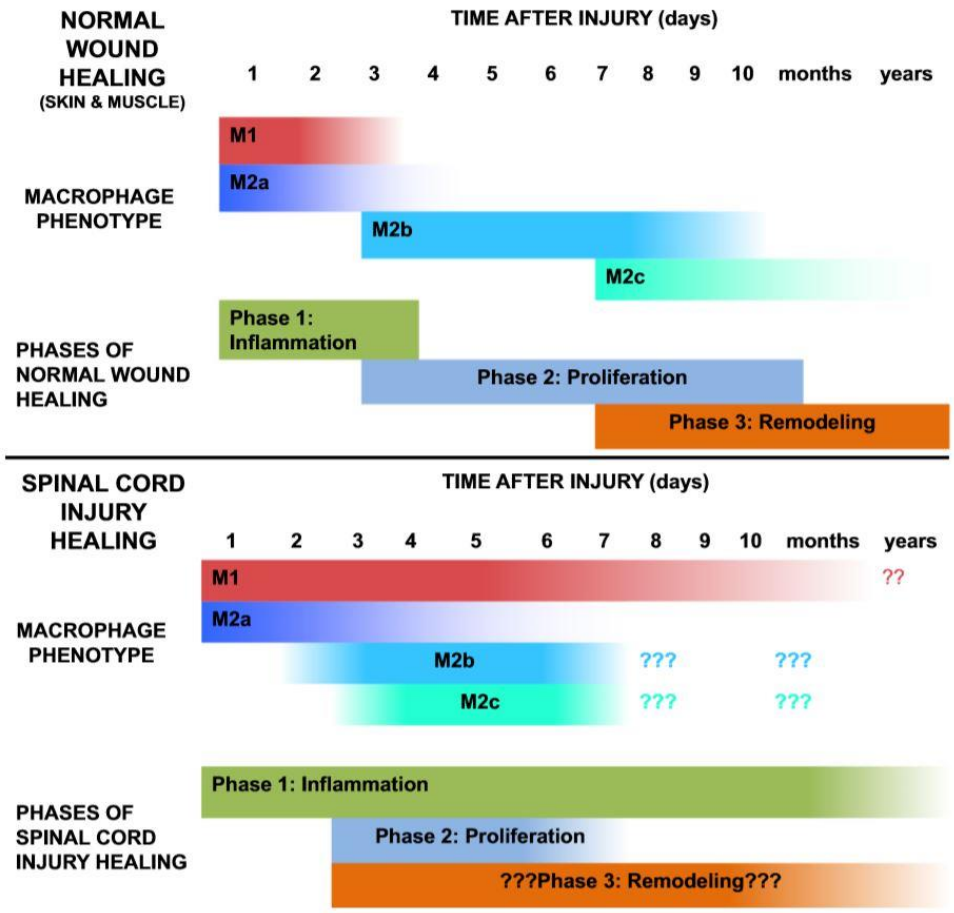

Figure 25 *- Inflammation gives way to pro-healing processes in normal wound healing, whereas inflammation does not resolve after SCI. From (Gensel et al., 2017).*

6.2 Materials and Methods

6.1.1 – Porous Templated Scaffolds for Spinal Cord Regeneration

Because of the immunomodulatory effects of porous hydrogel scaffolds seen in other tissues, we hypothesized that implanting a porous hydrogel scaffold into a spinal cord lesion could influence inflammatory cells towards pro-healing phenotypes, resulting in improved recovery after spinal cord injury. To assess the effects of pore size, we constructed pHEMA scaffolds with 40 μm pores, 100 μm pores, and without pores (nonporous). Each scaffold was washed intensively and stored in sterile PBS prior to implantation. To ensure sterility, samples were taken from each material and cytotoxicity and endotoxicity tests were performed on the material.

Rats were anesthetized with 5% isoflurane and maintained at 2.5% isofluorane. After shaving and sterilizing the surgery site, a longitudinal incision was made over the T8 area. A subperiostal dissection of paraspinal muscles and laminectomy were performed to expose the spinal cord at T8. A contusion injury was performed using a third-generation Ohio State University spinal cord contusion device with a probe tip of 2 mm diameter. The tip was lowered onto the spinal cord to induce a 0.8 to 0.85 mm displacement of the cord resulting in a moderate contusion. After the injury was performed, dura was opened and a pre-cut piece of pHEMA scaffold approximately 1 cm x 3 mm x 3 mm was placed into the lesion. The dura, muscle, and skin were sutured in layers to close the wound. All survival animals were treated with lactated Ringer's solution (subcutaneous; 5–10 mL), and analgesics (buprenorphine; 0.03mg/kg every 12h for 48h after surgery. Animals were allowed to recover in warmed cages and manual bladder expression was performed twice daily until normal void response recovered (up to 7days post-injury). Animals were euthanized by cardiac perfusion with PBS and 4% paraformaldehyde after 14 days of recovery for histological assessment. After perfusion, spinal cords were dissected and transitioned into 30% sucrose solution before freezing at -80 C and mounted within Optimal Cutting Temperature solution. Frozen cords were cross-sectionally sliced at a thickness of 10 μm and mounted onto slides for staining. Slices were stained with DAPI to label cell nuclei, GFAP to label astrocytes, and CD68 to label macrophages and activated microglia.

Initial histology revealed a few observations **(Figure 26)**. First, it was clear that cells were infiltrating into the porous structure, and that CD68 positive cells were lining the pores of the implant, similar to what has been seen in other experiments. Second, in some cases, the implanted scaffolds had either drifted away from contacting the injury site, or other tissue had grown in between the injury and the implant – thus, any potential local beneficial effects of the scaffold would not be present because of the distance between the scaffold and the injury.

Third, in some cases where the scaffold was in contact with the spinal cord, the cord was giving way to the scaffold. That is, due to the mechanical mismatch between the stiffer polymer (~100 kPa) and the softer spinal cord tissue (~8 kPa), the polymer implant was deforming the spinal cord tissue. Because of this, for future implant experiments, we plan to use a softer hydrogel material than the standard pHEMA, which is outlined later in section 5.2.

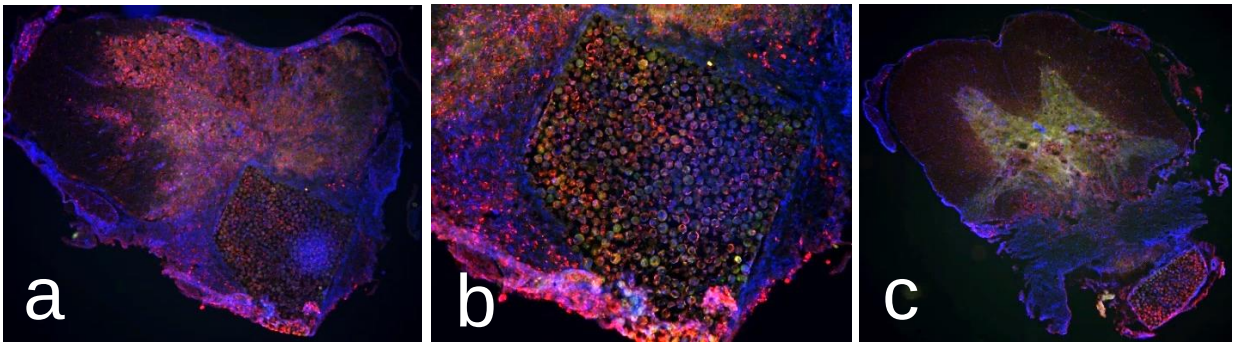

Figure 26 *- Porous SCI Implant Histology. (a) Cord giving way to stiffer polymer implant, and (b) zoomed in. (c) Tissue growth between the injury and the implant. Red is CD68 (Macrophages & Microglia), green is GFAP (Astrocytes), blue is DAPI (Nuclei).*

Right before sacrificing the implanted animals, they were assessed for functional recovery using the BBB test **(Figure 27)**. (BASSO, BEATTIE, & BRESNAHAN, 1995). While the nonporous implant group showed reduced recovery, animals that received porous implants scored no differently than animals that received an injury but no implant, suggesting that porous implants had no detrimental effects on recovery in their current state. If these porous implants could be improved in some way, by incorporating pharmaceutical release, stem cell seeding, or reduced mechanical modulus, for example, then there may be therapeutic effects on recovery.

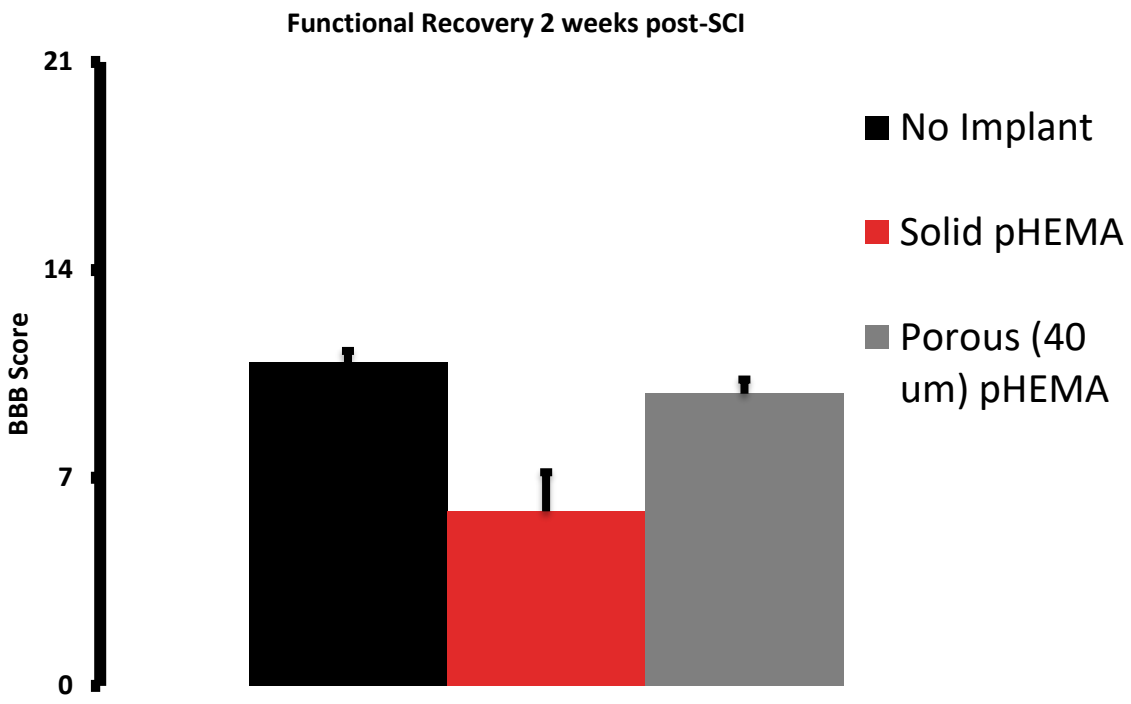

Figure 27 *- Functional recovery of rats with SCI , comparing no implant control with nonporous (solid) pHEMA implants and 40 µm porous pHEMA implants. There were no detrimental effects on BBB score between no implant control and 40 µm porous implants.*

6.1.2 – Using Flow Cytometry to Assess Effects of Duratomy on Neuroinflammation After SCI

Before moving on to future polymer implant experiments, we wanted to characterize inflammation after spinal cord injury and investigate the effects of another surgical procedure, duratomy. For injuries to the brain and brainstem, there are strict guidelines for management of intracranial pressure (Bratton et al., 2007) intended to maintain brain tissue perfusion and oxygenation, minimizing secondary injury. This treatment strategy has significantly reduced mortality and morbidity associated with traumatic brain injury (L. F. Marshall, Smith, & Shapiro, 1979; Miller et al., 1981). However, no such treatment strategy has been adopted to monitor intraspinal pressure (ISP) for spinal cord injury. Recent studies have shown that ISP increases at the injury site of patients with traumatic SCI (Werndle et al., 2014), and that surgical decompression of the dural spinal lining, a technique called a duratomy, decreased ISP (Phang et al., 2015). It is theorized that this decompression allows for increased perfusion into the

pressurized tissue at the injury, reducing secondary tissue injury. A recent paper published by the Hofstetter Lab has verified these results in a rat model, showing that performing duratomy effectively reduces ISP in rats (Khaing et al., 2017) and more recent, unpublished data shows duratomy increases rat recovery for moderately injured animals. Because inflammatory mediating cells are so important for spinal cord injury healing, we wanted to see if macrophage phenotypes are modulated by duratomy.

The aforementioned study showed an increase in ISP at the injury site, but also rostral to the injury **(Figure 28)** (Khaing et al., 2017). Because of this spatially distributed increase in ISP, we wanted to investigate macrophage phenotype at different locations around the injury site. To achieve this, we performed T8-level contusion injuries on 46 animals in several cohorts, with 20 receiving an injury only, 16 receiving an injury and duratomy, and 10 uninjured controls. Animals were euthanized and perfused with ice-cold PBS at 3, 7, 14, and 21 days post-injury with approximately 4 or more animals in each group per timepoint. Four sections of spinal cord from each animal were dissected out for flow cytometry: caudal to the injury, at the injury site, rostral to the injury, and far from the injury (cervical cord). Each section of cord removed spanned two spinal cord segments – so the tissue sample from the injury site spanned from T7-T9, with the injury site in the center of the tissue sample. Livers were harvested for CD68 positive controls, and a site next to the cervical spinal cord was harvested for use as an unstained cord sample (negative control).

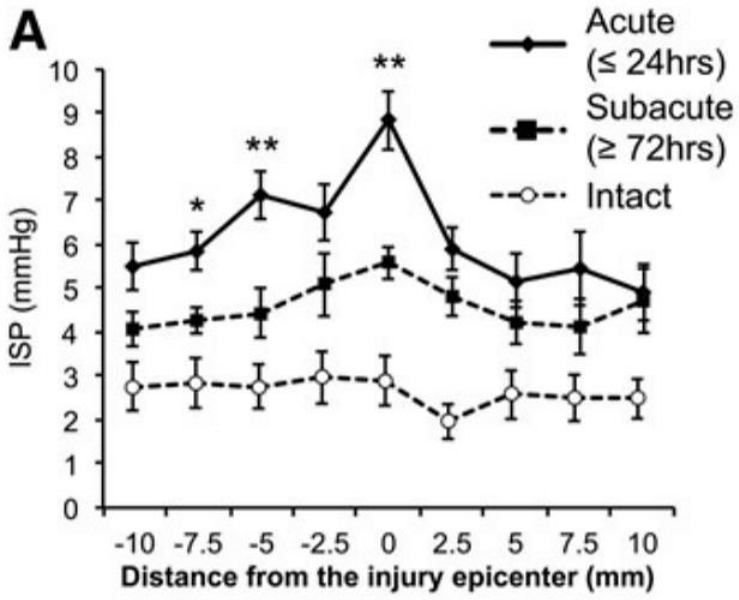

Figure 28 *- Intraspinal pressure increases at the injury site and rostral to the injury site after spinal cord injury. From (Khaing et al., 2017).*

Tissue samples were processed for flow cytometry as described elsewhere (Chen et al., 2015). Briefly, samples were minced with fine surgical scissors and triturated in digestion buffer (Liberase and DNAse) and incubated in digestion buffer for 20 minutes. Samples were ground through a 40 µm cell strainer, incubated for 10 more minutes, and then treated with cell culture medium with 10% FBS to stop enzymatic digestion. Red blood cells were removed with 5 minutes incubation in red blood cell lysis buffer, and cellular debris and other cell types such as neurons were removed using an Optiprep density gradient, discarding the supernatant, and resuspending the pellet. Cells were immunolabled with CD86-PE for M1 (pro-inflammatory) cells, CD163-AF647 for M2 (pro-healing) cells, and fixed, permeabilized, and labeled with CD68-FITC to label all macrophages and activated microglia (**Table 2**). Flow cytometry was performed using a BD LSR II flow cytometer, and cells were gated for size, CD68-FITC fluorescence, and CD86-PE and CD163-AF647 fluorescence to quantify cell phenotype **(Figure 29)**.

Table 2 *- Antibodies used for flow cytometry*

Antibody	Target	Conjugated Fluor	Host	Company	Catalog #
CD68	Macrophages	FITC	mouse	BioRad	MCA341F
CD86	M1 Macrophages	PE	mouse	eBioscience	12-0860-83
CD163	M2 Macrophages	AF647	mouse	BioRad	MCA342A647
Fc Blocker	Fc Receptor on Macrophages	none	mouse	BD	550271

My first compilation of the data is shown in **Figure 30**. Initial results did not reveal any significant differences between Lesion Only and Lesion plus Duratomy groups. Additionally, few effects were seen rostral to the injury, contrary to the ISP data observed. Data seem to show that number of macrophages spikes early after injury, but declines after a few weeks, which follows other published data(Chen et al., 2015). In general, I believe the CD68 data and trust it as a good macrophage marker. However, there appears to be no effect of duratomy on the proportion of M1 to M2 macrophages, indicating that a release of pressure is not modulating the inflammatory profile of cells in the injury – at least using these two surface markers. One worrysome feature of this data is that the unstained controls are rather high in some groups – indicating a high level of autofluorescence or poor gating. Additionally, the percentage of M1 and M2 cells is very low in general – so finding the true signal above the noise may be difficult. There are many other markers that could be used, or genetic profiling by qPCR could be used to gauge gene expression of these cells instead. Whatever the case, more analysis is needed to determine the effects of duratomy on the inflammatory environment in SCI.

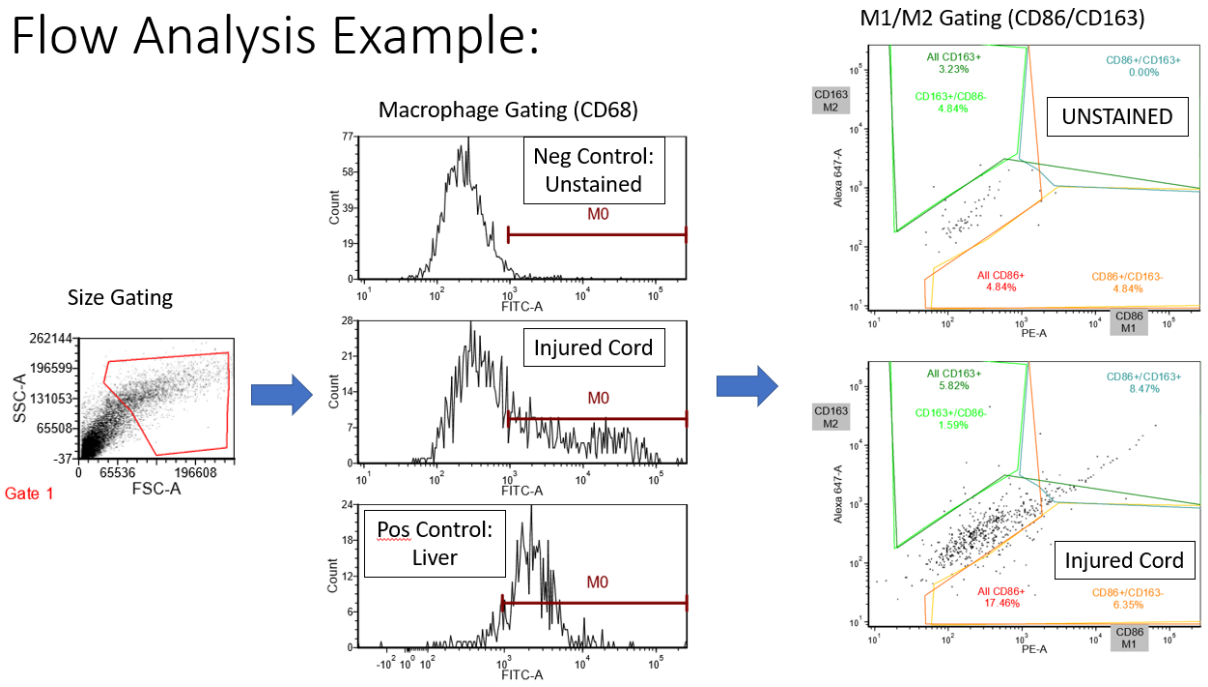

Figure 29 *- Example of gatings used for flow analysis. First, cells were gated for size to exclude cellular debris. Second, cells were gated using the pan-macrophage marker, CD68. Unstained negative controls showed low fluorescence, injured cord samples had some cells expressing higher fluorescence (demonstrating the increased number of macrophages and activated microglia), and liver positive control cells showed high fluorescence. Finally, cells were gated using the M1 and M2 markers, CD86 and CD163. Gates were determined using unstained negative controls.*

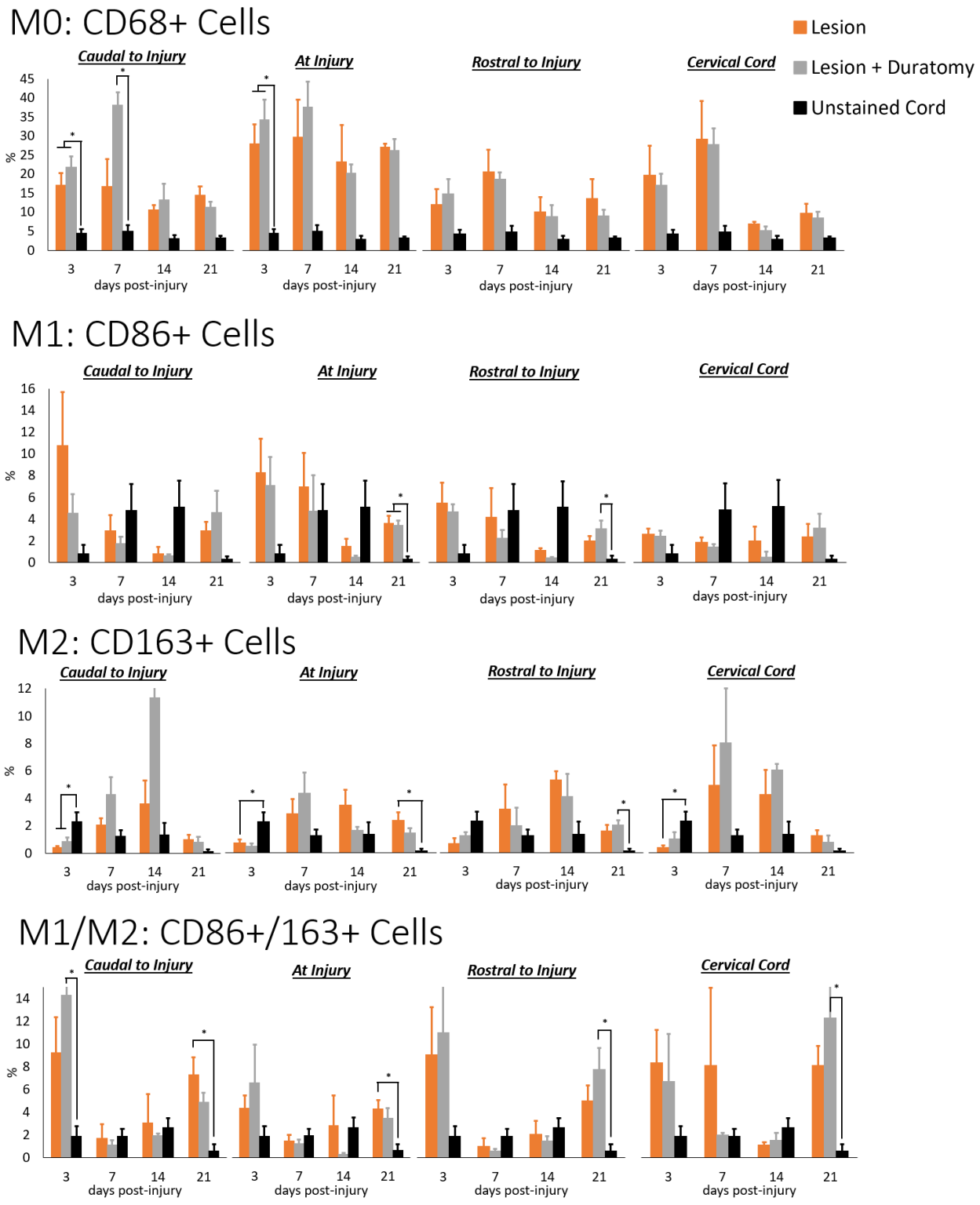

Figure 30 *- Flow cytometry results. M0 plots show percentage of size-gated cells positive for CD68. M1, M2, and M1/M2 plots show percentage of M0-gated cells positive for their respective markers. Error bars show standard error of the mean, and stars denote a significant difference determined by one-way ANOVA and post-hoc Tukey-Kramer tests. Color legend is shown on the right.*

Chapter 7: CNS Tissue Response to Porous Materials

7.1 Introduction

This work has been a collaboration between UW Bioengineering (Ian Dryg, Buddy Ratner, & James Bryers) and the UW Physiology & Biophysics (Steve Perlmutter) since Summer 2016.

The significance and background on glial scarring around implanted neural interfaces have been discussed in earlier background sections. To address these issues, I have been developing porous pHEMA rods to implant into cortex to study cellular and tissue responses. The overall hypothesis is that PTS will improve reactive brain cell responses, creating a healing environment around the implant rather than an inflammatory environment. Outcomes of these experiments will characterize tissue responses to porous hydrogel neural implants and inform future studies of glial cell activation and behavior. Additionally, I aim to create a novel porous neural interface design capable of extracellular neural recording. This would provide a new tool for neuroscience researchers and clinicians, potentially maintaining stable neural recordings for longer periods of time.

7.2 Materials and Methods

As an initial test of our hypothesis that porous polymers can decrease glial scarring around cortical implants, we performed an implant study with the help of the Perlmutter Lab. In each of six rats, four pHEMA rods were implanted into cortex, one of each type: nonporous (NP), 40μm molded (40M), 40μm punched (40P), and 100μm punched (100P). After fabrication of the polymer rods, they were handled in sterile conditions, lyophilized, and dry-autoclaved prior to implantation. These polymer rods had to be implanted dry to ensure that they were stiff enough to penetrate brain tissue. After implantation the rods hydrated within several seconds, becoming soft. After anesthetizing with 5% isoflurane, anesthesia was maintained with 2.5% isofluorane. A midline incision was made and tissue was cleared from the skull's surface. Bone screws were placed around the perimeter of the opening, and two craniotomies were opened –

one over each hemisphere, from ~2 mm lateral to midline to ~5 mm lateral to midline, extending ~8 mm long between Lambda and Bregma **(Figure 31)**. After craniotomies were performed, the dura was opened using fine forceps, and polymer rods were implanted. Craniotomies were covered with gelfoam, a PMMA headcap was built covering the exposed skull, stabilized by the bone screws. Animals were allowed to recover for either 1 week (n=3) or 4 weeks (n=3). These time points were chosen because macrophage responses peak around 1 week after injury, and the glial scar stabilizes by 4 weeks post injury. Animals were injected with Beuthanasia-D, and after they passed toe-pinch tests, cardiac perfusions were performed with PBS (to wash out blood), and 4% Paraformaldehyde (PFA, to fix the tissues). Rat heads were removed and post-fixed in 4% PFA overnight and then washed in PBS. Carefully, brains were removed while ensuring that implanted polymers remained *in situ*. Brains were sectioned and sliced using a vibratome into 50-µm thick slices and stored in 48-well plates in Hank's Buffered HEPES Saline (HBHS) at 4 degrees C for storage until staining. Immunohistochemistry images are shown in **Figure 32** and information is shown below in **Table 3**.

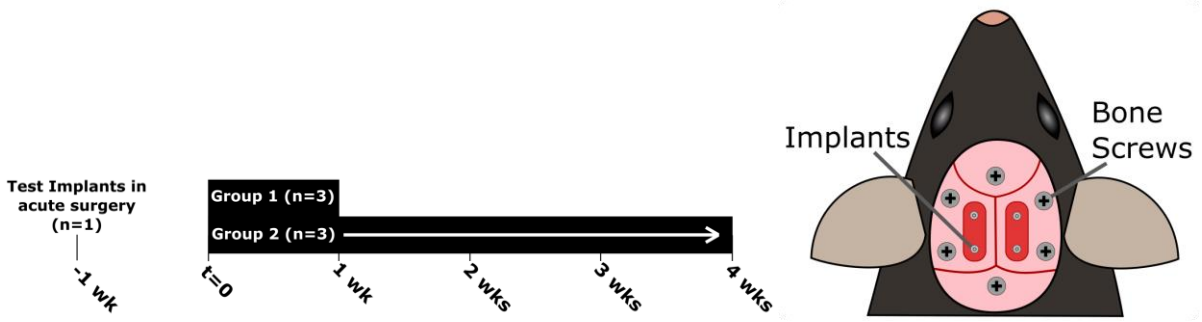

Figure 31 *- Experimental design for initial cortical implant experiment , with animal timeline (left) and and surgical layout (right).*

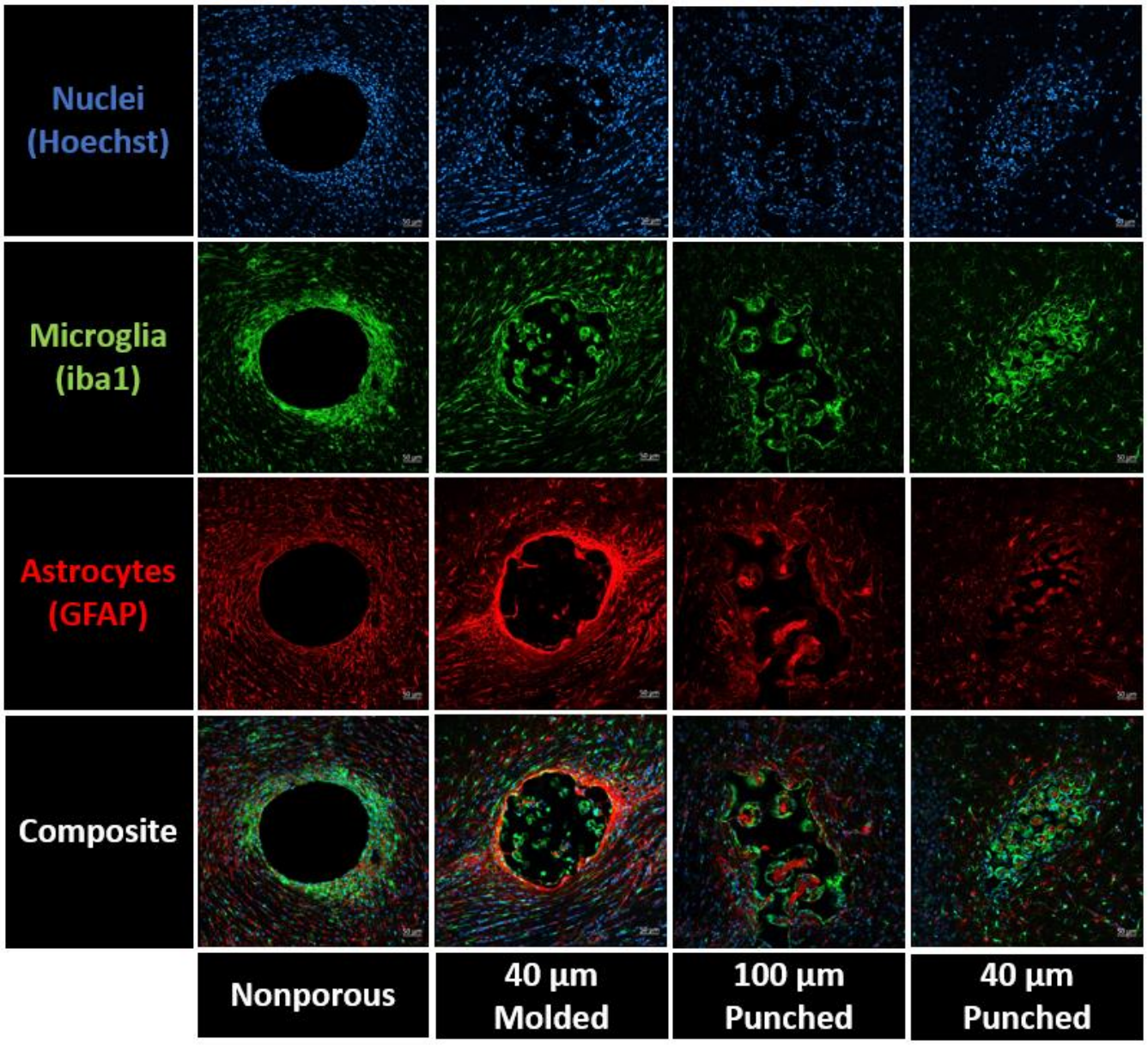

Figure 32 *- Representative 20X confocal images from each group. Hoechst (blue, first row) was used to label cell nuclei, iba1 (green, second row) for microglia and activated macrophages, GFAP (red, third row) for reactive astrocytes, and composite images (fourth row). Implants are each ~300 µm in diameter, scale bars in each image are 50 µm. Note the decreased interconnected of the porous structure within the molded implants.*

Table 3 *- Antibodies and immunohistochemistry information used in pHEMA implant experiments.*

Antibody/stain	Target	Supplier	Catalog #	Dilution
Hoechst 33342	Cell Nuclei	ThermoFisher	H3570	1:1000
Iba1	Microglia	Wako	016-20001	1:250
GFAP	Astrocytes	ThermoFisher	13-0300	1:800
RECA1	Endothelial Cells	Abcam	ab9774	1:200
MAP2	Neurons	Millipore	ab5622	1:1000

Fluorescence data was quantified in FIJI (ImageJ) using a plugin called Radial Profile Angle which collects fluorescence intensity starting at the center of a defined circle moving outwards, averaging fluorescence intensity for each radial distance from the center of the circle. Defining the center of the circle as the center of each polymer implant, we can collect fluorescence profiles vs. distance from the center of the implant, including fluorescence originating from cells that have migrated into the pores of the porous polymer implants. Fluorescence profiles from each animal were averaged together, normalized to control tissue which was taken far from any implants, and plotted **(Figures 33-36)**.

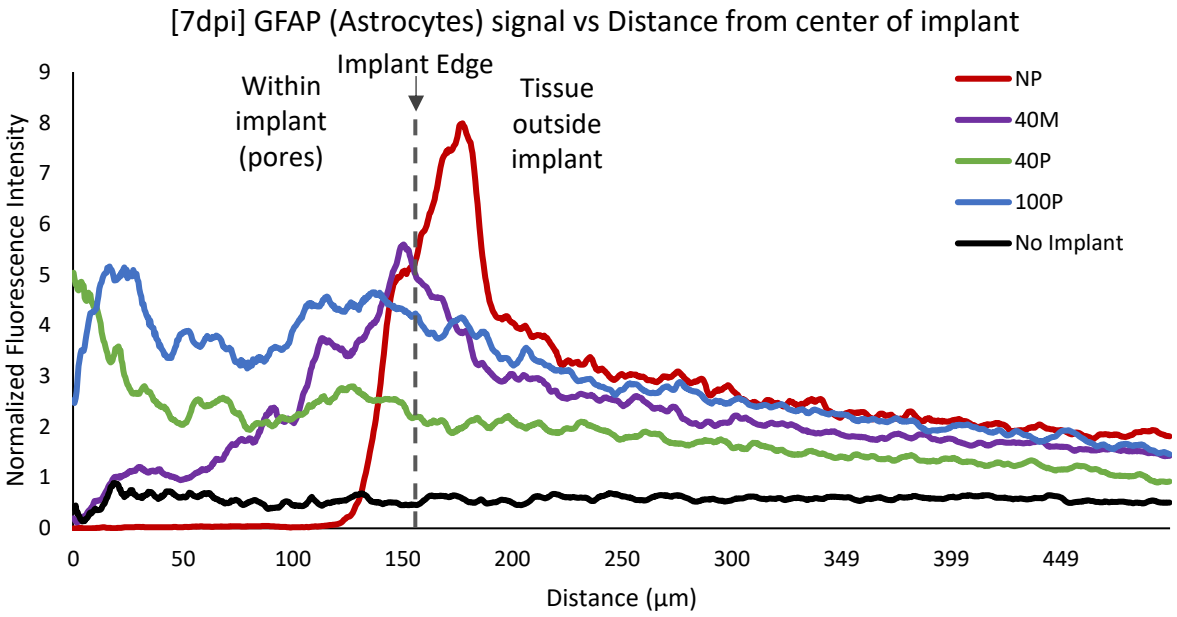

Figure 33 *- Normalized GFAP (astrocytes) fluorescence vs. distance from the center of the implant, 7 days post implant. Implants with 40 µm pores show decreased astrocyte encapsulation.*

At 7 days post-implant, porous implants show reduced astrocyte and microglial encapsulation. Needle-punched implants with 40 µm pores showed the lowest levels of fluorescence overall, while nonporous implants showed a clear spike of GFAP and iba1 fluorescence at the implant edge, indicating dense glial scar formation. However, by 21 days post-implant, there are no differences between implant groups. This study provides evidence that porous implants, especially punched porous implants with 40 µm pores, may slow down the glial encapsulation process.

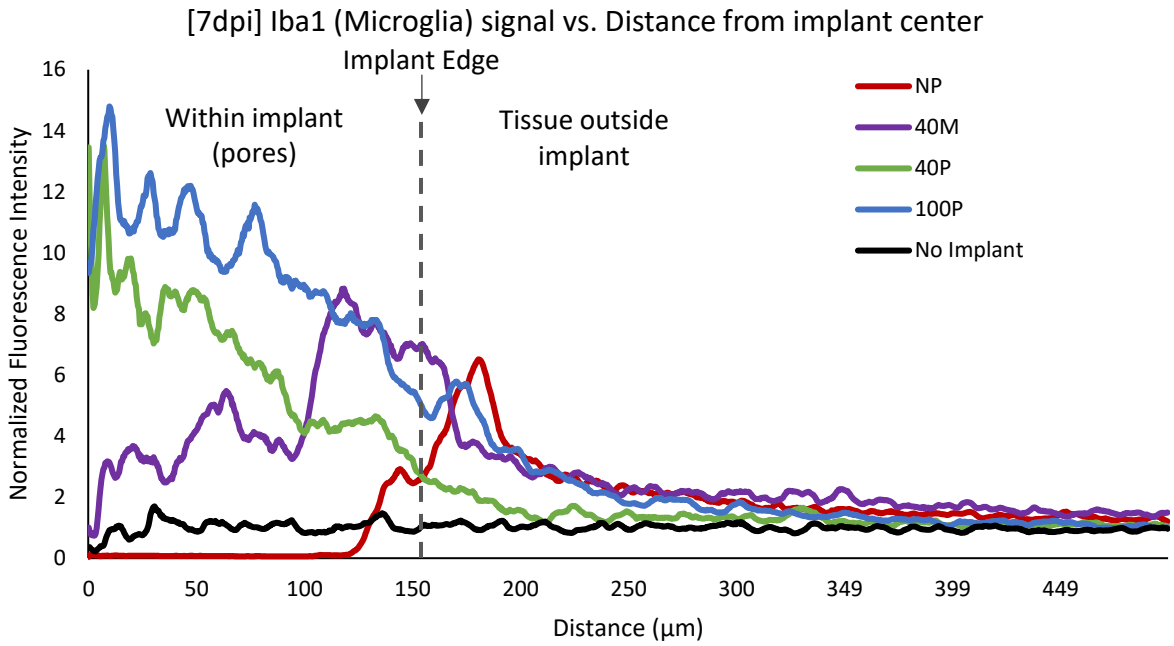

Figure 34 *- Normalized iba1 (microglia) fluorescence vs. distance from the center of the implant, 7 days post implant. Implants with 40 µm pores show decreased microglial encapsulation.*

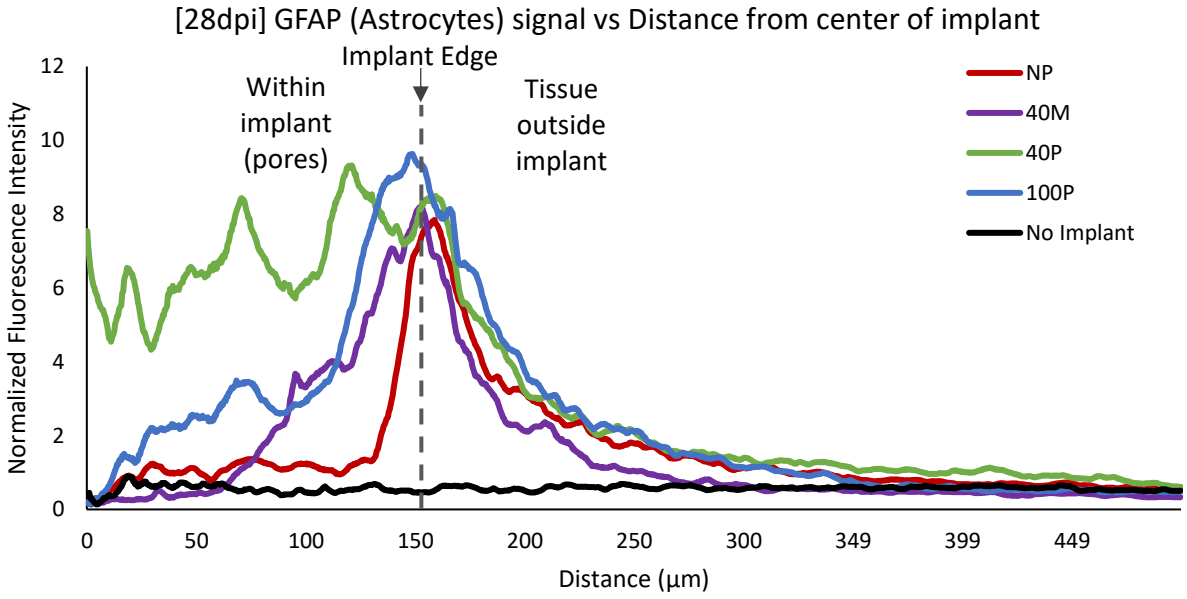

Figure 35 *- Normalized GFAP (astrocytes) fluorescence vs. distance from the center of the implant, 21 days post implant. All implants show similar levels of astrocyte encapsulation.*

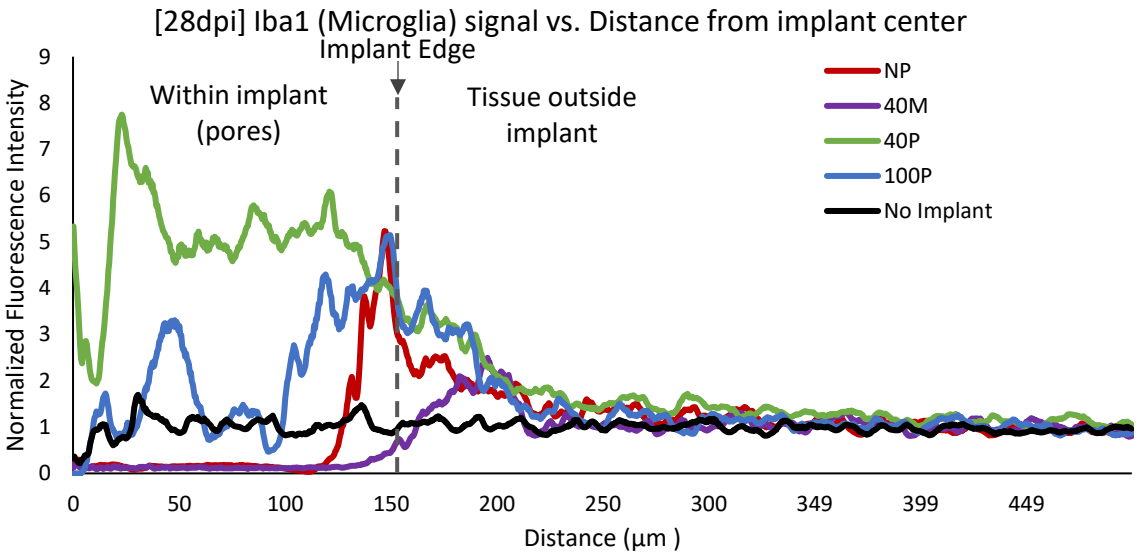

Figure 36 *- Normalized iba1 (microglia) fluorescence vs. distance from the center of the implant, 21 days post implant. All implants show similar levels of microglial encapsulation.*

In addition to staining with glial cell markers, other markers were examined **(Table 3)**, including RECA1 (endothelial cells/blood vessels), MAP2 (neurons), CD68 (macrophages and activated microglia), and MMR (pro-healing cells/M2 macrophages). The presence of porous implants does not seem to affect neurons negatively **(Figures 37-40)**. Neuronal tracts labeled by MAP2 extend inside the porous material, suggesting that recording with an incorporated neural interface could be possible. RECA1-positive cells label vascular endothelium, such as the blood vessel seen on the left. Within pores, cells are highly expressing RECA1, suggesting the formation of blood vessels within the material.

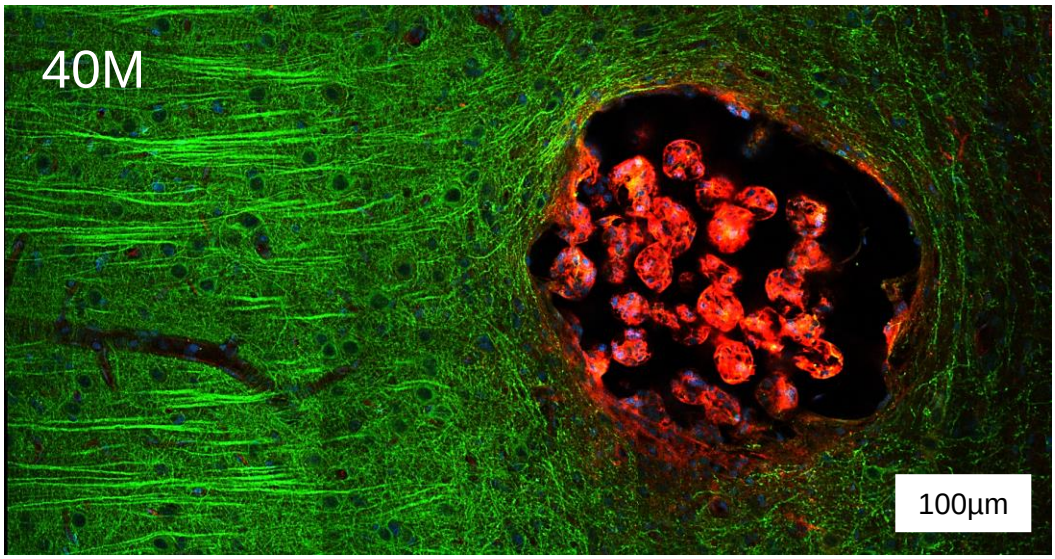

Figure 37 *- Molded 40 µm porous rod within brain tissue, labeled with MAP2 (Neurons, green), RECA1 (vascular endothelium, red), and Hoechst (nuclei, blue). In this sample, RECA1 fluorescence is much more intense within the pores than around actual blood vessels.*

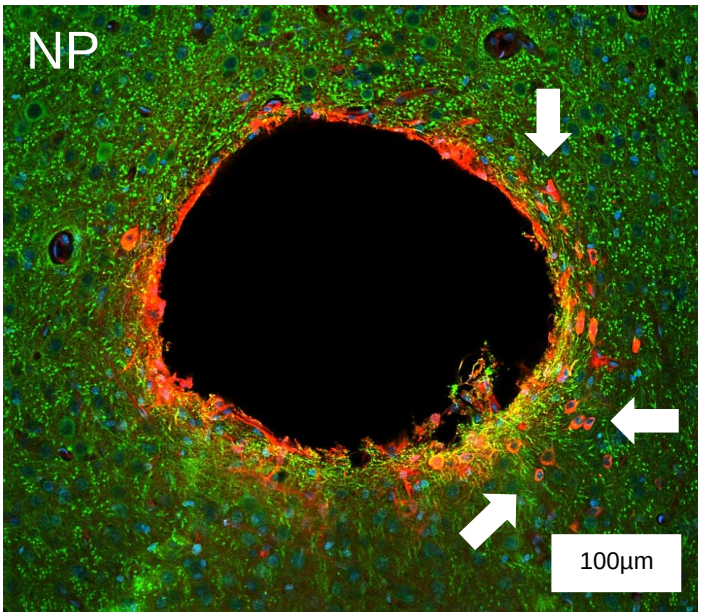

Figure 38 *- Nonporous pHEMA rod within brain tissue, labeled with MAP2 (Neurons, green), RECA1 (vascular endothelium, red), and Hoechst (nuclei, blue). Many cells engulfing the implant are labeled positive for RECA1. Interestingly, there are even cells not in direct contact with the implant labeled positive for RECA1 (see arrows), suggesting either other cell types are changing phenotypes to express RECA1, or new endothelial cells are being created around the implant.*

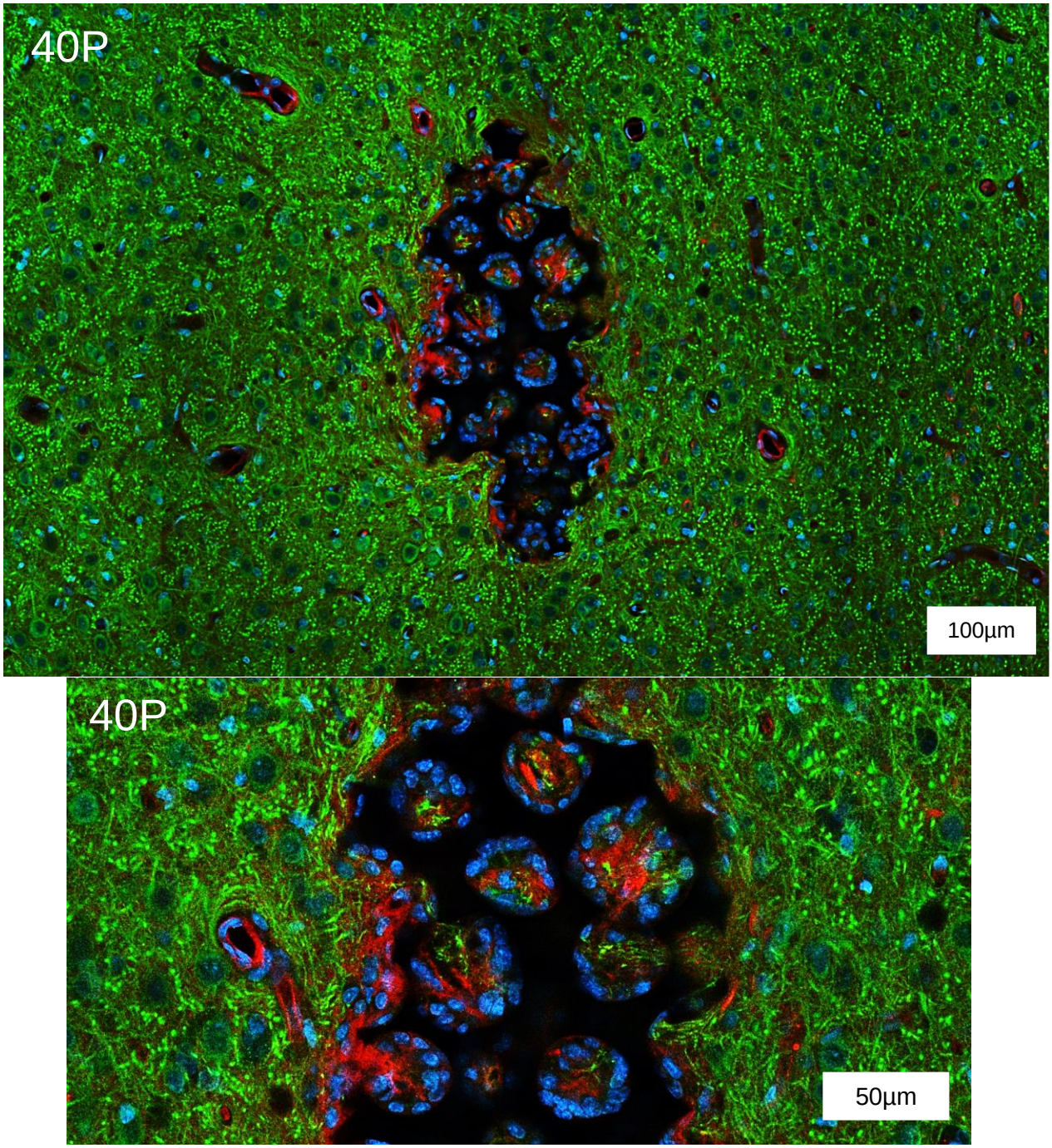

Figure 39 *- Punched 40 µm porous rod within brain tissue, labeled with MAP2 (Neurons, green), RECA1 (vascular endothelium, red), and Hoechst (nuclei, blue). The bottom image is zoomed in on the polymer-tissue interface of the top image. In these images, most neuronal tracts run out of the page rather than across the image, hence the dot-like appearance (contrarty fo Figure 33, where tracts run across the image). For this punched rod, there is positive MAP2 and RECA1 labeling within the pores, suggesting that both blood vessels and neurons have grown into the porous structure. RECA1 staining is less intense in this sample than in Figure 33.*

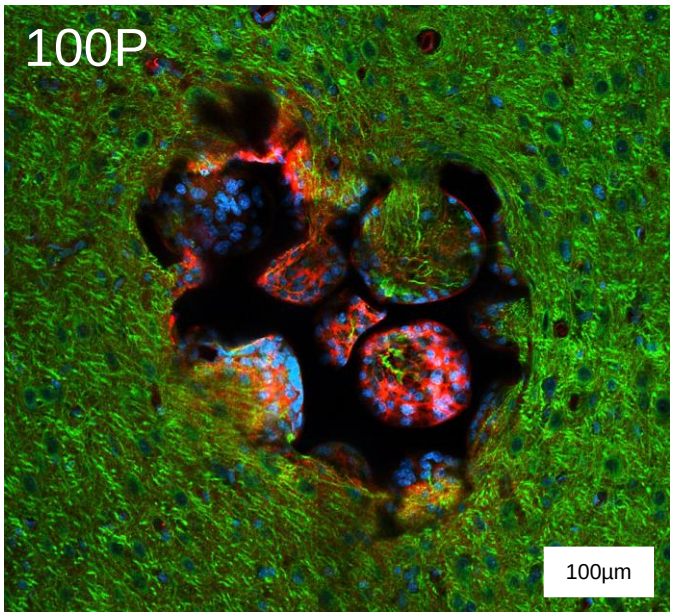

Figure 40 *- Punched 100 µm porous rod within brain tissue, labeled with MAP2 (Neurons, green), RECA1 (vascular endothelium, red), and Hoechst (nuclei, blue). Even in 100 µm pores, there are cells positively labeled with RECA1 (lining the pore walls) and MAP2, demonstrating vessel and neuron growth into the pores.*

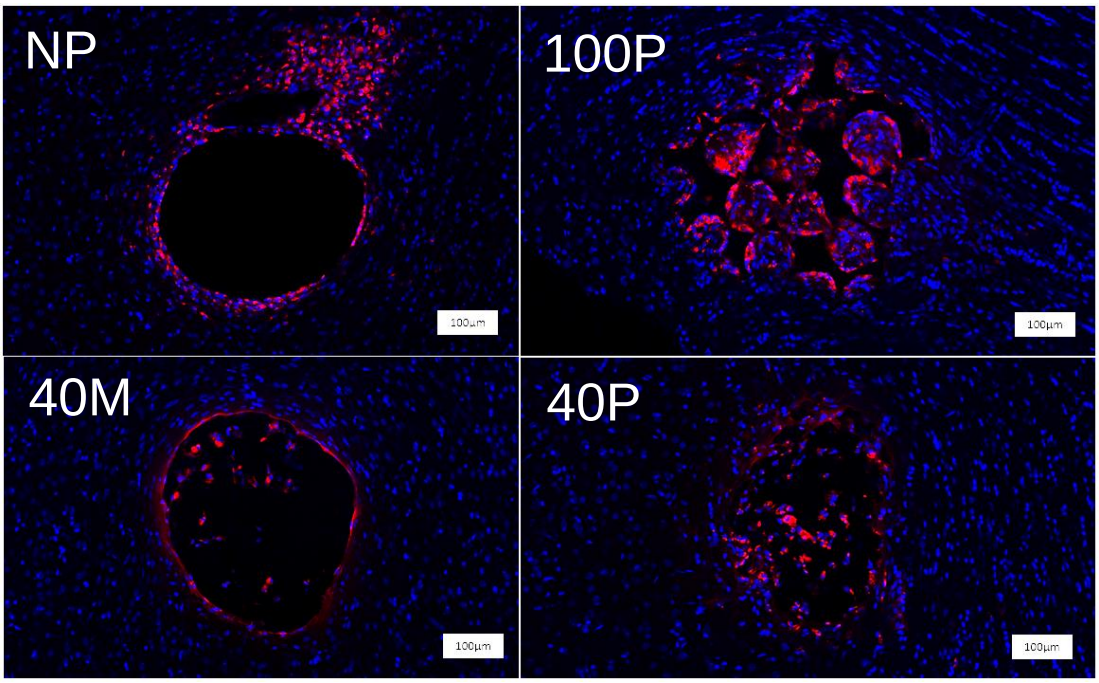

Figure 41 *- Slices labeled with CD68 (macrophages, activated microglia, red) and Hoechst (cell nuclei, blue). Macrophages line the surface of the nonporous implant (top left), and migrate into pores of porous implants, covering the surface of the pores. This section of the molded 40 µm implant (bottom left) appears to have poor porous structure as indicated by the positive labeling of CD68 around the seemingly nonporous surface of the implant.*

This initial histological examination shows promising results – neurons, endothelial cells, and macrophages appear to migrate into pores of porous implants. Tissue generally integrates better with implants that have a better porous structure (rods that were punched from bulk scaffold rather than molded rods). These experiments seem to demonstrate that the quality of the interconnected porous structure affects cellular and tissue responses in the brain. More experiments need to be performed to determine the effects of pore size on neuron, endothelial cell, and macrophage activity within pores, including more quantification of histology.

This research resulted in the following conference presentations:

Dryg, ID, Crawford LM, Perlmutter SI, Bryers, JD, Ratner BD (April 2019). Porous Hydrogels for Neural Implants: Effect of Pore Size on Glial Encapsulation. Society for Biomaterials Conference, 2019, Seattle, WA.
Dryg, ID, Crawford LM, Perlmutter SI, Ratner BD (June 2018). Directing Brain Tissue Integration for Long-Term Electrophysiology with Conductive Microporous Hydrogel Electrodes. NeuroFutures Conference, 2018, Seattle, WA.
Dryg, ID, Crawford LM, Perlmutter SI, Ratner BD (March 2018). Directing Brain Tissue Integration for Long-Term Electrophysiology with Conductive Microporous Hydrogel Electrodes. Gordon Conference for Neuroelectronic Interfaces, 2018, Galveston, TX.

Chapter 8: Effect of Implant Stiffness on CNS Tissue Response to Porous Materials

8.1 Introduction

Currently available implanted neural interface devices are made of stiff materials such as micro-machined silicon (Utah or Michigan Arrays) or metal microwires **(Figure 42)**. A growing body of evidence shows this stiffness mismatch between implant materials (~200 GPa) and brain tissue (~6 kPa) may result in increased reactive tissue responses to neuroprosthetic devices; and that reducing stiffness of neural interface materials can reduce tissue responses (Harris et al., 2011; Nguyen et al., 2014). However, studies that have tested softer materials have still featured materials with stiffnesses orders of magnitude greater than the stiffness of the brain. If we can match the stiffness of the implant to the stiffness of the brain, negative effects from the mechanical mismatch should be eliminated and glial scarring will be reduced. In this chapter, we tested the effects of stiffness using hydrogels of three different stiffnesses, encompassing the stiffness of the brain.

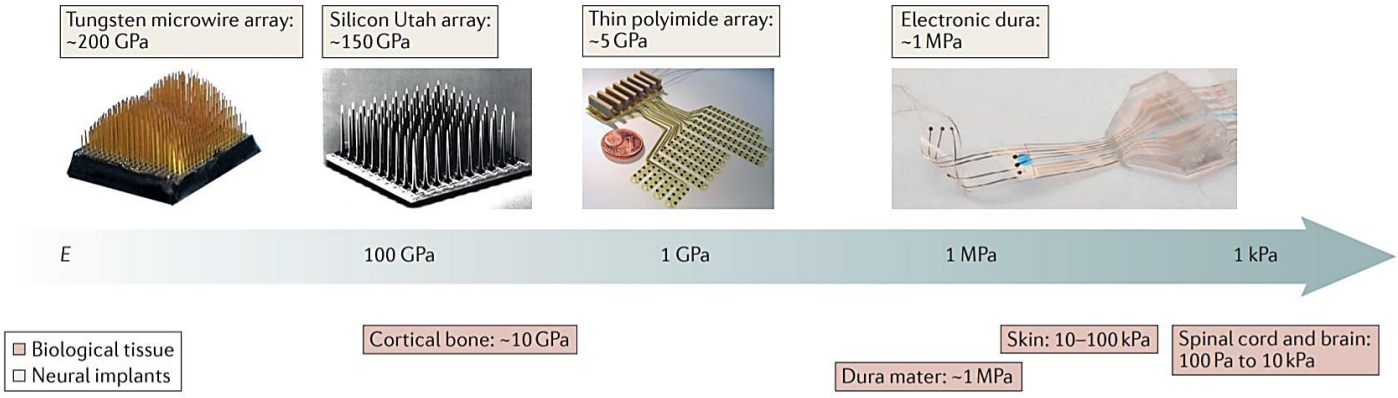

Figure 42 *- The wide spectrum of stiffnesses in available neural interface materials compared to biological tissue. From (Lacour, Courtine, & Guck, 2016).*

Recently, two other members of the Ratner Lab, Le Zhen and Becky Darrow, demonstrated that the stiffness of pHEMA can be tuned by varying the water content in the monomer solution. However, at higher water percentages, the resulting hydrogel microstructure began to accumulate numerous defects due to the hydrophobicity of HEMA, which made it unsuitable for making a Porous Templated Scaffold. To overcome this, they made a co-polymer

using HEMA and Glycerol Monomethacrylate (GMA), since the GMA has an additional OH group that adds hydrophilicity, helping the microstructure hold up at higher water percentages **(Figure 43)**. Using this co-polymer, they were able to tune the stiffness by varying water content, and the microstructure looked satisfactory **(Figure 44)**.

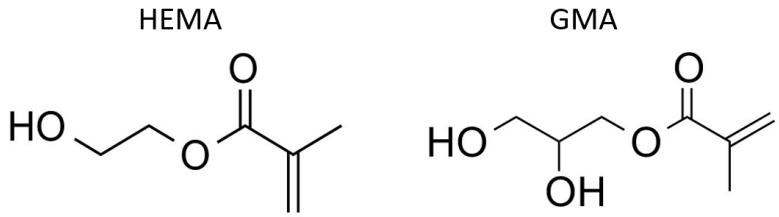

Figure 43 *- HEMA and GMA monomers. The extra hydroxyl group on the GMA makes it more hydrophilic.*

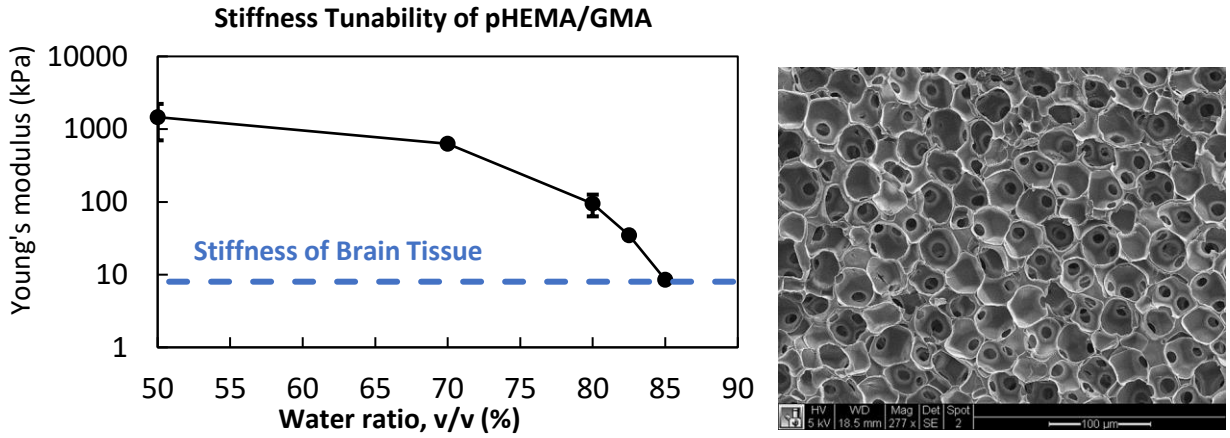

Figure 44 *- Stiffness tunability of pHEMA/GMA (compressive modulus, left). At 85% water, the material matches the stiffness of brain, and the microstructure of the material is satisfactory (right). Credit: Le Zhen & Becky Darrow.*

With this preliminary data, this co-polymer (50% HEMA, 50% GMA) was used for the stiffness study described in this chapter. It was hypothesized that there would be a correlation between polymer stiffness and extent of glial scarring, and implants with 40 µm pores would show the least glial scarring within each stiffness group. Similarly, it was expected that softer porous implants would have higher amounts of neurons both near and within the implants. Finally, it was hypothesized that softer implants will modulate nearby macrophages to express

more pro-healing markers (M2) and less pro-inflammatory markers (M1) compared to stiffer implants, and those effects will be enhanced with 40 µm pores.

8.2 Methods

8.2.1 Polymer Fabrication Methods

Using the 50:50 HEMA/GMA co-polymer, three different stiffnesses were tested using the following water contents: 50%, 75%, and 85%. The exact recipes are summarized below in **Table 4**. Polymer using these recipes were fabricated with three different porous scaffold templating architectures: non-templated (NT), 40 µm pores, and 100 µm pores **(Figure 45)**. By varying water content in the pre-polymer solution, we could control the resulting polymer stiffness **(Figures 46-47, Table 5)**. These scaffolds were fabricated using the punching method: a large slide-sized scaffold was produced, and then punched out using a 23 G needle (337 µm ID/641 µm OD).

Table 4 *- Recipe of pHEMA/GMMA hydrogels with varied pre-polymerization water content. 82.5% water group is shown but was not used in the implant study.*

Water %	Volume Water (mL)	Volume HEMA (mL)	Volume GMA (mL)	Volume TEGDMA (mL)	Mass Irgacure (mg)
50%	1	0.5	0.5	0.05	5
75%	3	0.5	0.5	0.05	5
82.5%	4.95	0.5	0.5	0.05	5
85%	5.667	0.5	0.5	0.05	5

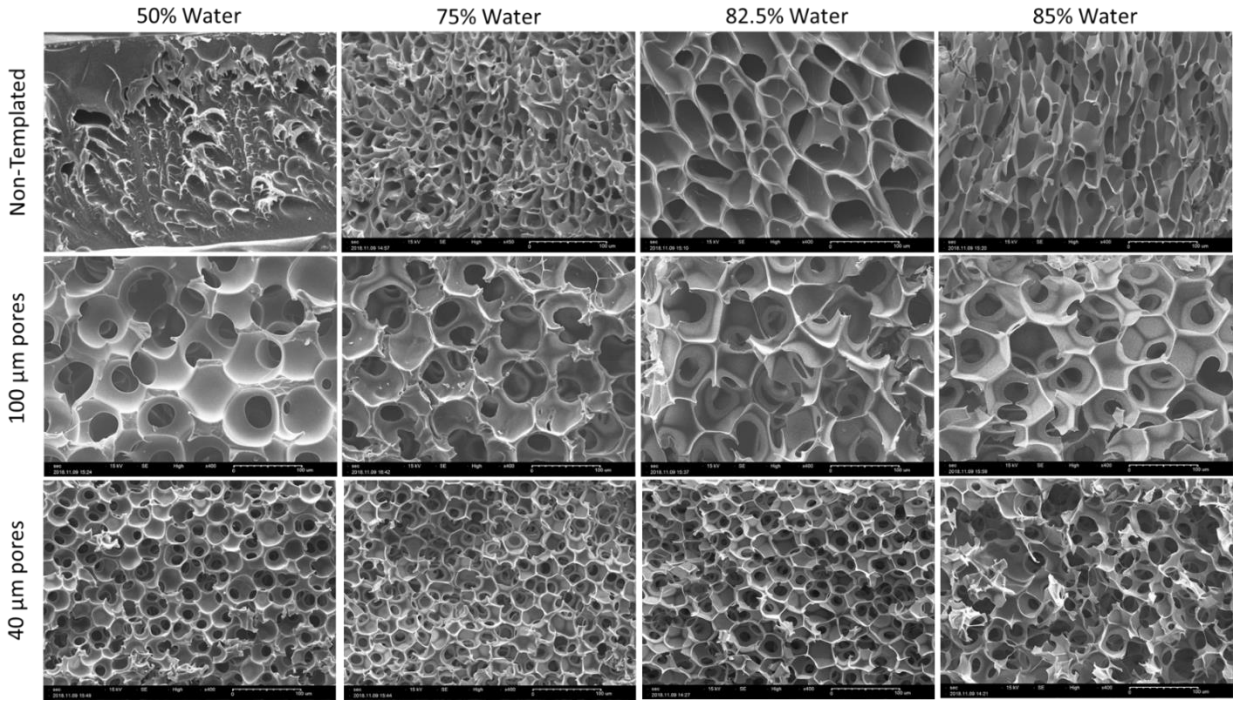

Figure 45 *- Scanning electron micrographs of pHEMA/GMA scaffolds with varying pre-polymer solution water content and porosity. 82.5% water group is shown but was not included in the implant study. Scale bars are all 100 µm.*

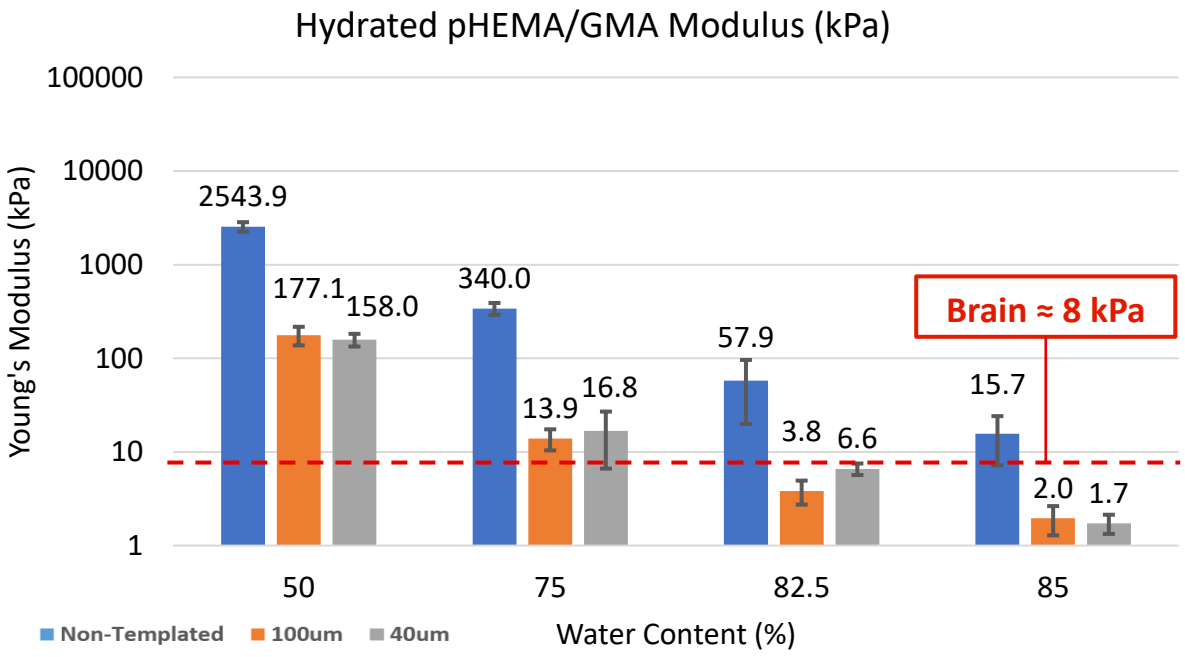

Figure 46 *– Hydrated pHEMA/GMA bulk mechanical properties as a function of water content in the pre-polymer solution and porosity. The range of stiffnesses encompass the brain's stiffness (8 kPa).*

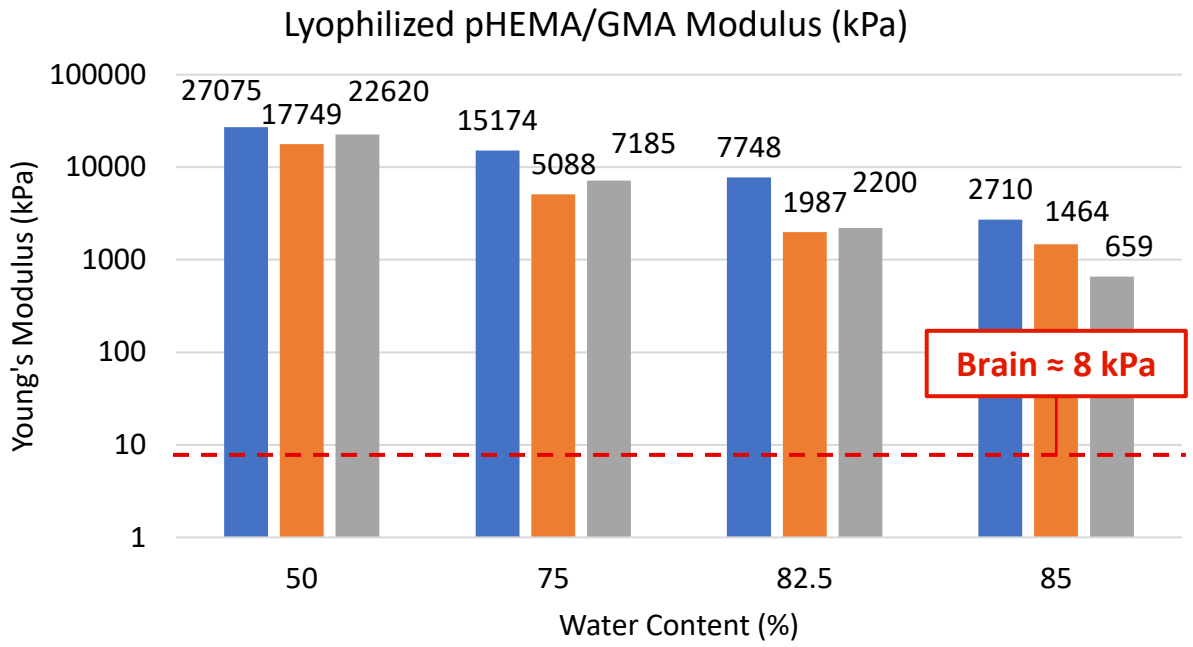

Figure 47 *– Lyophilized pHEMA/GMA bulk mechanical properties as a function of water content in the pre-polymer solution and porosity. In their lyophilized form, most implants can penetrate brain tissue and then hydrate to soften.*

Table 5 *- Average stiffness values (kPa) for materials used in this study. Showing hydrated (left) and lyophilized (right) stiffness values. 82.5% water group is shown but was not included in the implant study.*

Water Content (%)	Nonporous		100 µm pores		40 µm pores	
50	2,544	27,075	177	17,750	158	22,620
75	340	15,174	13.9	5,088	16.8	7,185
82.5	57.9	7,748	3.8	1,987	6.6	2,200
85	15.7	2,710	2	1,464	1.7	659

To ensure that rods from all polymer groups could penetrate into rat brain tissue, they were tested using a 0.83% Agar gel insertion test, which has similar mechanical properties to rat pia (Deitch, Choi, & Rousche, 2006). Because the softest (85% water) implants were unable to pass the Agar Brain insertion tests even in their lyophilized form, implants were double-reinforced with sterile-filtered 15% gelatin solution. Gelatin was used because it is not harmful to cells and it will quickly dissolve upon implantation into tissue. First, entire slide-sized scaffolds

were soaked in 15% gelatin solution at 80°C. The gel was allowed to set at 4°C, and then rods were punched from the scaffolds using the needle punching method. These rods were frozen and lyophilized. A secondary reinforcement was applied by dip-coating the lyophilized polymer rods 1cm deep into sterile-filtered 80°C 15% gelatin, allowing to dry, freezing, and lyophilizing again. Scraps left over from punching were also treated in the same way and used for endotoxin testing (Pierce Chromogenic Endotoxin Quant Kit, Thermo Scientific, A39552S). This gel reinforcement was used for all water content groups, including 50% water, 75% water, and 85% water. A no-gelatin control group was included for the 50% water content group to test if there was an effect of the gelatin on the tissue response (this group was chosen because the 50% water group was consistently stiff enough to penetrate the agar gel model). The following 12 groups listed in **Table 6** and shown in **Figure 48** were used in this study.

Table 6 *- Implant groups used.*

50% Water, Non-Templated, No Reinforcement	50% Water, Non-Templated, Gel-Reinforced	75% Water. Non-Templated Gel-reinforced	85% Water. Non-Templated Gel-reinforced
50% Water, 40 µm Pores, No Reinforcement	50% Water. 40 µm pores, Gel-Reinforced	75% Water. 40 µm pores, Gel-reinforced	85% Water. 40 µm pores, Gel-reinforced
50% Water, 100 µm pores, No Reinforcement	50% Water, 100 µm pores, Gel-reinforced	75% Water, 100 µm pores, Gel-reinforced	85% Water, 100 µm pores, Gel-reinforced

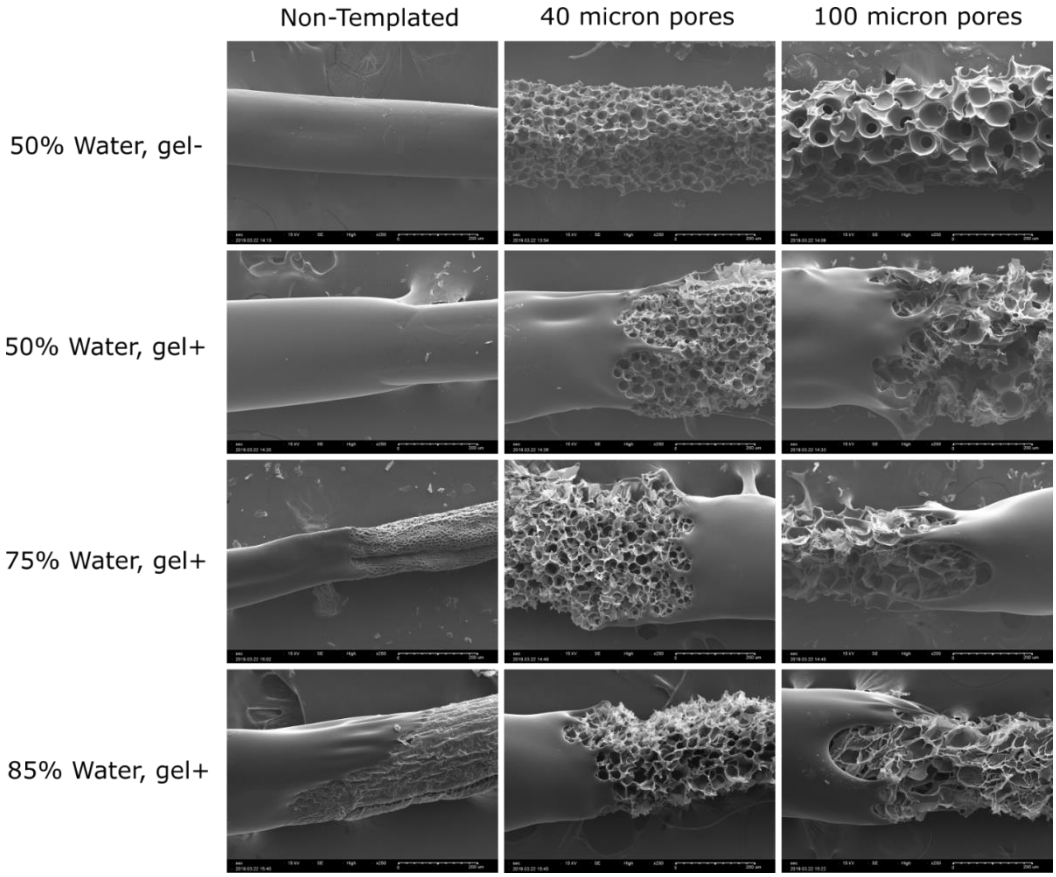

Figure 48 *- Scanning Electron Micrographs showing gelatin reinforced porous rods from each implant group.*

A similar implant procedure from Chapter 7 was repeated using the twelve scaffold groups in **Table 6**. Using two craniotomies, dura was opened and six polymer rods were implanted into each hemisphere with positions randomized **(Figure 49)**. Eight rats were implanted and allowed to recover for 4 weeks before sacrificing for histology as described in Section 4.2.2. Slices were stained with the antibodies shown in **Table 7**: GFAP and iba1 to assess effects on glial scarring, MAP2 and RECA1 will be used to visualize neurons and vasculature within and around implants, iNOS and Arg1 as M1 and M2 markers, and NeuN, NF, and MAP2 to visualize neuronal cell bodies, axons, and dendrites respectively.

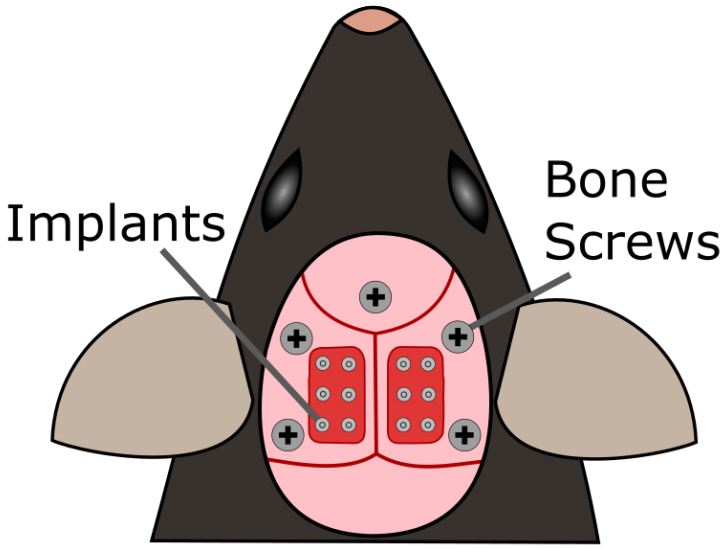

Figure 49 *- Surgical schematic for the polymer stiffness study. Two craniotomies were performed, dura was opened, and six polymer implants were placed into each hemisphere with positions randomized.*

Table 7 *- Antibodies and immunohistochemistry information used in pHEMA/GMA implant experiments.*

Antibody/stain	Target	Supplier	Catalog #	Host	Dilution
Hoechst 33342	Cell Nuclei	ThermoFisher	H3570	-	1:1000
Iba1	Microglia	Wako	016-20001	Rabbit	1:250
GFAP	Astrocytes	ThermoFisher	13-0300	Rat	1:800
CD68	Macrophages	Bio-Rad	MCA341R	Mouse	1:500
Arg1	M1 Macrophages	Cell Signaling Technologies	93668S	Rabbit	1:100
iNOS	M2 Macrophages	Abcam	ab15323	Rabbit	1:50
NeuN	Neuronal Cell Bodies	Abcam	ab177487	Rabbit	1:500
NeuroFilament	Neuronal Axons	Abcam	ab8135	Rabbit	1:1000
MAP2	Neurons	Millipore	ab5622	Rabbit	1:1000
RECA1	Endothelial Cells	Abcam	ab9774	Mouse	1:200
AlexaFluor 488 Goat anti-Rabbit IgG (H+L)	Rabbit Primary Antibodies	ThermoFisher	A-11008	Goat	1:250
AlexaFluor 594 Goat anti-Mouse IgG (H+L)	Mouse Primary Antibodies	ThermoFisher	A-11005	Goat	1:250
AlexaFluor 594 Goat anti-Rat IgG (H+L)	Rat Primary Antibodies	ThermoFisher	A-11007	Goat	1:250

The following antibodies were also tested, but it was determined they did not work well for our experiments because the isotype control showed signal, or the background signal was high: CD86 conjugated to PE (ThermoFisher 12-0860-83) and NOS2 (Santa Cruz sc-7271).

8.2.2 Tissue Histology Analysis

Images were captured using a Zeiss LSM 510 confocal laser scanning microscope using 3x3 tiled scans with a Zeiss Plan-Apocrhomat 20X/0.75 objective lens. All samples that used the same antibodies utilized the exact same microscope settings. Three fluors were used in each sample: Hoechst33342, AlexaFluor 488, and AlexaFluor 594. For Hoechst33342 samples, pinhole opening was 41 µm, with 1.53 Airy Units for an optical section thickness of 2.5 µm. For AlexaFluor 488 samples, pinhole opening was 40 µm, with 1.26 Airy Units for an optical section thickness of 2.5 µm. For AlexaFluor 594 samples, pinhole opening was 39 µm, with 1 Airy Unit for an optical section thickness of 2.5 µm. All samples used Digital Offset = 0, and Digital Gain = 1.0. Other imaging settings for each sample are shown below in **Table 8**.

Table 8 *- Imaging settings for each marker.*

Primary Antibody/stain	Fluor	Excitation Laser (nm)	Emission Filter (nm)	Laser Power (%)	Master Gain (V)
Hoechst 33342	Hoechst 33342	405	410-470	0.90	675
Iba1	AF488	488	410-550	0.29	630
GFAP	AF594	561	576-700	0.15	575
CD68	AF594	561	576-700	0.40	575
Arg1	AF488	488	410-550	0.35	700
iNOS	AF488	488	410-550	0.25	710
NeuN	AF488	488	410-550	0.40	650
NeuroFilament	AF488	488	410-550	0.29	630
MAP2	AF488	488	410-550	0.40	640
RECA1	AF594	561	576-700	0.30	765

Image analysis was performed using FIJI (ImageJ). For glial cells (GFAP for astrocytes and iba1 for microglia), the Radial Profile Angle plugin was used to measure fluorescence profiles radially outwards from the center of each implant. During acquisition, the diameter of

each implant was recorded, and the implant edges were shifted to match each other to minimize any variance in implant diameter. Then, the area under the fluorescence curve in 25 μm bins was calculated for easy comparison between groups (see **Figure 50** for a demonstration). Two-Way ANOVA with α=0.05 was used to determine if there was a statistically significant effect of water % (stiffness) or pore size.

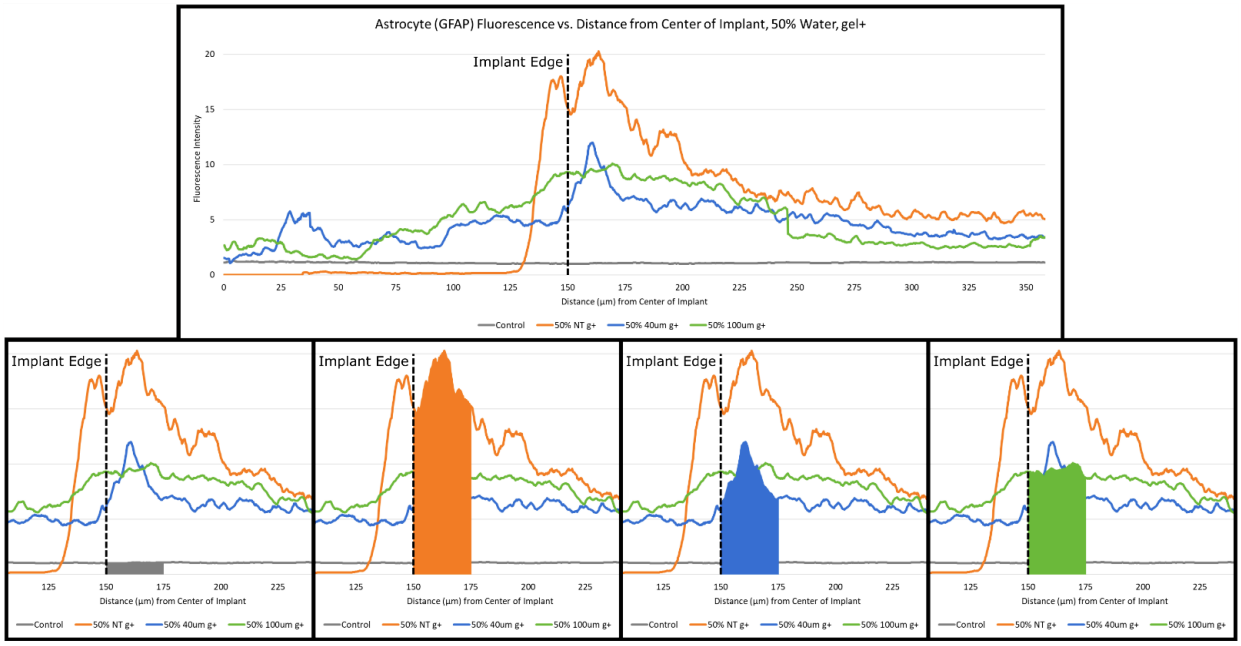

Figure 50 *- Demonstration of the area under the curve measurements for glial encapsulation.*

For neuronal cell bodies (NeuN), a custom-made FIJI script was developed to assist in cell counting and calculation of neuronal density. This script asked the user to define the outline of each implant, and then created 50 μm thick bands extending from the implant edge. The area of each band was recorded, and the number of neurons within each band was counted using the Cell Counter function in ImageJ (see Figure 51 for a demonstration). Cell density was calculated by dividing the number of neuron cell bodies counted by the area within each band. Two-way ANOVA with α=0.05 was used to determine if there was a statistically significant difference among the groups.

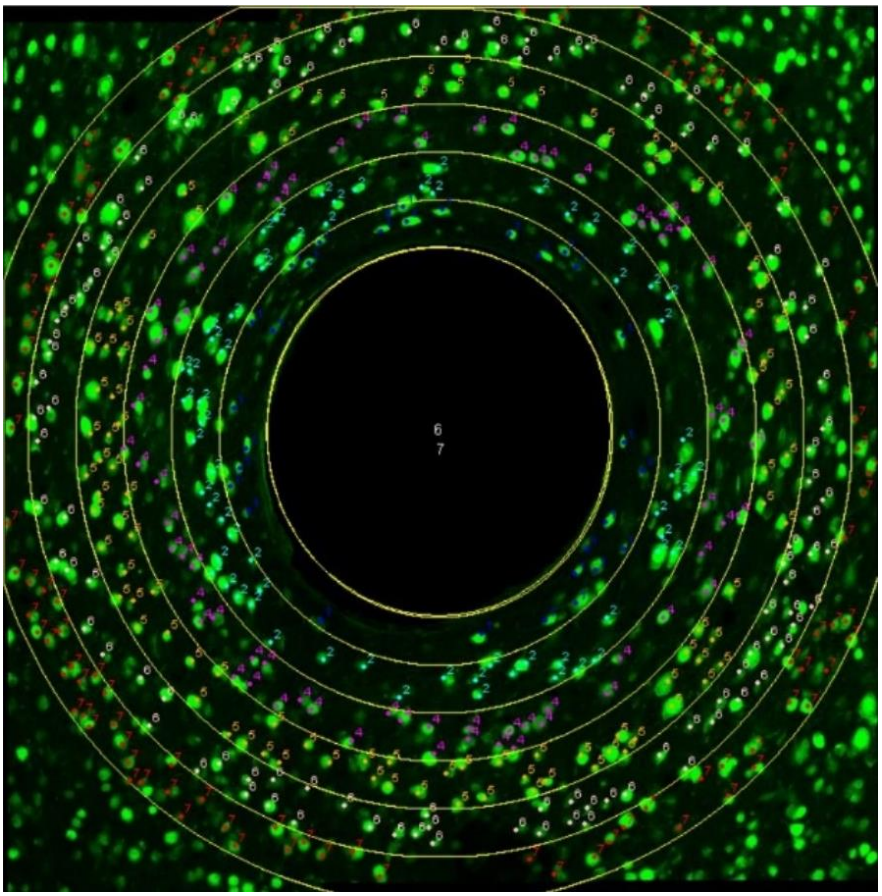

Figure 51 *- Demonstration of neuronal counting within 50 μm bands.*

For M1 (iNOS), M2 (Arg1), axons (NeuroFilament), and dendrites (MAP2), a custom-made FIJI macro was developed to perform a measurement of the overall fluorescence of each image for every image in a folder. Each image was imported, re-sized, changed to 16-bit, and underwent background subtraction using a 50 μm radius rolling ball method. Then, automatic thresholding was applied, and integrated density (sum of all pixels in the selection) was measured on the thresholded pixels. The intention of this method was to select only pixels that positively expressed the marker and measure the fluorescence of those pixels. ANOVA with $\alpha=0.05$ was used to determine if there was a statistically significant difference among the groups. If a difference was observed, post-hoc Tukey tests were used to compare each pair to determine which groups were significantly different.

8.3 Results

Glial Encapsulation (GFAP and iba1)

Representative confocal microscopy images for glial encapsulation are shown in **Figure 52**. Both 50% non-templated groups showed high levels of astrocyte encapsulation compared to softer and porous templated groups **(Figure 53)**. Two-Way ANOVA showed that astrocyte fluorescence within 25 µm of the implant is significantly affected by both pore size (p=0.002) and water % (p=0.03). Microglia fluorescence within 25 µm of the implant was not significantly affected by pore size or water % (**Figure 54)**.

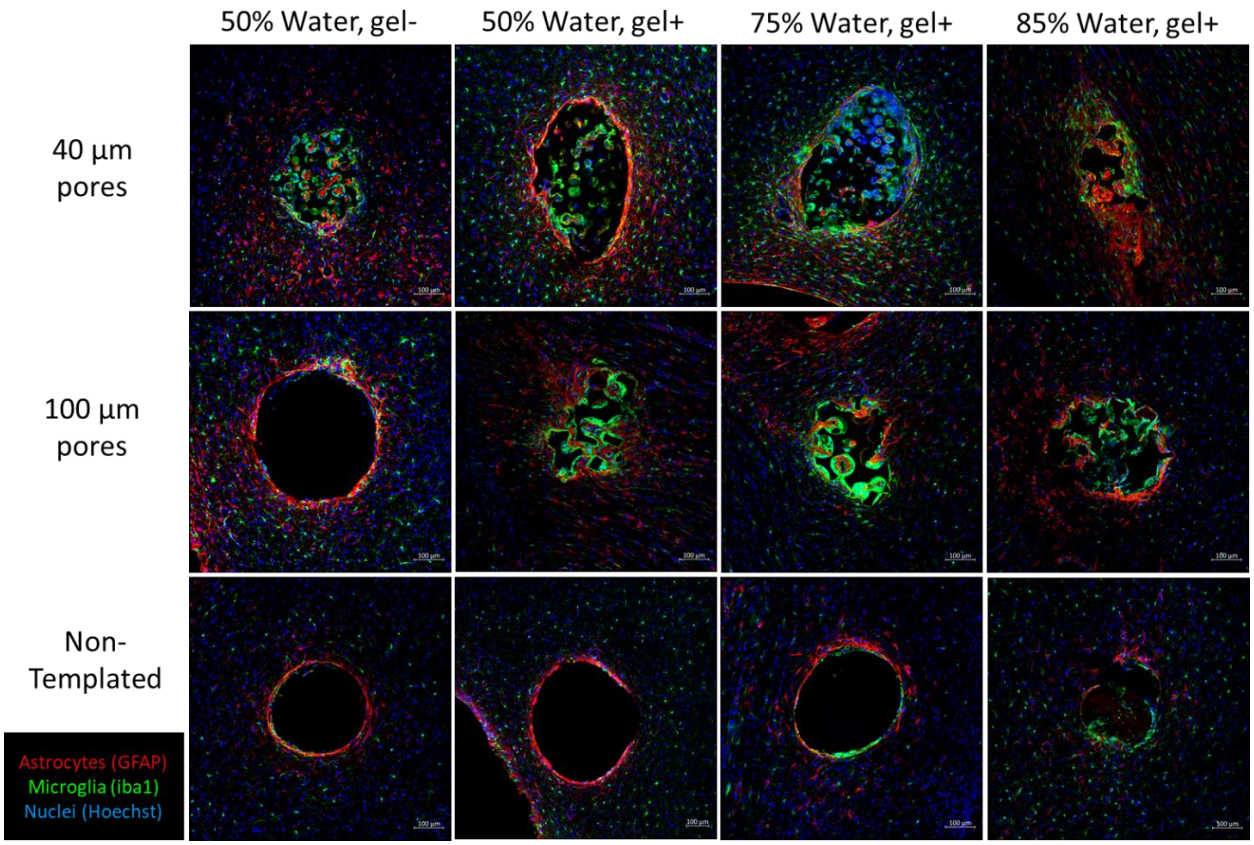

Figure 52 *- Confocal microscopy images of glial encapsulation for each group. Red shows Astrocytes labeled by GFAP, green shows microglia labeled by iba1, and blue shows cell nuclei labeled by Hoechst. Scale bars are 100µm.*

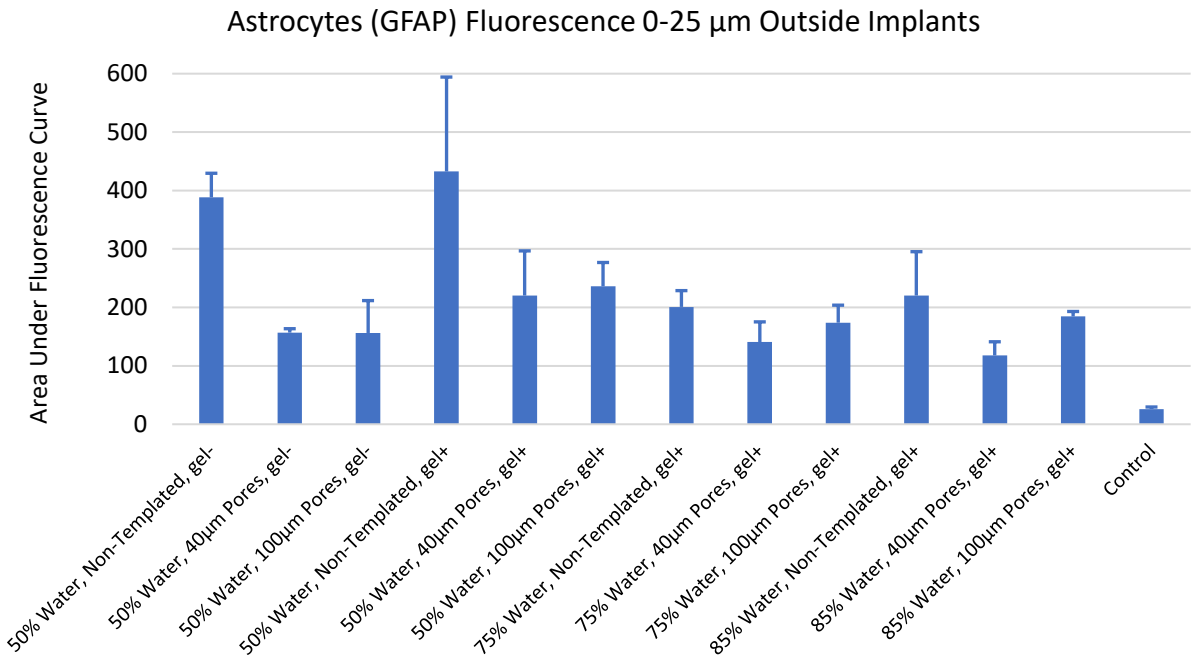

Figure 53 *- Astrocyte encapsulation 0-25 µm outside implants. Two-Way ANOVA revealed a significant effect from Pore Size (p=0.002) and Water % (p=0.03).*

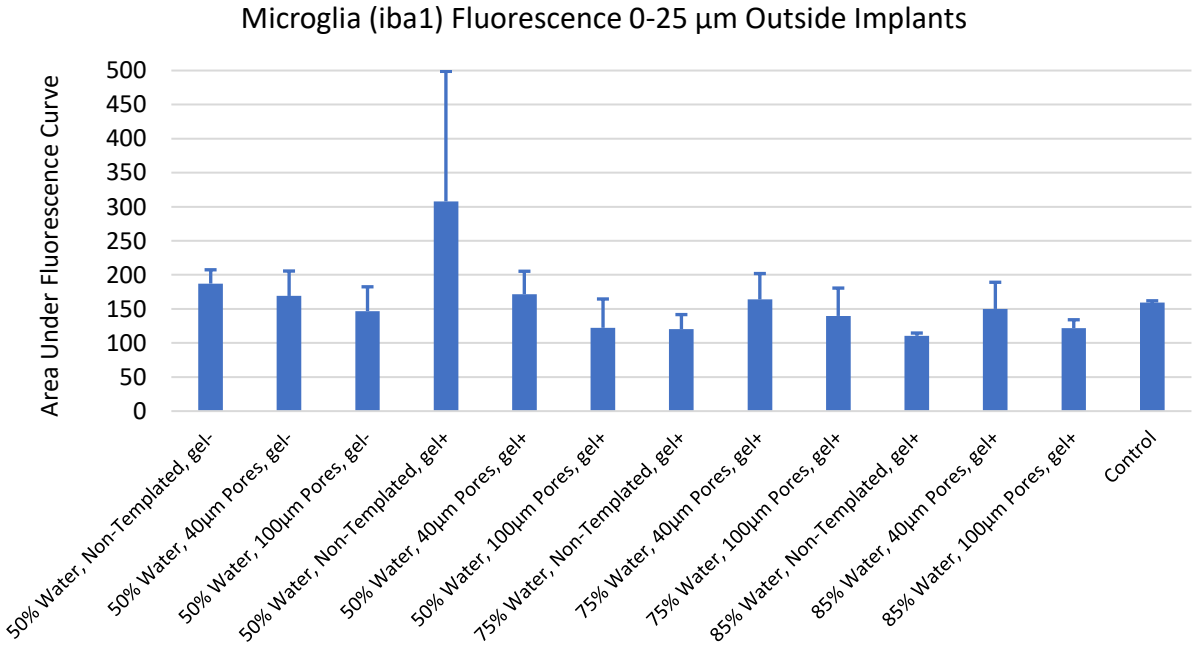

Figure 54 *- Microglia encapsulation 0-25 µm outside implants. There were no significant differences between groups.*

Neuronal Markers (NeuN, NF, and MAP2)

Neuron density around stiffer, non-templated implants was lower than around softer, porous templated implants **(Figure 55)**. In the 50µm band closest to the implant, two-way ANOVA showed that neuron density was significantly affected by both pore size (p=0.014) and water % (p=0.129). For Axons (NeuroFilament, **Figure 56**) and dendrites (MAP2, **Figure 57**), there were no significant differences in fluorescence (integrated density). Surprisingly, for some porous implants, there were cells positively labeled with neuronal markers within the pores **(NeuN: Figure 58, NF: Figure 59, MAP2, Figure 60)**.

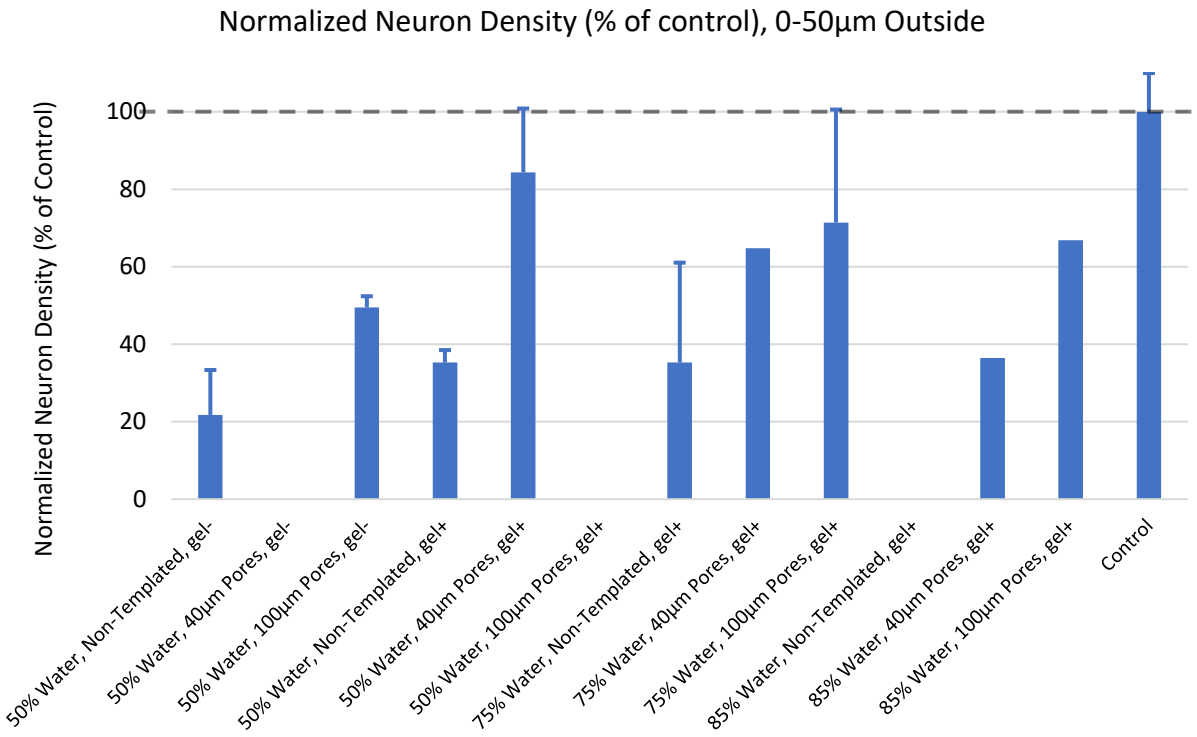

Figure 55 *- Normalized Neuron Density plotted as % of control tissue. Two-Way ANOVA revealed a significant effect of Pore Size (p=0.014), but not Water % (p=0.129). Dotted line indicates the 100% line, or the level of control.*

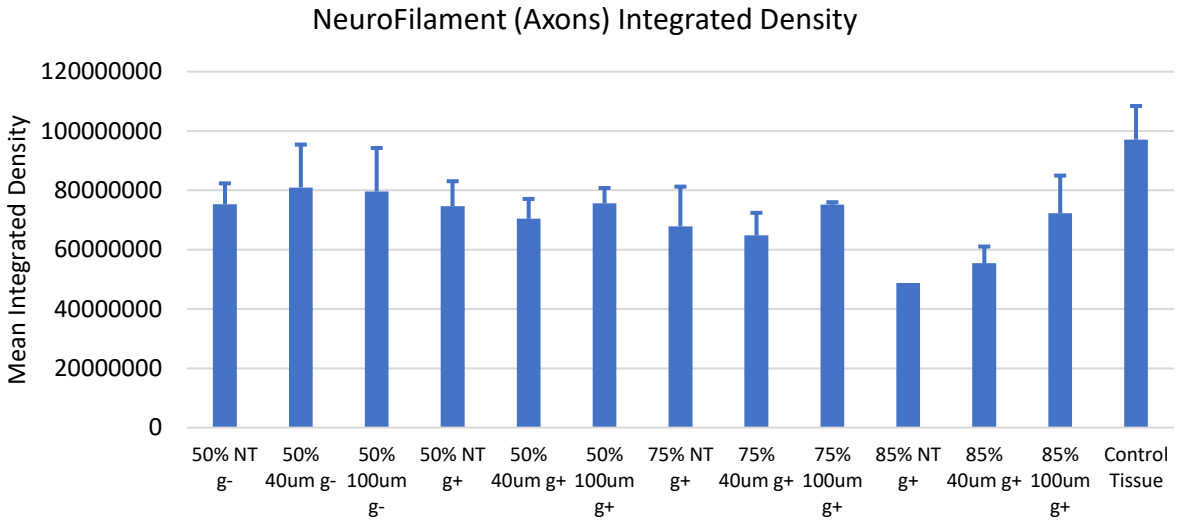

Figure 56 *- Average Integrated Density of NeuroFilament images. There were no significant differences between groups.*

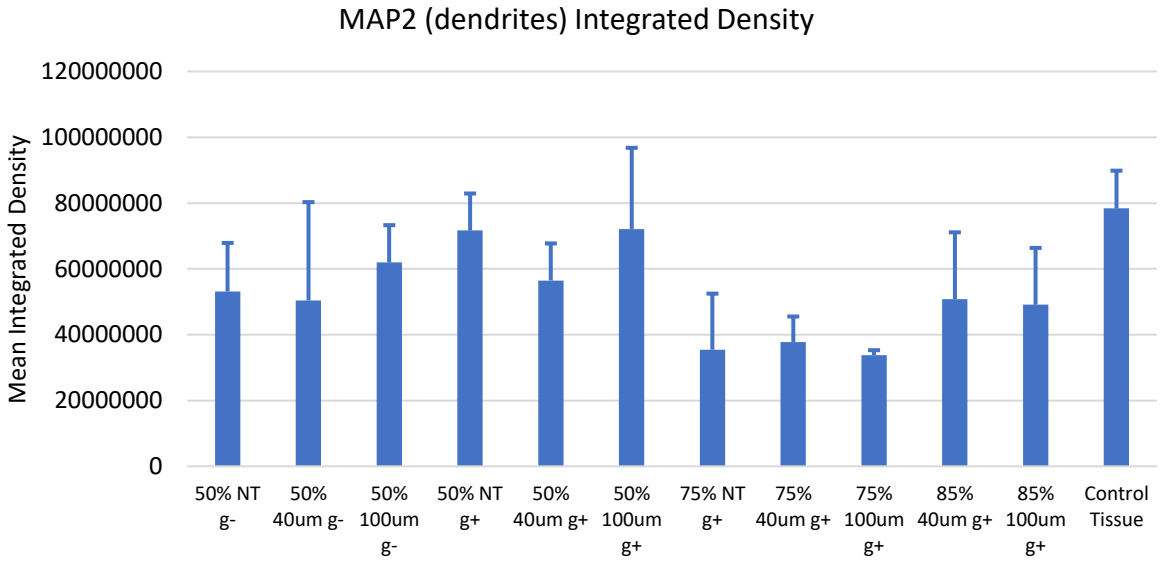

Figure 57 *- Average Integrated Density for MAP2 images. There were no significant differences between groups.*

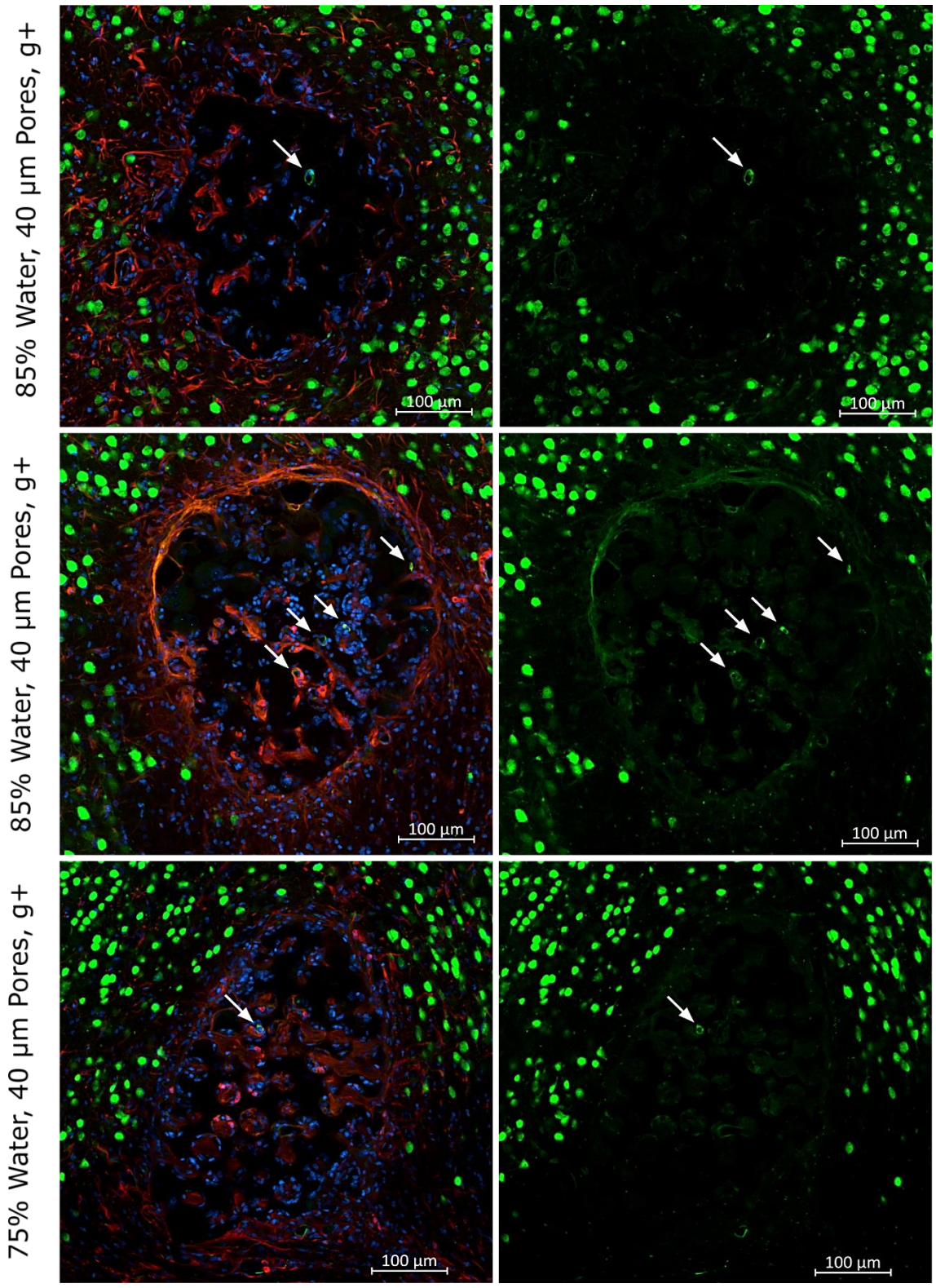

Figure 58 *- Examples of positive NeuN expression within 40 µm pores. Green is NeuN (neurons), red is GFAP (astrocytes), and blue is Hoechst (cell nuclei). Scale bars are 100 µm.*

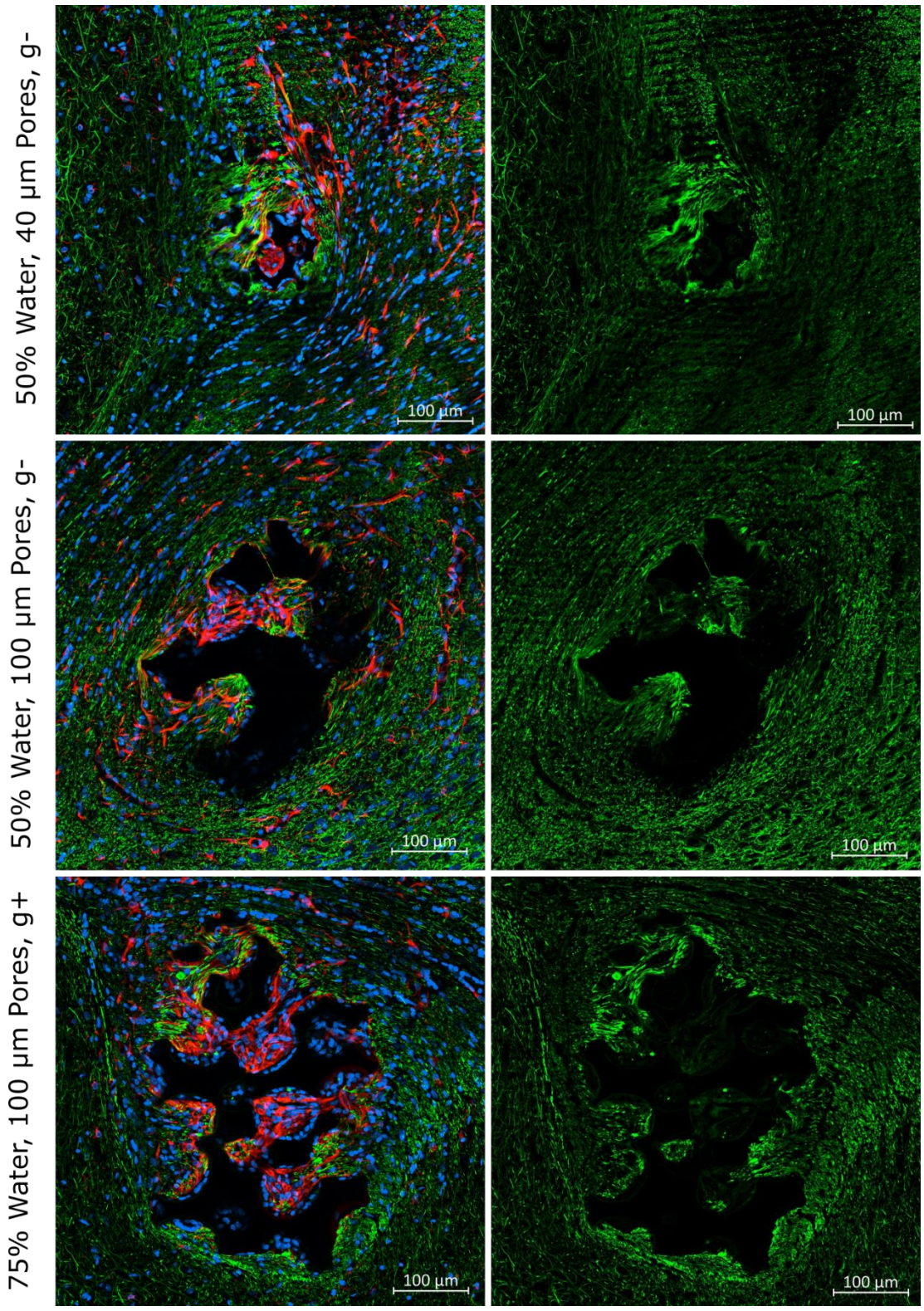

Figure 59 *- Examples of positive NeuroFilament expression within pores. Green is NeuroFilament (axons), red is GFAP (astrocytes), and blue is Hoechst (cell nuclei). Scale bars are 100 µm.*

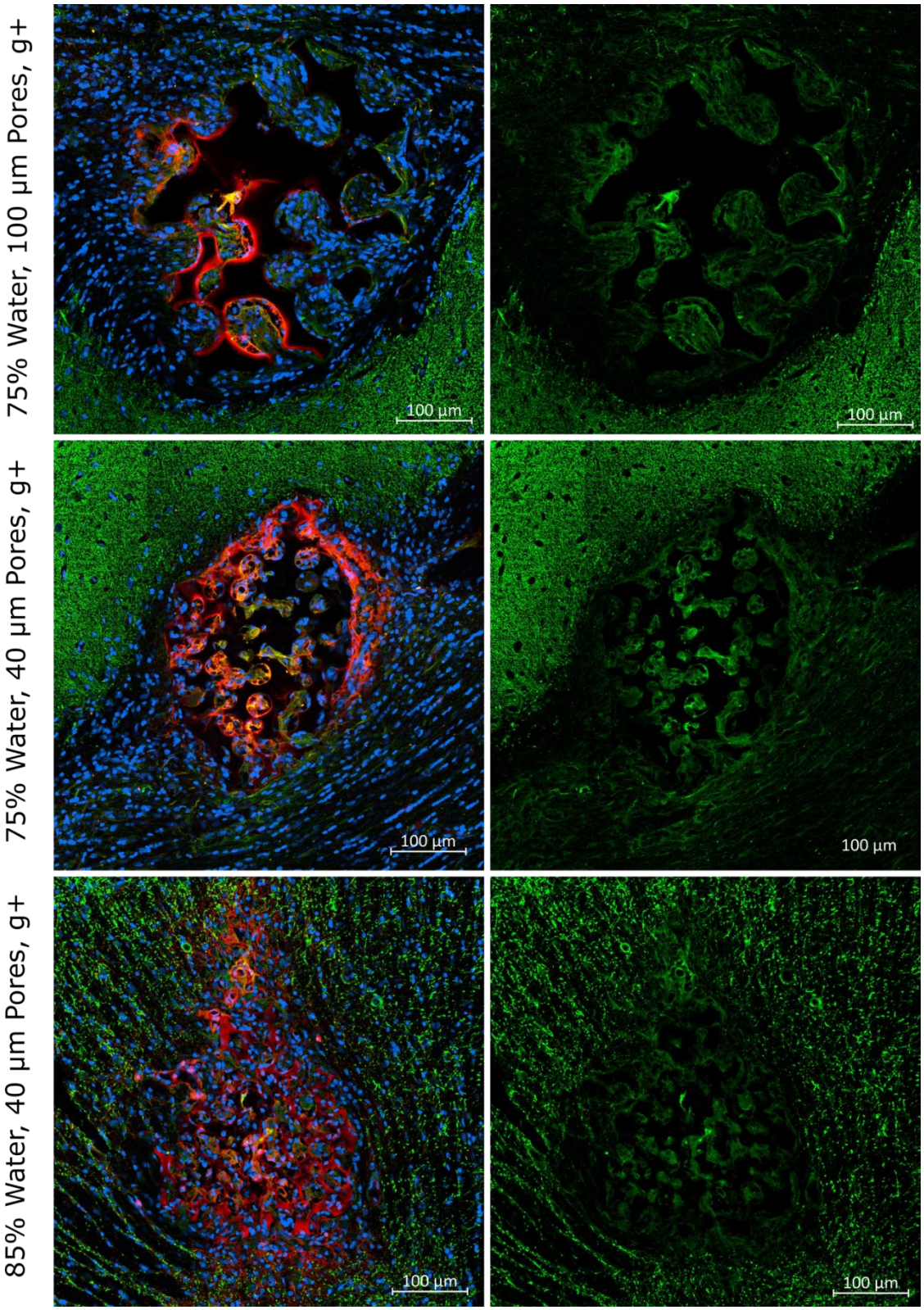

Figure 60 *- Examples of MAP2 expression within pores. Green is MAP2 (dendrites), red is RECA1 (endothelium), and blue is Hoechst (cell nuclei). Scale bars are 100 µm.*

Inflammatory Markers (iNOS and Arg1)

Using integrated density, two-way ANOVA revealed no significant differences for both proinflammatory marker iNOS and prohealing marker Arg1. However, a slight trend was observed: iNOS seemed higher for stiffer implants (higher on left side of plot in **Figure 61**), and Arg1 seemed higher for softer implants (higher on right in **Figure 62**). Additionally, for stiffer (50% water) implant groups, the 40µm porous groups showed decreased iNOS fluorescence **(Figure 61)**.

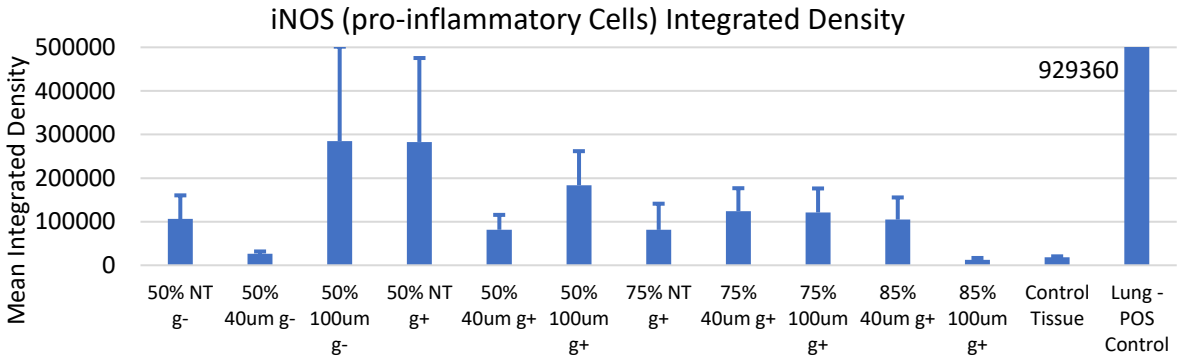

Figure 61 *- Average Integrated Density for iNOS images.There were no significant differences between groups.*

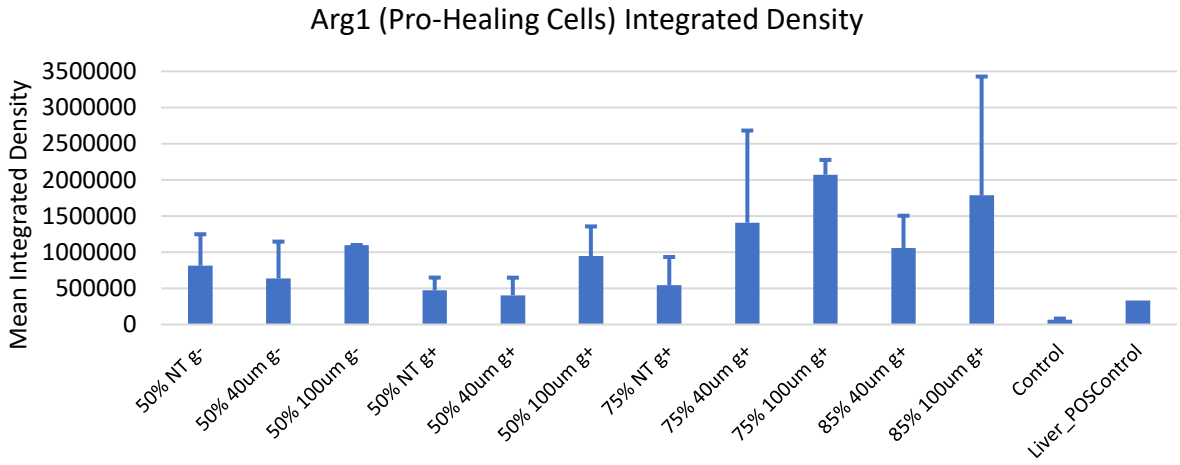

Figure 62 *- Average Integrated Density for Arg1 images. There were no significant differences between groups.*

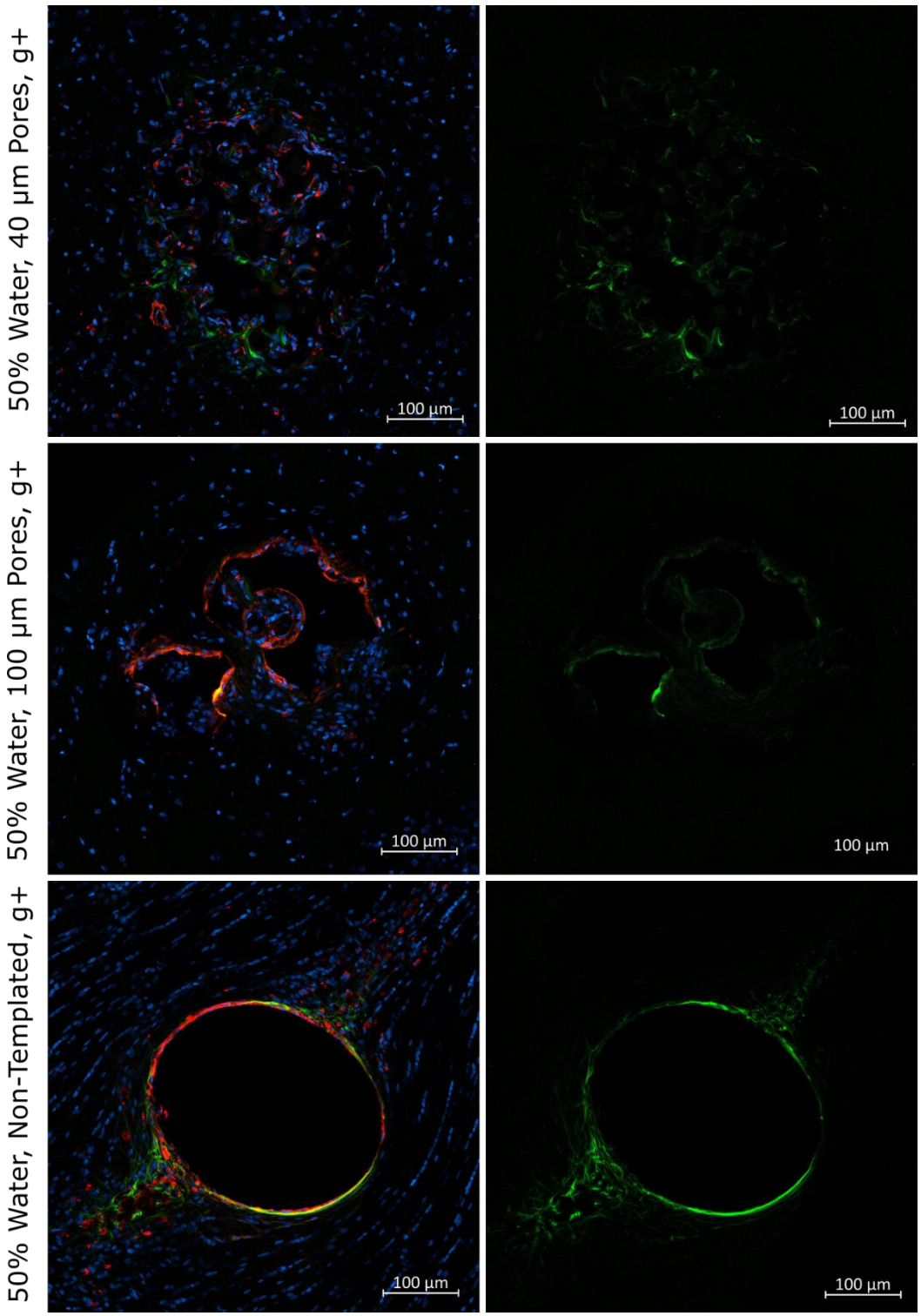

Figure 63 *- Examples of iNOS expression around 50% Water, gel-reinforced implants. Green is iNOS (proinflammatory marker), red is CD68 (macrophages), and blue is Hoechst (cell nuclei). Scale bars are 100 µm.*

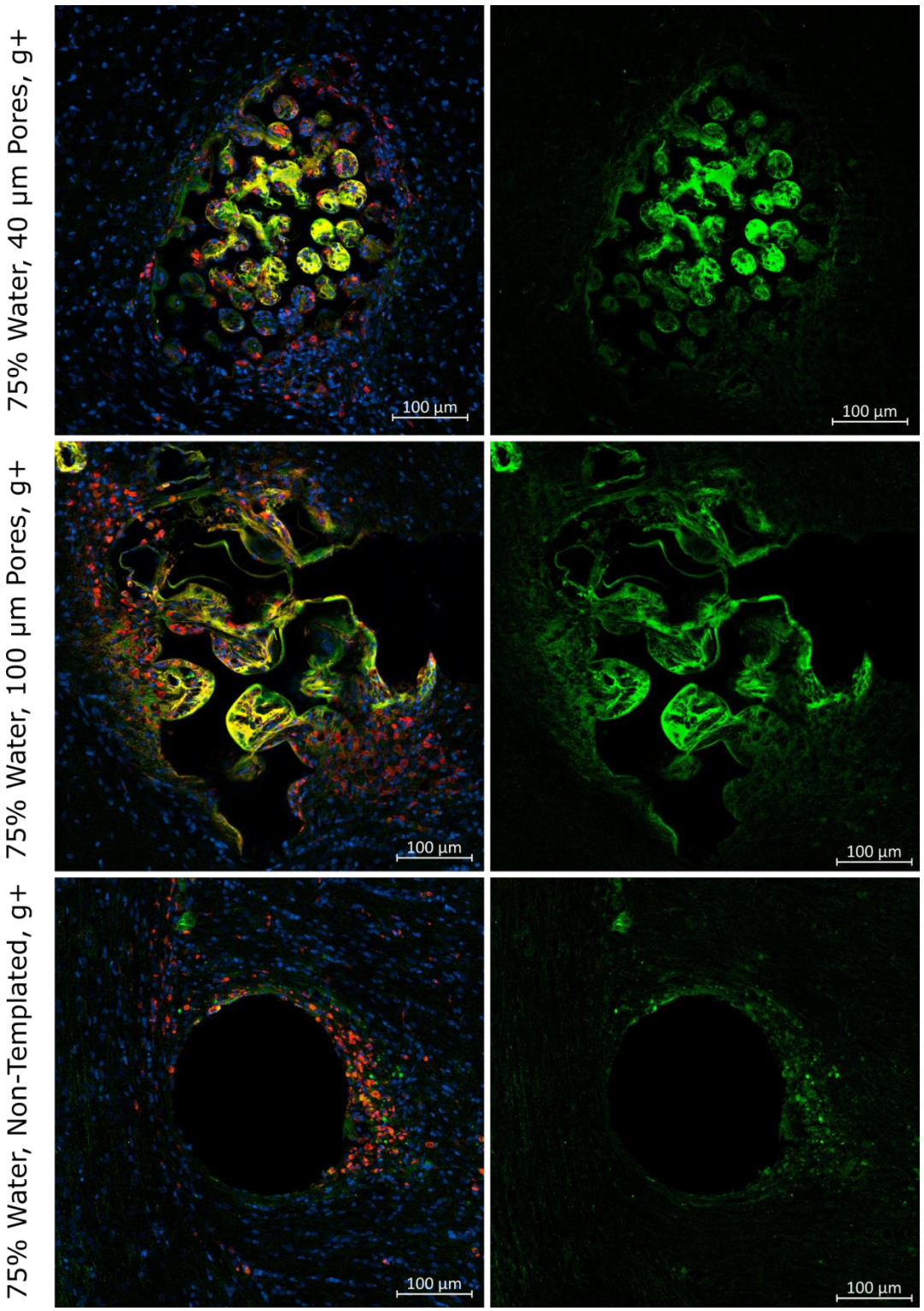

Figure 64 *– Examples of Arg1 expression around 75% Water, gel-reinforced implants. Green is Arg1 (prohealing marker), red is CD68 (macrophages), and blue is Hoechst (cell nuclei). Scale bars are 100 µm.*

8.4 Discussion and Conclusions

So far, no implanted neural interfaces have been able to overcome the foreign body response. In order to reliably record neural signals for many years, glial encapsulation must be minimized and neuronal proximity to recording sites must be maximized. In Chapter 7, we observed that porous hydrogels (pHEMA) reduced glial encapsulation at 1 week after implantation, but those improvements did not continue to 4 weeks after implantation. In this study, we improved upon those results by using softer hydrogels that matched the stiffness of the brain.

We hypothesized that both hydrogel stiffness and pore size play a role in the neuroinflammatory environment around brain implants. We found that both stiffness and pore size significantly affected astrocyte encapsulation, and pore size significantly affected neuronal density surrounding implanted hydrogels. Additionally, many porous scaffolds showed positive staining of neuronal markers within the porous structure. This is an important observation, because the capability of PTS to harbor neurons increases the chances of successful neural recordings once recording devices are incorporated within PTS. Although positive NeuN signal was observed within PTS, the shape and level of fluorescence was slightly different than neurons outside implants. We speculate that these neurons might be immature neurons. The question then arises: where did these immature neurons come from? A few possibilities exist. First, they may have spawned from other brain regions where neurogenesis is known to occur, such as the subventricular zone. Second, the properties of PTS may have caused neurogenesis to occur within the porous structure itself. Third, cells that have already infiltrated into the PTS may have re-differentiated into neurons. This third possibility is a running theory in our lab, as we have observed that PTS implanted into other tissues results in various tissue and cell types within the pores (especially blood vessel formation), and we speculate that infiltrating macrophages may be re-differentiation into those various cell types such as vascular

endothelium. To investigate these possibilities, future studies must be performed. We are already preparing to label remaining tissue slices from this study with markers for neurogenesis (ki67, doublecortin). We will also label slices with synaptophysin to see if the neurons within the pores are forming functional connections with other neurons.

Based on this analysis, there were no significant effects on microglia encapsulation, neuronal processes, proinflammatory markers, or prohealing markers. However, other analysis could be performed. This study used a bulk fluorescence analysis by thresholding each image and measuring the sum of the fluorescence of all thresholded images, called integrated density. While this method was faster and easier to analyze all images, other methods such as cell counting might result in more definitive results and will be tested in the future.

Three groups were not coated with gelatin as a control (50% Water, gel- groups). Overall, there were no statistically significant effects of gelatin coating. Although it was not a significant effect, the 50% water, non-templated, gel+ group showed a higher iba1 fluorescence than other groups, suggesting an effect on microglia.

Despite the positive observations, there are several confounding factors and changes that could have improved this study. Firstly, the gel coating method resulted in an increase in variance of implant size – some implants had a larger footprint from the gel coating than others. It is believed that implant size affects glial encapsulation (Stice, Gilletti, Panitch, & Muthuswamy, 2007), so this may have affected results. The gel coating was used to reinforce implants so they were strong enough to penetrate into brain tissue. However, other methods could have been explored which would have not changed implant size. Here is one proposed method. Before punching rods, bulk porous scaffolds could be infiltrated with gelatin. Then, rods could be punched, and the gelatin inside the pores could be cross-linked using EDC:NHS chemistry. This would increase the stiffness of implants, allowing them to penetrate brain tissue while not

increasing their size. However, the cross-linked gelatin would take longer to dissolve than un-cross-linked gelatin, which might alter results.

Secondly, twelve implants were used per animal. There were some positive aspects of this approach: since all polymer groups were implanted into each animal, inter-animal variation was reduced; and tissue staining and analysis could be performed at the same implant depth for each group. However, the large number of implants may have caused excess tissue damage – a few animals showed tissue lesions within a few hundred μm of the brain's surface. It may be a good idea to use less implants per animal in the future. It should be noted, however, that some studies use a large number of microelectrodes in one animal, so twelve implants per animal may be acceptable.

Thirdly, the implant location was poorly chosen for neuronal counting. The area around the hippocampus has a wide variability in neuronal density – some areas have barely any neurons, whereas the hippocampus itself is packed densely. Because most implants were located around the hippocampus, this was a bad location to compare neuronal density around implants. Because of this, any implants near the hippocampus or the neuron-scarce zones around the hippocampus were excluded from neuronal counting. Only implants in the tissue rostral to the hippocampus with a wide field of homogenously distributed neurons were used for neuronal counting. In the future, I would recommend implanting further rostral to hit this field of neurons with all implant groups.

Chapter 9: Conclusions and Future Directions

9.1 Conclusions and Future Directions

These studies demonstrated that PTS can be used as a scaffold for neural engineering applications. PTS stiffness and porosity can have a significant effect on the foreign body response in the brain; and soft, porous hydrogel implants can support neurons within the pores. However, the most important factor in determining the success of a brain-computer interface was not investigated: the ability to record neural signals long-term. In these studies, a recording device was not used. In the future, implant studies combining porous templated scaffolds with neural recording devices should be explored. Specifically, it remains unknown whether a recording device encapsulated within porous templated scaffold can successfully record neural signals since the recording sites will be embedded within the porous structure. We hypothesize that such a feat is possible, because of the observations that axon, dendrite, and neuron cell body markers showed positive expression within the pores.

Although no recordings were performed, we have shown that microwires, tetrodes, and planar silicon probes can be embedded within porous rods **(Figure 65)**. However, these were incorporated in the beginning of the fabrication process, so recording devices were exposed to organic solvents. It is likely that exposure to organic solvents affected the functionality of such recording devices, so a method should be developed to incorporate a recording device after the porous structure is already fabricated. For example, a planar silicon probe could be inserted into a porous polymer rod.

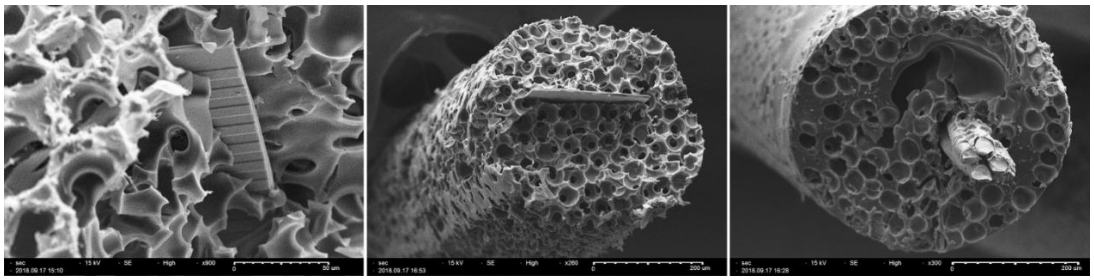

Figure 65 *- Scanning Electron Micrographs of PTS with recording devices incorporated - Michigan Arrays (planar silicon probes) on left and center; Tetrode on right.*

Bibliography

Aguzzi, A., Barres, B. a, & Bennett, M. L. (2013). or Something Else ? *Science*, *339*(6116), 156–161. https://doi.org/10.1126/science.1227901

Badylak, S. F., Valentin, J. E., Ravindra, A. K., McCabe, G. P., & Stewart-Akers, A. M. (2008). Macrophage Phenotype as a Determinant of Biologic Scaffold Remodeling. *Tissue Engineering Part A*, *14*(11), 1835–1842. https://doi.org/10.1089/ten.tea.2007.0264

Barrese, J. C., Rao, N., Paroo, K., Triebwasser, C., Vargas-Irwin, C., Franquemont, L., & Donoghue, J. P. (2013). Failure mode analysis of silicon-based intracortical microelectrode arrays in non-human primates. *Journal of Neural Engineering*, *10*(6). https://doi.org/10.1088/1741-2560/10/6/066014

Bartneck, M., Heffels, K.-H., Pan, Y., Bovi, M., Zwadlo-Klarwasser, G., & Groll, J. (2012). Inducing healing-like human primary macrophage phenotypes by 3D hydrogel coated nanofibres. *Biomaterials*, *33*(16), 4136–4146. https://doi.org/10.1016/j.biomaterials.2012.02.050

BASSO, D. M., BEATTIE, M. S., & BRESNAHAN, J. C. (1995). A Sensitive and Reliable Locomotor Rating Scale for Open Field Testing in Rats. *Journal of Neurotrauma*, *12*(1), 1–21. https://doi.org/10.1089/neu.1995.12.1

Bhrany, A. D., Irvin, C. A., Fujitani, K., Liu, Z., & Ratner, B. D. (2013). Evaluation of a sphere-templated polymeric scaffold as a subcutaneous implant. *JAMA Facial Plastic Surgery*, *15*(1), 29–33. https://doi.org/10.1001/2013.jamafacial.4

Biran, R., Martin, D. C., & Tresco, P. A. (2005). Neuronal cell loss accompanies the brain tissue response to chronically implanted silicon microelectrode arrays. *Experimental Neurology*, *195*(1), 115–126. https://doi.org/10.1016/j.expneurol.2005.04.020

Boehler, C., Kleber, C., Martini, N., Xie, Y., Dryg, I., Stieglitz, T., … Asplund, M. (2017). Actively controlled release of Dexamethasone from neural microelectrodes in a chronic in vivo study. *Biomaterials*, *129*. https://doi.org/10.1016/j.biomaterials.2017.03.019

Bota, P. C. S., Collie, A. M. B., Puolakkainen, P., Vernon, R. B., Sage, E. H., Ratner, B. D., & Stayton, P. S. (2010). Biomaterial topography alters healing in vivo and monocyte/macrophage activation in vitro. *Journal of Biomedical Materials Research. Part A*, *95*(2), 649–657. https://doi.org/10.1002/jbm.a.32893

Bratton, S. L., Chestnut, R. M., Ghajar, J., McConnell Hammond, F. F., Harris, O. A., Hartl, R., … Wright, D. W. (2007). IX. Cerebral Perfusion Thresholds. *Journal of Neurotrauma*, *24*(supplement 1), S-59-S-64. https://doi.org/10.1089/neu.2007.9987

Brown, B. N., Ratner, B. D., Goodman, S. B., Amar, S., & Badylak, S. F. (2012). Macrophage polarization: An opportunity for improved outcomes in biomaterials and regenerative medicine. *Biomaterials*, *33*(15), 3792–3802. https://doi.org/10.1016/j.biomaterials.2012.02.034

Brown, B. N., Valentin, J. E., Stewart-Akers, A. M., McCabe, G. P., & Badylak, S. F. (2009). Macrophage phenotype and remodeling outcomes in response to biologic scaffolds with and without a cellular component. *Biomaterials*, *30*(8), 1482–1491. https://doi.org/10.1016/j.biomaterials.2008.11.040

Bryers, J. D., Giachelli, C. M., & Ratner, B. D. (2012). Engineering biomaterials to integrate and heal: the biocompatibility paradigm shifts. *Biotechnology and Bioengineering*, *109*(8), 1898–1911. https://doi.org/10.1002/bit.24559

Cao, Y., Chen, Y., & DeVivo, M. (2011). Lifetime Direct Costs After Spinal Cord Injury. *Topics in Spinal Cord Injury Rehabilitation*, *16*(4), 10–16. https://doi.org/10.1310/sci1604-10

Carlson, D. E., Vogelstein, J. T., Qisong Wu, Wenzhao Lian, Mingyuan Zhou, Stoetzner, C. R., … Carin, L. (2014). Multichannel Electrophysiological Spike Sorting via Joint Dictionary Learning and Mixture Modeling. *IEEE Transactions on Biomedical Engineering*, *61*(1), 41–54. https://doi.org/10.1109/TBME.2013.2275751

Chen, Y. J., Zhu, H., Zhang, N., Shen, L., Wang, R., Zhou, J. S., … Lü, H. Z. (2015). Temporal kinetics of macrophage polarization in the injured rat spinal cord. *Journal of Neuroscience Research*, *93*(10), 1526–1533. https://doi.org/10.1002/jnr.23612

Collinger, J. L., Wodlinger, B., Downey, J. E., Wang, W., Tyler-Kabara, E. C., Weber, D. J., … Schwartz, A. B. (2013). High-performance neuroprosthetic control by an individual with tetraplegia. *The Lancet*, *381*(9866), 557–564. https://doi.org/10.1016/S0140-6736(12)61816-9

Deitch, S., Choi, M., & Rousche, P. (2006). Brain Model for Microelectrode Implantation Testing.

Doherty, T. M., Kastelein, R., Menon, S., Andrade, S., & Coffman, R. L. (1993). Modulation of murine macrophage function by IL-13. *Journal of Immunology (Baltimore, Md. : 1950)*, *151*(12), 7151–7160. Retrieved from http://www.ncbi.nlm.nih.gov/pubmed/7903102

Freire, M. A. M., Morya, E., Faber, J., Santos, J. R., Guimaraes, J. S., Lemos, N. A. M., … Nicolelis, M. A. L. (2011). Comprehensive analysis of tissue preservation and recording quality from chronic multielectrode implants. *PLoS ONE*, *6*(11), 23–27. https://doi.org/10.1371/journal.pone.0027554

Fukano, Y., Usui, M. L., Underwood, R. A., Isenhath, S., Marshall, A. J., Hauch, K. D., … Fleckman, P. (2010). Epidermal and dermal integration into sphere-templated porous poly(2-hydroxyethyl methacrylate) implants in mice. *Journal of Biomedical Materials Research - Part A*, *94*(4), 1172–1186. https://doi.org/10.1002/jbm.a.32798

Fukano, Yuko, Knowles, N. G., Usui, M. L., Underwood, R. A., Hauch, K. D., Marshall, A. J., … Olerud, J. E. (2006). Characterization of an in vitro model for evaluating the interface between skin and percutaneous biomaterials. *Wound Repair and Regeneration : Official Publication of the Wound Healing Society [and] the European Tissue Repair Society*, *14*(4), 484–491. https://doi.org/10.1111/j.1743-6109.2006.00138.x

Galperin, A., Long, T. J., Garty, S., & Ratner, B. D. (2013). Synthesis and fabrication of a degradable poly(N-isopropyl acrylamide) scaffold for tissue engineering applications. *Journal of Biomedical Materials Research. Part A*, *101*(3), 775–786. https://doi.org/10.1002/jbm.a.34380

Geng, C. K., Cao, H. H., Ying, X., Zhang, H. T., & Yu, H. L. (2015). The effects of hyperbaric oxygen on macrophage polarization after rat spinal cord injury. *Brain Research*, *1606*(295), 68–76. https://doi.org/10.1016/j.brainres.2015.01.029

Gensel, J. C., Kopper, T. J., Zhang, B., Orr, M. B., & Bailey, W. M. (2017). Predictive screening of M1 and M2 macrophages reveals the immunomodulatory effectiveness of post spinal cord injury azithromycin treatment. *Scientific Reports*, *7*(December 2016), 1–10. https://doi.org/10.1038/srep40144

Gordon, S. (2003). Alternative activation of macrophages. *Nature Reviews Immunology*, *3*(1), 23–35. https://doi.org/10.1038/nri978

Goshi, N., Vomero, M., Dryg, I., Seidman, S., & Kassegne, S. K. (2016). Modeling and characterization of tissue/electrode interface in capacitive µECoG glassy carbon electrodes. In *ECS Transactions* (Vol. 72). https://doi.org/10.1149/07201.0083ecst

Grainger, D. W. (2013). All charged up about implanted biomaterials. *Nature Biotechnology*, *31*(6), 507–509. https://doi.org/10.1038/nbt.2600

Gratchev, A., Kzhyshkowska, J., Köthe, K., Muller-Molinet, I., Kannookadan, S., Utikal, J., & Goerdt, S. (2006). Mphi1 and Mphi2 can be re-polarized by Th2 or Th1 cytokines, respectively, and respond to exogenous danger signals. *Immunobiology*, *211*(6–8), 473–486. https://doi.org/10.1016/j.imbio.2006.05.017

Harris, J. P., Hess, A. E., Rowan, S. J., Weder, C., Zorman, C. A., Tyler, D. J., & Capadona, J. R. (2011). In vivo deployment of mechanically adaptive nanocomposites for intracortical microelectrodes. *Journal of Neural Engineering*, *8*(4), 046010. https://doi.org/10.1088/1741-2560/8/4/046010

Hochberg, L. R., Bacher, D., Jarosiewicz, B., Masse, N. Y., Simeral, J. D., Vogel, J., …

Donoghue, J. P. (2012). Reach and grasp by people with tetraplegia using a neurally controlled robotic arm. *Nature*, *485*(7398), 372–375. https://doi.org/10.1038/nature11076

Hume, D. A., Ross, I. L., Himes, S. R., Sasmono, R. T., Wells, C. A., & Ravasi, T. (2002). The mononuclear phagocyte system revisited. *Journal of Leukocyte Biology*, *72*(4), 621–627. Retrieved from http://www.ncbi.nlm.nih.gov/pubmed/12377929

Isenhath, S. N., Fukano, Y., Usui, M. L., Underwood, R. A., Irvin, C. A., Marshall, A. J., … Olerud, J. E. (2007). A mouse model to evaluate the interface between skin and a percutaneous device. *Journal of Biomedical Materials Research. Part A*, *83*(4), 915–922. https://doi.org/10.1002/jbm.a.31391

Jiang, Mei H., Chung, E., Chi, G. F., Ahn, W., Lim, J. E., Hong, H. S., … Son, Y. (2012). Substance P induces M2-type macrophages after spinal cord injury. *NeuroReport*, *23*(13), 786–792. https://doi.org/10.1097/WNR.0b013e3283572206

Jiang, Mei Hua, Lim, J. E., Chi, G. F., Ahn, W., Zhang, M., Chung, E., & Son, Y. (2013). Substance P reduces apoptotic cell death possibly by modulating the immune response at the early stage after spinal cord injury. *Neuroreport*, *24*(15), 846–851. https://doi.org/10.1097/WNR.0b013e3283650e3d

Kassegne, S., Vomero, M., Gavuglio, R., Hirabayashi, M., Özyilmaz, E., Nguyen, S., … Khosla, A. (2015). Electrical impedance, electrochemistry, mechanical stiffness, and hardness tunability in glassy carbon MEMS µECoG electrodes. *Microelectronic Engineering*, *133*, 36–44. https://doi.org/10.1016/J.MEE.2014.11.013

Khaing, Z. Z., Cates, L. N., Fischedick, A. E., McClintic, A. M., Mourad, P. D., & Hofstetter, C. P. (2017). Temporal and Spatial Evolution of Raised Intraspinal Pressure after Traumatic Spinal Cord Injury. *J Neurotrauma*, *34*(3), 645–651. https://doi.org/10.1089/neu.2016.4490

Kim, Y.-H., Ha, K.-Y., & Kim, S.-I. (2017). Spinal Cord Injury and Related Clinical Trials. *Clinics in Orthopedic Surgery*, *9*(1), 1. https://doi.org/10.4055/cios.2017.9.1.1

Knowles, N. G., Miyashita, Y., Usui, M. L., Marshall, A. J., Pirrone, A., Hauch, K. D., … Olerud, J. E. (2005). A model for studying epithelial attachment and morphology at the interface between skin and percutaneous devices. *Journal of Biomedical Materials Research. Part A*, *74*(3), 482–488. https://doi.org/10.1002/jbm.a.30384

Lacour, S. P., Courtine, G., & Guck, J. (2016). Materials and technologies for soft implantable neuroprostheses. *Nature Reviews Materials*, *1*(10), 16063. https://doi.org/10.1038/natrevmats.2016.63

Luisi, J., Narayanaswamy, A., Galbreath, Z., & Roysam, B. (2011). The FARSIGHT Trace Editor: An Open Source Tool for 3-D Inspection and Efficient Pattern Analysis Aided Editing of Automated Neuronal Reconstructions. *Neuroinformatics*, *9*(2–3), 305–315. https://doi.org/10.1007/s12021-011-9115-0

Marshall, A., Irvin, C., Barker, T., Sage, E., Hauch, K., & Ratner, B. (2004). Biomaterials with tightly controlled pore size that promote vascular ingrowth. *ACS Polymer Preprints*, (45), 100–101.

Marshall, L. F., Smith, R. W., & Shapiro, H. M. (1979). The outcome with aggressive treatment in severe head injuries. *Journal of Neurosurgery*, *50*(1), 20–25. https://doi.org/10.3171/jns.1979.50.1.0020

Miller, J. D., Butterworth, J. F., Gudeman, S. K., Faulkner, J. E., Choi, S. C., Selhorst, J. B., … Becker, D. P. (1981). Further experience in the management of severe head injury. *Journal of Neurosurgery*, *54*(3), 289–299. https://doi.org/10.3171/jns.1981.54.3.0289

Mosser, D. M. (2003). The many faces of macrophage activation. *Journal of Leukocyte Biology*, *73*(2), 209–212. https://doi.org/10.1189/jlb.0602325

Mosser, D. M., & Edwards, J. P. (2008). Exploring the full spectrum of macrophage activation. *Nature Reviews. Immunology*, *8*(12), 958–969. https://doi.org/10.1038/nri2448

Mozaffarian, D., Benjamin, E. J., Go, A. S., Arnett, D. K., Blaha, M. J., Cushman, M., … American Heart Association Statistics Committee and Stroke Statistics Subcommittee.

(2015). Heart disease and stroke statistics--2015 update: a report from the American Heart Association. *Circulation*, *131*(4), e29-322. https://doi.org/10.1161/CIR.0000000000000152

Munder, M., Eichmann, K., & Modolell, M. (1998). Alternative metabolic states in murine macrophages reflected by the nitric oxide synthase/arginase balance: competitive regulation by CD4+ T cells correlates with Th1/Th2 phenotype. *Journal of Immunology (Baltimore, Md. : 1950)*, *160*(11), 5347–5354. Retrieved from http://www.ncbi.nlm.nih.gov/pubmed/9605134

Murray, P. J. (2006). Understanding and exploiting the endogenous interleukin-10/STAT3-mediated anti-inflammatory response. *Current Opinion in Pharmacology*, *6*(4), 379–386. https://doi.org/10.1016/j.coph.2006.01.010

Mytar, B., Siedlar, M., Woloszyn, M., Ruggiero, I., Pryjma, J., & Zembala, M. (1999). Induction of reactive oxygen intermediates in human monocytes by tumour cells and their role in spontaneous monocyte cytotoxicity. *British Journal of Cancer*, *79*(5–6), 737–743. https://doi.org/10.1038/sj.bjc.6690118

Nakajima, H., Uchida, K., Guerrero, A. R., Watanabe, S., Sugita, D., Takeura, N., … Baba, H. (2012). Transplantation of Mesenchymal Stem Cells Promotes an Alternative Pathway of Macrophage Activation and Functional Recovery after Spinal Cord Injury. *Journal of Neurotrauma*, *29*(8), 1614–1625. https://doi.org/10.1089/neu.2011.2109

National Spinal Cord Injury Statistical Center. (2013). Spinal Cord Injury Facts and Figures at a Glance. *The Journal of Spinal Cord Medicine*, *36*(1), 1–2. https://doi.org/10.1179/1079026813Z.000000000136

Nguyen, J. K., Park, D. J., Skousen, J. L., Hess-Dunning, A. E., Tyler, D. J., Rowan, S. J., … Capadona, J. R. (2014). Mechanically-compliant intracortical implants reduce the neuroinflammatory response. *Journal of Neural Engineering*, *11*(5). https://doi.org/10.1088/1741-2560/11/5/056014

O'Shaughnessy, W. Shannan, Gao, M., & Gleason, K. K. (2006). Initiated chemical vapor deposition of trivinyltrimethylcyclotrisiloxane for biomaterial coatings. *Langmuir*, *22*(16), 7021–7026. https://doi.org/10.1021/la0607858

O'Shaughnessy, W S, Murthy, S. K., Edell, D. J., & Gleason, K. K. (2007). Stable biopassive insulation synthesized by initiated chemical vapor deposition of poly(1,3,5-trivinyltrimethylcyclotrisiloxane). *Biomacromolecules*, *8*(8), 2564–2570. https://doi.org/10.1021/bm070242s

Phang, I., Werndle, M. C., Saadoun, S., Varsos, G., Czosnyka, M., Zoumprouli, A., & Papadopoulos, M. C. (2015). Expansion Duroplasty Improves Intraspinal Pressure, Spinal Cord Perfusion Pressure, and Vascular Pressure Reactivity Index in Patients with Traumatic Spinal Cord Injury: Injured Spinal Cord Pressure Evaluation Study. *Journal of Neurotrauma*, *32*(12), 865–874. https://doi.org/10.1089/neu.2014.3668

Prasad, A., Xue, Q. S., Sankar, V., Nishida, T., Shaw, G., Streit, W., & Sanchez, J. C. (2012). Comprehensive characterization of tungsten microwires in chronic neurocortical implants. *Proceedings of the Annual International Conference of the IEEE Engineering in Medicine and Biology Society, EMBS*, *056015*, 755–758. https://doi.org/10.1109/EMBC.2012.6346041

Soekadar, S. R., Birbaumer, N., Slutzky, M. W., & Cohen, L. G. (2014). Brain – machine interfaces in neurorehabilitation of stroke. *Neurobiology of Disease*, *83*, 172–179. https://doi.org/10.1016/j.nbd.2014.11.025

Stein, M., Keshav, S., Harris, N., & Gordon, S. (1992). Interleukin 4 potently enhances murine macrophage mannose receptor activity: a marker of alternative immunologic macrophage activation. *The Journal of Experimental Medicine*, *176*(1), 287–292. https://doi.org/10.1084/jem.176.1.287

Stice, P., Gilletti, A., Panitch, A., & Muthuswamy, J. (2007). Thin microelectrodes reduce GFAP expression in the implant site in rodent somatosensory cortex. *Journal of Neural*

Engineering, *4*(2), 42–53. https://doi.org/10.1088/1741-2560/4/2/005
Sussman, E. M., Halpin, M. C., Muster, J., Moon, R. T., & Ratner, B. D. (2014). Porous implants modulate healing and induce shifts in local macrophage polarization in the foreign body reaction. *Annals of Biomedical Engineering*, *42*(7), 1508–1516. https://doi.org/10.1007/s10439-013-0933-0
Thomson, K. S., Korte, F. S., Giachelli, C. M., Ratner, B. D., Regnier, M., & Scatena, M. (2013). Prevascularized microtemplated fibrin scaffolds for cardiac tissue engineering applications. *Tissue Engineering. Part A*, *19*(7–8), 967–977. https://doi.org/10.1089/ten.tea.2012.0286
Turner, J. N. (1999). , “Cerebral astrocyte response to micromachined silicon implants,.” *Experimental Neurology*, *vol*, 156pp33-49.
Underwood, R. A., Usui, M. L., Zhao, G., Hauch, K. D., Takeno, M. M., Ratner, B. D., … Fleckman, P. (2011). Quantifying the effect of pore size and surface treatment on epidermal incorporation into percutaneously implanted sphere-templated porous biomaterials in mice. *Journal of Biomedical Materials Research - Part A*, *98 A*(4), 499–508. https://doi.org/10.1002/jbm.a.33125
Verreck, F. A. W., de Boer, T., Langenberg, D. M. L., Hoeve, M. A., Kramer, M., Vaisberg, E., … Ottenhoff, T. H. M. (2004). Human IL-23-producing type 1 macrophages promote but IL-10-producing type 2 macrophages subvert immunity to (myco)bacteria. *Proceedings of the National Academy of Sciences of the United States of America*, *101*(13), 4560–4565. https://doi.org/10.1073/pnas.0400983101
Vomero, M., Dryg, I., Maxfield, T., Shain, W., Perlmutter, S., & Kassegne, S. (2016). In-vivo characterization of glassy carbon μ-electrodes and histological analysis of brain tissue after chronic implants. In *ECS Transactions* (Vol. 72). https://doi.org/10.1149/07201.0091ecst
Ward, M. P., Rajdev, P., Ellison, C., & Irazoqui, P. P. (2009). Toward a comparison of microelectrodes for acute and chronic recordings. *Brain Research*, *1282*, 183–200. https://doi.org/10.1016/j.brainres.2009.05.052
Werndle, M. C., Saadoun, S., Phang, I., Czosnyka, M., Varsos, G. V., Czosnyka, Z. H., … Papadopoulos, M. C. (2014). Monitoring of Spinal Cord Perfusion Pressure in Acute Spinal Cord Injury. *Critical Care Medicine*, *42*(3), 646–655. https://doi.org/10.1097/CCM.0000000000000028
Williams, J. C., Hippensteel, J. A., Dilgen, J., Shain, W., & Kipke, D. R. (2007). Complex impedance spectroscopy for monitoring tissue responses to inserted neural implants. *Journal of Neural Engineering*, *4*(4), 410–423. https://doi.org/10.1088/1741-2560/4/4/007
Woolley, A. J., Desai, H. A., Steckbeck, M. A., Patel, N. K., & Otto, K. J. (2011). In situ characterization of the brain-microdevice interface using Device Capture Histology. *Journal of Neuroscience Methods*, *201*(1), 67–77. https://doi.org/10.1016/j.jneumeth.2011.07.012
Xie, Y., Bonin, T., Löffler, S., Hüttmann, G., Tronnier, V., & Hofmann, U. G. (2013). Coronal in vivo forward-imaging of rat brain morphology with an ultra-small optical coherence tomography fiber probe. *Physics in Medicine and Biology*, *58*(3), 555–568. https://doi.org/10.1088/0031-9155/58/3/555
Ziegler-Graham, K., MacKenzie, E. J., Ephraim, P. L., Travison, T. G., & Brookmeyer, R. (2008). Estimating the Prevalence of Limb Loss in the United States: 2005 to 2050. *Archives of Physical Medicine and Rehabilitation*, *89*(3), 422–429. https://doi.org/10.1016/j.apmr.2007.11.005

Appendix

Tissue Histology Protocol

Unless otherwise stated, these methods were used for tissue histology. Animals were anesthetized using isoflurane (5% in oxygen) or IP injection (5-6 µL/g) of a ketamine (20 mg/mL) / xylazine (3 mg/mL) mixture, and tested for a surgical level of anesthesia using the foot pinch test. Then, animals were cardiac perfused with PBS and 4% paraformaldehyde. Heads were removed and post-fixed overnight at 4 degrees C. Because explanting an implanted device can disrupt cellular responses on and near the device's surface, attempts are sometimes made to maintain the implanted devices *in situ* for tissue histology, as previously described (Woolley, Desai, Steckbeck, Patel, & Otto, 2011). Brains were removed from the skull and stored in HBHS with sodium azide until sectioning. A series of 100-150 µm thick brain slices were made, when possible, with an alignment designed to capture the implanted devices within a single tissue slice (coronal sections). If in-situ device capture was not performed, often horizontal slices were taken through a cross-section of the implant. Tissue slices were stored in HBHS with sodium azide until immunohistochemistry. Slices were treated with primary antibodies GFAP, Iba1, NeuroTrace, and Hoechst, labeling astrocytes, microglia, neurons, and all cell nuclei, respectively. Confocal microscopy was performed to image the histology and fluorescence profiles were quantified. Within all studies, the same microscopy settings were used so quantifications could be compared.

Shain Lab Immunohistochemistry Protocol for Floating Sections

Day 1:

1. Wash 3x in HBHS with sodium azide, rapid rinses
    a. HEPES replaces bicarbonate of Hanks, HEPES is very physiological at wide temperature range (maintains osmolarity to +/- 0.1 mosm). Osmolarity greatly influences cells because of pressure/shrinking.
2. Incubate in 5 mg/ml $NaBH_4$ in HBHS for 30min
    a. Exposes antigen post-crosslinking
3. Wash 3x in HBHS with sodium azide, rapid rinses
4. Incubate in 0.2% Triton-X-100 in HBHS with azide for 30min
    a. Detergent, lyses membrane
    b. 200 µL 1% Triton + 0.8 mL HBHS
5. Wash 3x in HBHS with sodium azide, rapid rinses
6. Wash 3x in HBHS with sodium azide, rapid rinses
7. Block in 5% Normal Serum (from 2^{o} Antibody Host) or Image-iT FX for 30min at room temperature
    a. 4-5 drops per 500 µL (1 well of 24-well plate)
    b. Blocks background staining from non-specific and dye interactions
8. Wash 3x in HBHS with sodium azide, rapid rinses
9. Incubate overnight in primary antibodies in 0.2 Triton-X-100 in HBHS with sodium azide at room temperature

Day 2:

1. Wash 4x for 30min each in HBHS with sodium azide
2. Incubate overnight in secondary antibodies in 0.2% Triton-X-100 in HBHS with sodium azide at room temperature. Cover with foil (protect from light)

Day 3:

1. Wash 4x for 30min in HBHS with sodium azide with 0.5% Tween 20
    a. 5 µL Tween 20 in 1000 µL of HBHS
    b. Reduces non-specific and protein to protein interactions
2. Mount onto slides with Fluoromount-G or Prolong Gold

Shain Lab 4% Paraformaldehyde Recipe

Sodium Phosphate Buffers:

0.4M Na_2HPO_4 (FW 141.96) dibasic: 56.78 g/L

0.4M NaH_2PO_4 (F@ 137.99) monobasic: 56 g/L (28 g/500mL)

4% Paraformaldehyde Protocol:

1. Mix the following under a fume hood:
    a. 40 grams Paraformaldehyde (PFA)
    b. 600 mL dH_2O
2. Stir and heat to 60^oC
    a. Allow most of the PFA to dissolve before moving to the next step
3. Add 5+ pellets of NaOH: solution will begin to clear
4. Add 202.5 mL of 0.4M dibasic Sodium Phosphate buffer
5. Add 47.5 mL of 0.4M monobasic Sodium Phosphate buffer
6. Allow PFA to continue to dissolve
7. Vacuum filter the PFA solution
8. Fill up to 1000mL final volume with dH_2O
9. Adjust pH to 7.4

Shain Lab HBHS (HEPES Buffered Hanks Saline) Recipe

10X Stock Solutions:

		grams/100mL	grams/500mL	grams/1L
Monovalent Salts 10X Stock	NaCl	7.5	37.7	75.4
	KCl	0.3	1.5	3.0
	Na_2HPO_4	0.1	0.7	1.4
	KH_2PO_4	0.1	0.3	0.7
Divalent Salts 10X Stock	$CaCl_2$	0.1	0.6	1.2
	$MgCl_2$	0.0	0.1	0.3
	$MgSO_4$ x 7H	0.0	0.2	0.5

Working Solution:

	1 Liter	2 Liters
Monovalent Salts 10X Stock	100 mL	200 mL
Divalent Salts 10X Stock	100 mL	200 mL
HEPES	2.4 grams	4.8 grams
Glucose (Dextrose)	2.0 grams	4.0 grams
Sodium Azide	90 mg	180 mg

- Bring solution to final liter volume with dH_2O
- pH final solution to 7.4 with 1.0 N NaOH

Directions:

1. Add half of dH_2O to beaker before adding stock solutions (otherwise divalent salts will precipitate)
2. Add stock solutions
3. Add HEPES and Glucose (Dextrose)
4. Add Sodium Azide
5. Bring volume to 100% with dH_2O
6. pH to 7.4

List of publications:

C. Boehler, C. Kleber, N. Martini, Y. Xie, **I. Dryg**, T. Stieglitz, U. Hofmann, M. Asplund. "Actively controlled release of Dexamethasone from neural microelectrodes in a chronic in-vivo study." Biomaterials (2017). Print.

Noah Goshi, M. Vomero, **Ian Dryg**, S. Seidman, Sam Kassegne. "Modeling and Characterizing of Tissue/Electrode Interface in Capacitive ECoG Glassy Carbon Electrodes." ECS Transactions. (2016)

Maria Vomero, **Ian Dryg**, Tyler Maxfield, William Shain, Steve Perlmutter, Sam Kassegne. "In-Vivo characterization of Glassy Carbon-Electrodes and Histological Analysis of Brain Tissue after Chronic Implants." ECT Transactions. (2016)

Dryg, Ian, Matthew Ward, Kurt Qing, Henry Mei, Jeremy Schaffer, and Pedro Irazoqui. "Magnetically Inserted Neural Electrodes: Tissue Response and Functional Lifetime." Transactions on Neural Systems and Rehabilitation Engineering (2015).Print.

IAN D. DRYG

Seattle, WA, 98103 iddryg@gmail.com
(563) 940-3841 www.linkedin.com/in/idryg United States Citizen

Profile:

Six years of collaborative PhD experience assessing markers of inflammation in response to custom-engineered polymeric biomaterials and brain-recording devices. **Relevant skills include:** immunohistochemistry, fluorescence microscopy, flow cytometry, MATLAB, image analysis, electrophysiology, signal processing, and animal care and surgery.

Education:

2013 – 2019 **University of Washington** – *Seattle, WA*
Ph.D. – Bioengineering, Expected Summer 2019
Concentration – Neural Engineering, Neural Interfaces, Foreign Body Reaction, Inflammation, Biomaterials
Thesis – Modulating Neuroinflammation with Porous Templated Scaffolds
GPA – 3.7 / 4.0

2012 – 2013 **Purdue University** – *West Lafayette, IN*
M.S. – Biomedical Engineering, May 2013
Concentration – Neural Engineering, Neural Interfaces, Reactive Tissue Response
Thesis – Magnetically Inserted Flexible Electrodes: Tissue Response and Functional Lifetime
GPA – 3.75 / 4.0

2008 – 2012 **Purdue University** – *West Lafayette, IN*
B.S. – Biomedical Engineering Major, Mathematics Minor, May 2012
GPA – 3.63 / 4.0

Research Experience:

2015 – 2019 **University of Washington** – *Seattle, WA, USA*
Advisors: Buddy Ratner Ph.D. & James Bryers Ph.D.
Thesis: *Modulating Neuroinflammation with Porous Templated Scaffolds*
- Assessed neuro-inflammatory response to custom-engineered polymer scaffolds for neural engineering applications.

2013 – 2015 **University of Washington / Seattle Children's Research Institute** – *Seattle, WA, USA*
Advisor: Bill Shain Ph.D.
- Collaborated with groups from UW, SDSU, and MIT, and Blackrock Microsystems. Developed implantable neural devices which avoid, control, or investigate reactive brain tissue responses.

2014 Summer **University of Freiburg** – *Freiburg, Germany*
Advisor: Ulrich Hofmann Ph.D.
Thesis: *Optical Coherence Tomography for Online Monitoring of Brain Implants*
- Collaborative international exchange using Optical Coherence Tomography (OCT) for real-time monitoring of tissue responses surrounding implantable neural devices *in vivo*, compared with traditional immunohistochemistry.

2010 – 2013 **Purdue University** – *West Lafayette, IN, USA*
Advisor**:** Pedro Irazoqui Ph.D.
Thesis: *Magnetically Inserted Neural Electrodes: Tissue Response and Functional Lifetime*

- Can smaller implant size, faster insertion speed, and inert electrode material reduce the tissue response in the brain; and increase functional lifetimes for neural prostheses?

2011 – 2012 **Purdue University and Northwestern University**– *West Lafayette, IN, USA and Chicago, IL, USA*
Advisors**:** Pedro Irazoqui Ph.D. (Purdue) & Todd Kuiken M.D. (Northwestern)
Thesis: *The Osseo-Magnetic Link – A Prosthetic for Transradial Amputees*

- Developed a prosthetic arm to allow transradial amputees more intuitive and accurate control of wrist rotation

2010 **Purdue University** – *West Lafayette, IN, USA*
Advisor**:** Alyssa Panitch Ph.D.
Thesis: *Local treatment of osteoarthritis using cytokines harvested from the patient*

Publications:

2017 C. Boehler, C. Kleber, N. Martini, Y. Xie, **I. Dryg**, T. Stieglitz, U. Hofmann, M. Asplund. "Actively controlled release of Dexamethasone from neural microelectrodes in a chronic in-vivo study." Biomaterials (2017). Print.

2016 Noah Goshi, M. Vomero, **Ian Dryg**, S. Seidman, Sam Kassegne. "Modeling and Characterizing of Tissue/Electrode Interface in Capacitive ECoG Glassy Carbon Electrodes." ECS Transactions. (2016)

2016 Maria Vomero, **Ian Dryg**, Tyler Maxfield, William Shain, Steve Perlmutter, Sam Kassegne. "In-Vivo characterization of Glassy Carbon-Electrodes and Histological Analysis of Brain Tissue after Chronic Implants." ECT Transactions. (2016)

2015 **Dryg, Ian**, Matthew Ward, Kurt Qing, Henry Mei, Jeremy Schaffer, and Pedro Irazoqui. "Magnetically Inserted Neural Electrodes: Tissue Response and Functional Lifetime." Transactions on Neural Systems and Rehabilitation Engineering (2015).Print.

Grants/Awards:

2016 **Institute for Translational Health Sciences Collaboration Grant**
Project: Modulating Neuroinflammation after Spinal Cord Injury using Porous Templated Scaffolds

2014 **NSF Center for Sensorimotor Neural Engineering Student Seed Grant** – *January 2014*
Project: Correlating Surface and Implantable Electrode recording Performance using focal Drug Delivery and light evoked responses
Each student is the PI of his/her grant. Provides funding for a research project. Awarded to a handful of graduate students within the CSNE.

2014 **NSF Center for Sensorimotor Neural Engineering Research Grant**
Project: Correlating Surface and Implantable Electrode recording Performance using focal Drug Delivery and light evoked responses
Awarded to a handful of graduate students within the CSNE. Covers tuition, stipend, etc.

Skills:

Technical: Flow Cytometry, Immunohistochemistry, Tissue Histology, Polymer Chemistry, Bioconjugation (EDC-NHS),
Cell Culture, ELISA, Electrical Impedance Spectroscopy, Electrophysiology, Spike Sorting, Wire Bonding, Circuit Board Milling, Soldering

Imaging: Confocal Microscopy, Optical Coherence Tomography, Scanning Electron Microscopy

Computer: MATLAB, Python, Microsoft Excel, Arduino, FIJI (ImageJ)

Animal: Rat & Mouse: Handling, Anesthesia, Injections, Surgery, Euthanasia, Cardiovascular Perfusions

Presentations:

2019 **Society for Biomaterials Conference** – *Seattle, WA*
Poster Title: Porous Hydrogels for Neural Implants: Effect of Pore Size on Glial Encapsulation

2018 **NeuroFutures Conference** – *Seattle, WA*
Poster Title: Directing Brain Tissue Integration for Long-Term Electrophysiology with Conductive Microporous Hydrogel Electrodes

2018 **Gordon Conference for Neuroelectronic Interfaces** – *Galveston, TX*
Poster Title: Directing Brain Tissue Integration for Long-Term Electrophysiology with Conductive Microporous Hydrogel Electrodes

2017 **SPIE Photonics West** – *San Francisco, CA*
Poster Title: Online Monitoring of Tissue Responses to Plasma Coated Rigid Neural Implants using Fiber- based Optical Coherence Tomography

2015 **Biomaterials Seminar: University of Washington** – *Seattle, WA*
Presentation Title: Tissue Responses to Neural Implants

2015 **NSF Site Visit**: **UW Center for Sensorimotor Neural Engineering** – *Seattle, WA*
Poster Title: First-ever optical monitoring of brain implants; comparison with traditional tissue histology

2014 **First Annual NeuroFutures Conference** – *Seattle, WA*
Poster Title: Correlating tissue responses with recording performance of implanted and brain-surface electrodes

2014 **NSF Site Visit**: **UW Center for Sensorimotor Neural Engineering** – *Seattle, WA*
Poster Title: Correlating tissue responses with recording performance of implanted and brain-surface electrodes

2013 **Cyberonics, Inc.** – *Houston, TX*
Event: Educational/Informational Class on Neuroscience for Employees of Cyberonics, Inc.
Presentation Title: Neural Interfaces

2012 **American Epilepsy Society Annual Meeting** – *San Diego, CA*
Poster Title: Magnetically Inserted Flexible Microelectrodes Reduce the Reactive Tissue Response

2012 **Undergraduate Research Poster Symposium** – *West Lafayette, IN*
Poster Title: Active Sensor for Proprioception in Trans-radial Amputees

2011 **TechCon** – *Austin, TX*
Poster Title: Active Sensor for Proprioception in Trans-radial Amputees

2011 **Undergraduate Research Poster Symposium** – *West Lafayette, IN*
Poster Title: Multi-modal Flexible Neural Prosthesis Combining Optical, Chemical, and Electrical Stimulation

Honors:

2015 **2nd Place - DARPA C4C Combinator Innovation Competition**
Project: Combine 2 or more DARPA-funded research projects to develop new product/business ideas.

2012 **Undergraduate Research Poster Symposium**
Award: Purdue Engineering Student Council Award
Poster Title: Active Sensor for Proprioception in Trans-radial Amputees

2011 **1st Place - Undergraduate Research Poster Symposium**
Award: First Place in Innovative Technology/Entrepreneurship & Design
Poster Title: Multi-modal Flexible Neural Prosthesis Combining Optical, Chemical, and Electrical Stimulation

2008 – 2012 **Purdue University Presidential Scholarship** – $10,000 per year
High academic achievement; Demonstrated experience in leadership, service, and/or school or community activity.

2000 – 2008 **Boy Scouts of America** – *Troop 89, Bettendorf, IA*
Eagle Scout; Patrol Leader; Den Chief

Interests/Activities:

General: Outdoors sports | Photography | Music (Percussionist) | Fitness

2014 – Present **University of Washington Climbing Club** – Rock Climbing, Mountaineering, Ski touring

2014 – 2018 **University of Washington Kayak Club** – Whitewater and Sea Kayaking

2008 – 2013 **Purdue Outing Club** – Outdoor Adventure Sports
Positions: President, Whitewater Kayaking Consultant
Activities: Whitewater Kayaking, Rock Climbing, Caving, Mountain Biking

2009 – 2012 **Purdue Tomahawk** – Leadership and Community Service
Positions: Pledge Mentor, Social Coordinator

2009 – 2013 **Purdue Biomedical Engineering Society**

2009 – 2011 **Purdue Rescue Squad**
Provide medical assistance at Purdue Football Games